Università degli Studi di Genova

Doctorate in

Sciences and Technologies of

Chemistry and Materials

Curriculum: Chemical Sciences and Technologies

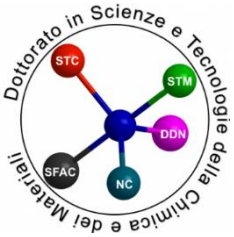

Flory-Huggins Photonic Sensors

PAOLA LOVA

Supervisor: Prof. Davide Comoretto

Abstract

This Thesis focuses on the design of a simple optical method for the determination of molecular diffusion coefficients and for the quali-quantitative assessment of the diffusing species in polymer photonic sensors and in commercial polymer thin films used in packaging.

This project arose to overcome the lack of methodologies related to the detection of hazardous vapor molecules both in air and in goods packaging. To tackle this task, this Thesis proposes simple optical spectroscopy coupled to photonic crystal sensors (called Flory-Huggins Photonic Sensors, FHPSs) and commercial polymer thin films to retrieve quali-quantitative information of polluted air and molecular diffusion coefficient in the polymers themselves. This is achieved studying the kinetics of optical variations in the diffraction and/or interference pattern of the sensors, which are opportunely designed to interact with the analyte species.

In the first Chapters, after discussing the problematics related to the monitoring of vapor analytes and to the determination of diffusion coefficients, this Thesis explains the working principle of the FHPSs, and the optical set-up designed to the purpose. Then, commodity polymers FHPSs are used as proof of principle to create a receipt for the design of sensors suitable for any class of chemical compounds. This system also shows colorimetric response with sensitivity and lower detection limit approaching the part per million and label free selectivity to the tested analytes. Moreover, the study of the kinetics of the spectral response allow to evaluate the diffusion coefficients of the analytes within the photonic structure. The method is then tested for the detection of various pollutants. The possibility to use unstructured commercial films to the same purposes in also discussed and demonstrated.

These results promise to simplify detection of volatile pollutants in atmosphere and a new simple tool to asses diffusion of hazardous molecules in packaging systems. The possibility to assess the colorimetric response of the FHPSs even by the naked eye, together with the capability to monitor diffusive processes in polymer packaging film directly on the shelf, promises also safety devices and continuous assessment of goods.

Acknowledgements

I want to express my deepest gratitude to my supervisor, Prof. Davide Comoretto, for the priceless guidance and advice he has provided through this PhD.

I would also like to acknowledge the several collaborators I had during these years:

- Prof. Alberto Servida of the Department of Chemistry and Industrial Chemistry of the University of Genova for the multivariate analysis of photonic sensors.
- Prof. Francesco Buatier de Mongeot and Carlo Mennucci of the Department of Physics of the University of Genova for the help with experimetal procedures.
- Prof. Maddalena Patrini of the University of Pavia for her experimental support.
- Dr Dario Cavallo of the Department of Chemistry and Industrial Chemistry of the University of Genova for the help with experimental procedures related to this project.
- Prof. Giuseppe Portale and Marco Viviani from the University of Groningen for the precious help in project related to this Thesis.
- Prof. Cesare Soci and Dr Daniele Cortecchia from the Nanyang Technological University of Singapore for the help with hybrid perovskite materials.
- Dr Francesco di Stasio and Dr Roman Khrane from the Italian Institute of Technology of Genova for providing nanocrystals.
- Prof. Dr Frank Würthner and Dr Vincenzo Grande of the University of Wurzburg for providing new and interesting emitters.
- Dr Giuseppe Paternò from the Italian Institute of Technology of Milan for the help with experimental procedures.

Completing this work would not have been possible if not for the support of colleagues and students: Dr Giovanni Manfredi, Heba Megahd, Andrea Dodero, Stefano Alberti, Chiara Bastianini, Paolo Giusto, Selena Silvano, Alba Surace and Gabriele Pesce.

My gratitude goes also to the Administrative Staff of the Department of Chemistry and Industrial Chemistry of the University of Genova.

Table of Contents

List of Abbreviations

1POH	1-propanol, (propan-1-ol)
2POH	2- propanol, (propan-2-oll)
aPP	Amorphous polypropylene
ASE	Amplified stimulated emission
BEN	Benzene
BuOH	1-butanol, (butan-1-ol)
CA	Cellulose acetate
CTC	Carbon tetrachloride. (tetrachloromethane)
CW	Continuous wave
DBR	Distributed Bragg reflector
DFB	Distributed feedback
DiR	Dot in rod
DMF	Dimethyl formamide, (N, N – dimethylformamide)
DMSO	Dimethyl sulfoxide, (methylsolfinylmethane)
(EDBE) $PbCl_4$	2,2'-(ethylenedioxy)bis(ethylammonium) lead chloride
EtOH	Ethanol
FHPS	Flory-Huggins photonic sensor
FWHM	Full width half maximum
HY	Hyflon AD polymer
LED	Light emitting diode
LOD	Lower detection limit
MA PbI_3	Methylammonium lead iodide
MC	Microcavity
MeOH	Methanol
o-DCB	Ortho dichlorobenzene, (1, 2 – dichlorobenzene)
PAA	Polyacrylic acid
PBI	Perylene bisimide
PDOS	Photonic density of stated
PEH-PBI	phenoxy-functionalized PBI

PhC	Photonic crystal
PL	Photoluminescence
PMMA	Poly (methyl methacrylate)
PS	Polystyrene
PVC	Polyvinyl chloride
PVK	Poly (N-vinylcarbazole)
Q-factor	Quality factor
QY	Quantum yield
RPS	Rounds per second
TEM	Transmission electron microscopy
TMM	Transfer Matrix Method
TOL	Toluene
UV	Ultraviolet
VCSEL	Vertical cavity surface emitting laser
VIS	Visible
VOC	Volatile organic compound
ZnONP@PS	ZnO nanoparticles - polystyrene nanocomposite

Summary

Photonic Crystals

Following the seminal researches by John[1] and Yablonovitch,[2] photonic crystals (PhCs) stimulated wide fundamental interest, that nowadays results in many technological applications.[3] PhCs are arrays of media having different dielectric function arranged in sub-micrometric lattices which can extend with different dimensionality (Figure 1).[4-5] Such structures affect photons properties as the crystal potential in a semiconductor affects the properties of electrons. Therefore, one can extend to PhCs three basic concepts from semiconductors: the photonic band structure, which identifies spectral regions forbidden and allowed to photon propagation;[5] the photonic band gap (PBG), which is responsible for the PhC chromatic response;[6-9] and the density of photonic states (PDOS), [2-5] which helps explaining the effects on the photoluminescence (PL) of materials embedded in the PhC. Then, to understand the working principle of PhCs, we will use the analogy with semiconductors. In electronics, a crystal is a structure where atoms are arranged in an array of points generated by periodic translations, namely the Bravais Lattice. The interaction between the periodic potential and electrons defines frequency regions forbidden to the latter, called energy band gaps.[9] The optical analogous of a crystal is a PhC, where macroscopic media with different refractive index are ordered with a periodicity comparable to the wavelength of visible light.[10] Here, light diffraction and refraction at every interface generates PBGs, where photons cannot propagate and are diffracted backward (or reflected) providing the structures with their characteristic iridescent colors (Figure 1)[11,12] Intuitively, the higher is the dielectric contrast within the lattice, the stronger is the control over the light that one can achieve. For these reasons, PhC have been historically made by material with high refractive index (e.g. GaAs and GaN) and air. On the other hand, structuring such materials requires complicated, expensive and time demanding techniques such as e-beam and focus ion beam lithography and metal-organic vapor deposition.[13–15] These structures are still a hot topic in photonics for optical fibers, light emitting diodes (LEDs), sensors, photovoltaic devices, lasers, lightening and quantum computing.[10] However, new solution processable photoactive materials incompatible with the processing of bulky inorganic structures (e.g. organic semiconductors quantum dots, hybrid perovskites and self-assembling supramolecular systems) stimulated the development of PhCs grown with organic and colloidal materials by solution and melt processes.[11-13]

As a consequence, thanks to the ease of processing and the low cost, polymers become interesting building blocks for photonic structures.[16–19] Figure 1 reports some example of polymer structures with different dimensionality and compare them with well-known natural lattices.[8] Figure 1a shows the schematic and photographs of mono-dimensional planar lattices, also called distributed Bragg Reflectors (DBRs), where alternated polymer thin films deposited by simple spin coating[20] resemble the nacre. Similarly, Figure 1b shows a two dimensional lattice fabricated soft lithography[21], whose natural analogue is the sea-mouse (Figure 1b bottom). Water dispersion of microspheres can instead be used to fabricate three-dimensional structures, like those illustrated in Figure 1c.[22]

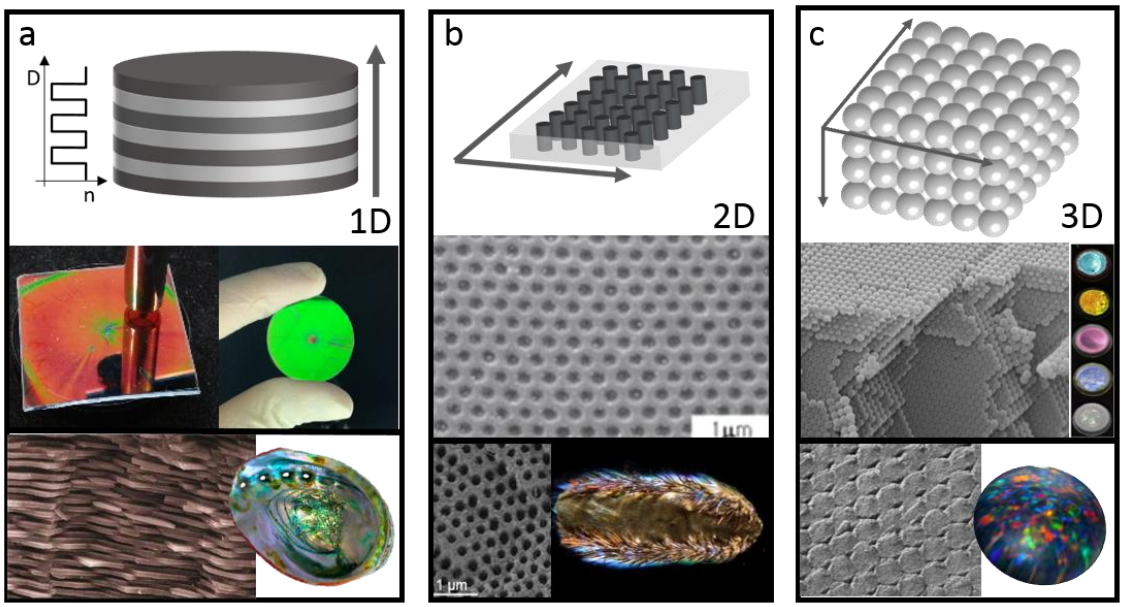

Figure 1: Scheme and photographs of synthetic and natural PhCs with different dimensionality: a) 1D: polymer multilayers and nacre[6] b) 2D: hole array fabricated by soft lithography and sea mouse spines[23] and c) 3D: microsphere lattice synthetic opals and a natural opal.[24]

Among PhCs, DBRs are currently the most interesting owing to their simple optical response providing a playground to understand deep physical concepts. DBRs are indeed made of alternated thin films of different dielectric materials. This simplicity makes them the only PhCs that can take advantage of large area growths.[14] Such fabrications are restricted to polymeric media, and are unconceivable for bulky inorganic DBRs. Large area fabrications might reduce processing costs and enhance customizability, also on industrial scale, thus adding unprecedented market opportunities. Figure 2 illustrates the evolution and fabrications of

solution and melt processed DBRs. The top of the Figure displays three well-known natural DBRs belonging to animal and plant reigns: the nacre in a seashell,[15] the Panamanian Tortoise beetle exoskeleton,[16] and the *Pollia Condensata* skin,[17] whose growth is driven by the thermodynamics of spinodal phase separation.[18] The interest in these natural structures led to their emulation until the development of solution-based fabrication methods for flexible synthetic DBRs made of polymers and inorganic nanoparticles. The base of Figure 2 shows some applications arose only in the last decades. From left to right: the use of DBRs in functional architecture, in enhancement of photon absorption for photovoltaic cells and modules, emission control, lasing, and sensing.[13, 19-21]

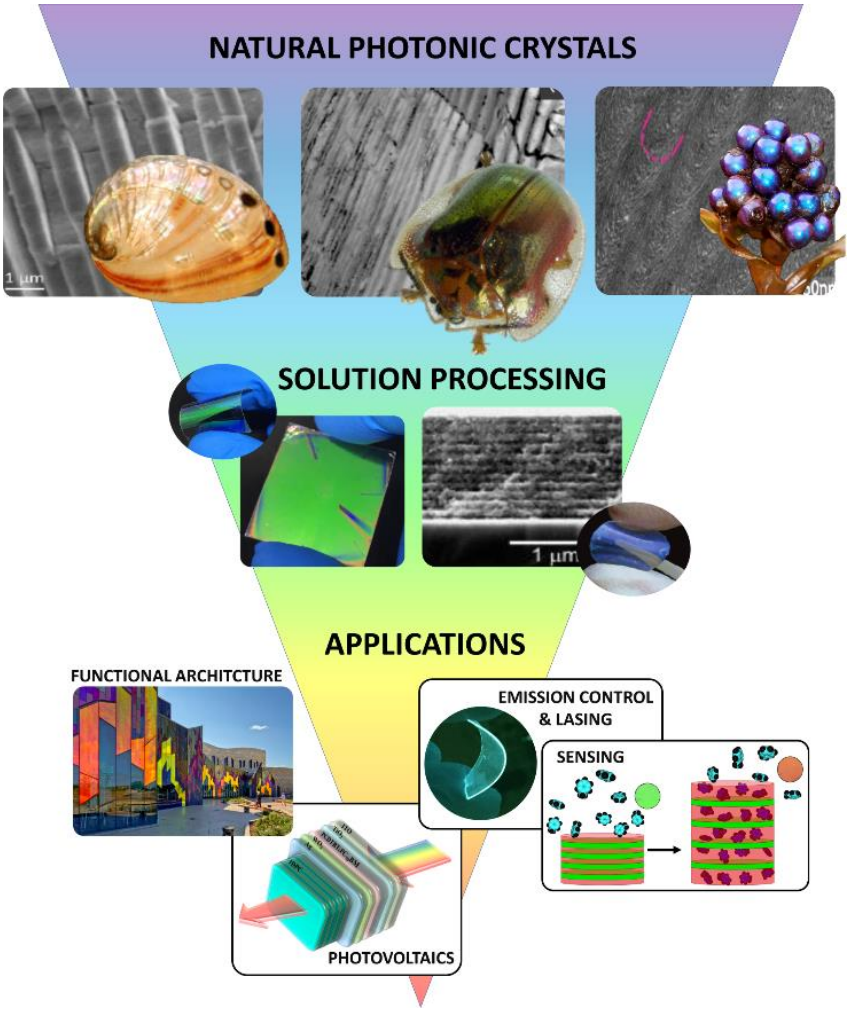

Figure 2: From top to bottom: electron microscopy and digital images of natural DBRs: nacre[15], Panamanian Tortoise[16], and *Pollia Condensata*;[17] photographs and schematic of DBRs and applications.[13, 19-21]

Background

Among those just mentioned, sensing is the most promising field of application of polymer DBRs. Indeed, several preliminary works demonstrated that their high sensitivity and broad-band selectivity to, among others, vapor and gas polluttants.[22-29] The optical response of these sensors relies on the permeation of vapor molecules within the DBR and the swelling of the polymers, which induces a color variation. The example of Figure 3 schematizes the typical response of a polymer DBR to a vapor analyte penetrating it starting from the top layer, which contacts the air environment and inducing the progressive swelling of the films. In turn, the swelling increases the light optical path and shifts the PBG to the longer wavelength side of the spectrum providing the colorimetric response.

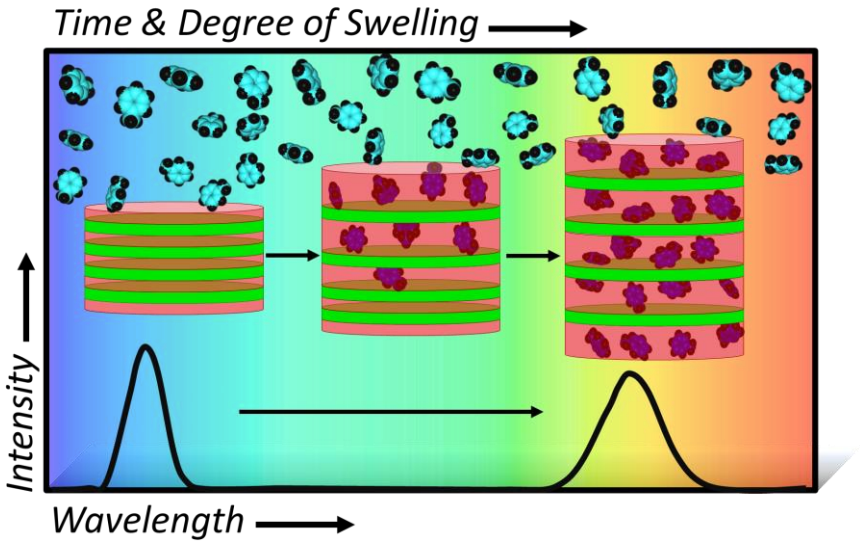

Figure 3: Schematic of the processes occurring into polymer DBR sensors during the exposure to vapor analytes.[23]

The presence of a characteristic behavior for different analytes suggested that studying the kinetics of this spectral response would allow distinguishing different analytes. This process was demonstrated for phase changing polymer building blocks (Figure 4).[22] In this case, registering the spectrum of the DBR sensor at a set time provides different signals, which depend on the different intercalation kinetics of the analytes within the DBR. On the other hand, the mechanism behind the selectivity and sensitivity to different analytes was not fully

understood, while the comprehension of these mechanism would allow to define a new strategy for the fabrication of sensors with borad lablel-free selectivity.

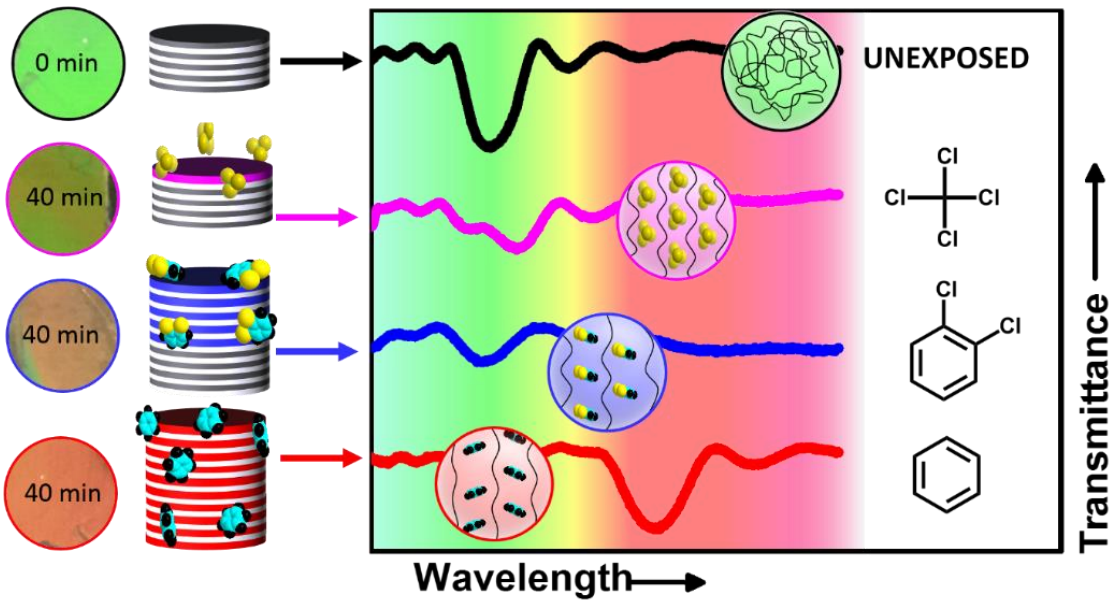

Figure 4: Scheme of phase changing DBR sensors (black line) to CCl_4 (magenta), 1,2-diclorobenzene (blue), and benzene (red).The photographs on the left shows the surface of the sensors before and after the exposure to the analytes..[22]

Motivations and Aims

This Thesis focuses on the design of a simple optical method for the determination of molecular diffusion coefficients and for the quali-quantitative assessment of the diffusing species in polymer DBRs and commercial polymer thin films used in packaging. This project arose to overcome the lack of methodologies related to the detection of hazardous molecular species in the vapor phase in air and in goods packaging. The current technology requires indeed complex and time demanding laboratory analyses. To tackle this task, this Thesis proposes to employ optical spectroscopy coupled to the polymer structures just mentioned to retrieve quali-quantitative information of polluted air and molecular diffusion coefficient in the polymers themselves. This is achieved studying the kinetics of the variations in the diffraction and/or interference pattern of the sensors, which are opportunely designed to interact with the analyte species. The goal is the design of sensors that can assess air quality and be potentially implemented into packaging systems to provide information about degradation markers and

intercalation of hazardous molecule into the packaging itself. This aspect can indeed allow monitoring of goods quality as well as degradation of packaging barrier properties.

Thesis Structure

Chapter 1 highlights the importance of simple detection systems for the qualitative and quantitative analysis of vapor analytes. The importance of atmosphere monitoring has been indeed widely recognized and recently the possibility to assess the quality of air in sealed containers revealed new perspectives in health preservations and device encapsulation. The Chapter reviews state of the art technologies for the qualitative and quantitative detection of volatile species focusing on their figures of merit and main limitations. Then, it introduces new colorimetric technologies aimed to simplify the analyses which disclose compatibility with packaging systems. Last, it proposes a new method that exploit polymer multilayers to achieve contemporary analysis of volatile species and determination of their diffusion coefficient within the polymer themselves by simple UV-Vis spectroscopy.

Chapter 2 describes the fabrication methodologies and characterization techniques developed for the sensing measurements and used for sensors characterization in the Thesis work.

Chapter 3 describes polymer DBRs label-free colorimetric sensors featuring specific interactions with pollutants for environmental monitoring and packaging technologies. This Chapter reports on commodity polymer multilayers as proof-of-principle systems to demonstrate that DBRs sensitivity and selectivity can be explained in term of Flory-Huggins interaction parameters between the sensor polymers and the analyte. In details, it reports on the response of multilayers made of cellulose acetate and polystyrene to five short chain alcohols for the determination of their diffusion coefficient in the polymer matrix monitoring of the UV-VIS optical response of the photonic sensors. In addition, this part focuses on sensors selectivity also in binary mixtures. Eventually, sensitivity, lower detection limit and reversibility of these systems are also investigated. This Chapter defines then a general method for the design of FHPSs able to detect and disentangle any class of vapor compounds and measure their diffusion coefficients.

In Chapter 4 the new method is tested for the assessment of aryl, halogenated and perfluorinated compounds FHPSs designed on the base of their Flory-Huggins interaction parameter with the analytes.

Chapter 5 demonstrates the use of UV-Vis optical spectroscopy to determine the diffusion coefficient of small molecules in unstructured commercial polymer film used in packaging. Using the same working principle demonstrated for DBR vapor sensors it is indeed possible to employ the interference pattern typical of thin polymer films for the assessment of diffusion coefficients and even to recognize the analyte diffusing into the polymer.

Chapter 6 discusses the results achieved during this Thesis project and propose a future research path to achieve use of the sensors in real environment.

Chapter 7 reports on other projects related to the one reported in this Thesis. Polymer multilayered structure where indeed also employed to achieve emission control and lasing. This project accompanied the main one of this Thesis to the goal to demonstrates that polymer photonic structures are feasible. The Chapter first introduces the concept of microcavities, and their effect on light matter interaction. It will then briefly discuss the result achieved both in light emission control and lasing demonstrating the capability to couple several emitters, including perovskites, organic molecules and inorganic nanocrystals into microcavity structures.

Last, Appendix A reports the theoretical background useful to understand the basic optics of DBRs. Moreover, a list of publications and contribution to conferences arose from this work is reported at the end on this manuscript.

References

(1) John, S., *Phys. Rev. Lett.*, **1987**, 58, 2486-2489.

(2) Yablonovitch, E., *Phys. Rev. Lett.*, **1987**, 58, 2059-2062.

(3) Comoretto, D., *Organic and Hybrid Photonic Crystals*. Springer: Cham, 2015.

(4) Skorobogatiy, M.; Yang, J., *Fundamentals of photonic crystal guiding*. Cambridge University Press: Cambridge, 2009.

(5) Joannopoulos, J. D.; Johnson, S. G.; Winn, J. N.; Meade, R. D., *Photonic crystals: molding the flow of light*. Princeton university press: Woodstock, 2011.

(6) Teyssier, J.; Saenko, S. V.; van der Marel, D.; Milinkovitch, M. C., **2015**, 6, 6368.

(7) Zhang, S.; Chen, Y., **2015**, 5, 16637.

(8) Vigneron, J. P.; Simonis, P., *Phys. B*, **2012**, 407, 4032-4036.

(9) Dumanli, A. G.; Savin, T., *Chem. Soc. Rev.*, **2016**, 45, 6698-6724.

(10) Photonic crystals market: https://www.alliedmarketresearch.com/photonic-crystals-

market. (accessed 11/12/2019).

(11) Manfredi, G.; Lova, P.; Di Stasio, F.; Rastogi, P.; Krahne, R.; Comoretto, D., *RSC Advances*, **2018**, 8, 13026-13033.

(12) Frezza, L.; Patrini, M.; Liscidini, M.; Comoretto, D., *J. Phys. Chem. C*, **2011**, 115, 19939 - 19946.

(13) Lova, P.; Cortecchia, D.; S. Krishnamoorthy, H. N.; Giusto, P.; Bastianini, C.; Bruno, A.; Comoretto, D.; Soci, C., *ACS Photonics*, **2018**, 5, 867-874.

(14) Shen, H.; Wang, Z.; Wu, Y.; Yang, B., *RSC Advances*, **2016**, 6, 4505-4520.

(15) Choi, S. H.; Byun, K. M.; Kim, Y. L., *ACS Photonics*, **2018**, 5, 881-889.

(16) Vigneron, J. P.; Pasteels, J. M.; Windsor, D. M.; Vértesy, Z.; Rassart, M.; Seldrum, T.; Dumont, J.; Deparis, O.; Lousse, V.; Biró, L. P.; Ertz, D.; Welch, V., *Phys. Rev. E*, **2007**, 76, 031907.

(17) Vignolini, S.; Rudall, P. J.; Rowland, A. V.; Reed, A.; Moyroud, E.; Faden, R. B.; Baumberg, J. J.; Glover, B. J.; Steiner, U., *Proc. Natl. Acad. Sci.*, **2012**, 109, 15712-15715.

(18) Grimann, M.; Fuhrmann-Lieker, T., Biological photonic crystals. In *Organic and hybrid photonic crystals*, Comoretto, D., Ed. Springer International Publishing: Cham, 2015; pp 57-74.

(19) Chamaleonlab - http://chameleonlab.nl/. (accessed 11/12/2019).

(20) Calvo, M. E.; Míguez, H., *Chem. Mater.*, **2010**, 22, 3909-3915.

(21) Yu, W.; Shen, L.; Shen, P.; Long, Y.; Sun, H.; Chen, W.; Ruan, S., *ACS Appl. Mater. Interfaces*, **2014**, 6, 599-605.

(22) Lova, P.; Bastianini, C.; Giusto, P.; Patrini, M.; Rizzo, P.; Guerra, G.; Iodice, M.; Soci, C.; Comoretto, D., *ACS Appl. Mater. Interfaces*, **2016**, 8, 31941–31950.

(23) Lova, P.; Manfredi, G.; Boarino, L.; Comite, A.; Laus, M.; Patrini, M.; Marabelli, F.; Soci, C.; Comoretto, D., *ACS Photonics*, **2015**, 2, 537-543.

(24) Lova, P.; Manfredi, G.; Boarino, L.; Laus, M.; Urbinati, G.; Losco, T.; Marabelli, F.; Caratto, V.; Ferretti, M.; Castellano, M.; Soci, C.; Comoretto, D., *Phys. Status Solidi C*, **2015**, 12, 158-162.

(25) Mönch, W.; Dehnert, J.; Prucker, O.; Rühe, J.; Zappe, H., *Appl. Opt.*, **2006**, 45, 4284-4290.

(26) Mönch, W.; Dehnert, J.; Jaufmann, E.; Zappe, H., *Appl. Phys. Lett.*, **2006**, 89, 164104.

(27) Convertino, A.; Capobianchi, A.; Valentini, A.; Cirillo, E. N. M., *Sens. Actuators, B,* **2004**, 100, 212-215**.**

(28) Convertino, A.; Capobianchi, A.; Valentini, A.; Cirillo, E. N. M., *Adv. Mater.***, 2003**, 15, 1103 - 1105**.**

(29) Convertino, A.; Valentini, A.; Ligonzo, T.; Cingolani, R., *Appl. Phys. Lett.***, 1997**, 71, 732-734**.**

Chapter 1: Vapor Sensing Technologies

This Chapter highlights the importance of developing simple detection systems for the qualitative and quantitative analysis of vapor analytes. The importance of atmosphere monitoring has been indeed widely recognized and recently the possibility to assess the quality of air in sealed containers revealed new perspectives in health preservations and device encapsulation.

The first Paragraph reviews the current technologies for the qualitative and quantitative detection of volatile species focusing on their figures of merit and main limitations. Then, it introduces new colorimetric technologies aimed to simplify the analyses which disclose compatibility with packaging systems. Current technologies for the measurement of diffusion coefficient are also reviewed. Polymeric and mesoporous DBR sensors are then reviewed and compared. Last, this section proposes a new method that exploit polymer DBRs to achieve contemporary analysis of volatile species and determination of their diffusion coefficient within the polymer themselves by simple UV-Vis spectroscopy.

This section is substantially published at:

Lova, P.; Megahd, H.; Comoretto, D. Thin Polymer Films: Simple Optical Determination of Molecular Diffusion Coefficients. ACS Applied Polymer Materials **2020**, 2, 563-568

Lova, P. et al. Flory-Huggins Photonic Sensors for the Optical Assessment of Molecular Diffusion Coefficients in Polymers, ACS Appl. Mater. Interfaces**, 2019**, 11, 16872-16880**.**

Lova, P. et al., Advances in Functional Solution Processed Planar One-Dimensional Photonic Crystals, *Adv. Opt. Mater.***, 2018**, 6, 1800730-26**.**

The assessment of volatile organic compounds (VOCs) in the vapor phase plays a key role in the evaluation of potential health risks in industrial and urban areas. Recently, it revealed great relevance also in packaging of goods and device encapsulation.[1-2] Indeed, fast assessment of analytes penetrating in the packaging itself would allow to identify the formation of degradation markers within the sealed environment, or the intercalation of harmful molecules from the external air.[1-2] The possibility to implement the packaging with sensors based on simple colorimetric response that do not require any chemical target and that can identify, quantify and measure the diffusivity of analytes in the packaging itself could then allow direct assessment of food and goods quality directly on the shelf. On the other hand, current technologies for the determination of analytes in air are still far away from this standard.

This Chapter reviews the technologies used currently for the qualitative and quantitative detection of molecules in the vapor and gas phases introducing their figures of merit and limitations. It will then describe the technologies used for the determination of diffusion coefficients. Last, it will describe the state of the art of colorimetric photonic sensors and propose a new approach to achieve both chemical analyses and determination of diffusion coefficients via UV-Vis spectroscopy.

1.1 Assessment of Vapor Phase Analytes

Despite the lack of regulations for the monitoring of packaged goods during their shelf-life, the importance of atmospheric VOCs[89] monitoring has been largely recognized. VOCs cause indeed several toxic effects,[12] and are often associated to development of cancer[3] and formation of tropospheric ozone,[4] which results in global warming,[5] formation of new pollutants[7]and can causes respiratory illness.[6] As a consequence, detection of atmospheric vapor analytes is ruled by national regulations, which vary country by country. In general, quantitative analyses can be performed with portable detectors, while qualitative ones require laboratory equipment.

The Figures of merit of a detection system vary strongly depending on the polluted environment. In industrial areas, where pollutant species and sources are usually known, detection of small concentrations is necessary to avoid excessive and prolonged exposures. In urban environments, the large amount of activities that may release these compounds makes instead their identification of primary importance to evaluate the risks. Then, while in industrial area the main requirements are sensitivity and low detection limit, in urban areas the identification of the pollutant, and thus the selectivity of the detection system, is most critical.

In the next Paragraphs, we will introduce the established technologies used to monitor air quality, highlighting the figure of merit of detection systems.

1.1.1 Sensors for Quantitative Analyses

As mentioned before, in industrial plants, sensors must detect very small concentrations. Indeed, analytes such as formaldehyde and benzene show carcinogenic effects in concentrations below 1 ppm. In these cases, the operators are provided with portable detectors with high sensitivity and low detection limit. Although they sensitivity, these detectors are not qualitative and produces additive responses to the presence of different analytes.[14–16] Among the most diffuse portable detectors, there are metal oxide sensors, colorimetric indicator tubes and infrared point sensors (Figure 1.1).

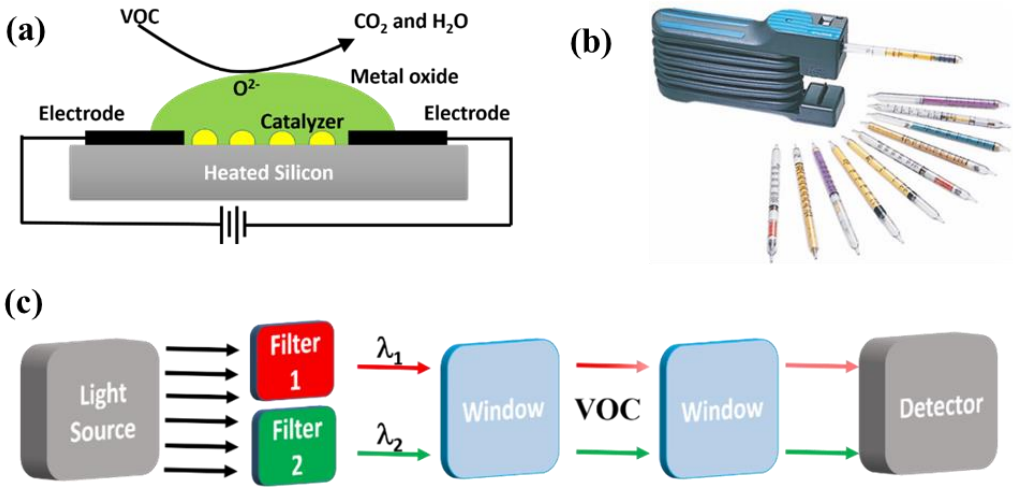

Figure 1.1: (a) Schematic of a metal oxide detector for VOC vapors analysis. (b) Commercial colorimetric reaction tube detector with volumetric hand-pump and colorimetric glass tubes for different analytes.[21] (c) Schematic of infrared point detector components.

Metal Oxide Sensors rely on a catalyzed oxidation of the analytes operated by a metal oxide (Figure 1.1 a). This favor electrons injection into the latter modifying its resistance and generating a signal.[17] These sensors show sensitivity down to few part per billion but lack of selectivity and the presence of ozone and water generates false readings. [18,19]

Colorimetric indicator tubes are glass tubes containing specific colorimetric chemical targets. Figure 1.1 b shows a commercial system where a volumetric hand pump is connected to the

glass tubes with the target. The color variation is compared with a database to retrieve analyte concentration. These tests can detect concentrations from few part per million to few percent, but accuracy is generally low.[20]

Portable infrared sensors use infrared spectroscopy to detect hydrocarbons. These sensors use two wavelengths: a measuring one, corresponding to the analyte absorption, and a reference one, which is detuned. The analyte concentration is determined by comparison between the relative intensity of the two beams (Figure 1.1 c).[22] These systems show high sensitivity, but different analytes with absorption in the same spectral range induces false readings.

1.1.2 Sensors for Qualitative Analyses

Portable detectors do not allow analytes identification, so unknown leaking sources necessitate laboratory analyses. This process requires sampling of large amount of air and analytes separation before the measurements. Air is sampled over long periods in areas selected accounting for meteorological data and distance from the source. The air is collected in pressurized canisters[23] or it is possible to concentrate the analytes using membranes,[24–26] solvent extraction, or cryogenic methods.[27–31] After concentration, the analytes are separated via gas chromatography.[3233] For qualitative analyses, two detectors are usually connected to the column in series or parallel configuration.[34] For systems connected in series, the first module must perform non-disruptive analyses, posing some constraint to the detector choice. Parallel detectors can instead be disruptive, but splitting the sample causes loss of sensitivity.[35] The most employed detectors are mass spectrometers,[36] together with photoionization[37] and flame ionization detectors.[37] All of them show high sensitivity and low detection limits, but requires trained users and continuous maintenance.

In summary, qualitative techniques available for the detection of vapor analytes need complex sampling and analyses, therefore new qualitative methods that can minimize instrumentation are desirable for extensive on-site air monitoring of VOCs. Moreover, sensitive technologies that does not require large amount of air are desirable to apply these systems to packaging.

1.1.3 New Colorimetric Technologies

Sensors relying on color[44–53] or photoemission[38–43] variation arising from the interaction between analytes and chemical targets are increasingly studied to allow devices with simpler

readout than current techniques. These detectors use arrays of targets with different reactivity that generate a characteristic color matrix allowing analyte identification via chemometric analysis. The receptors can be metalloporphirines,[45,55] reducing agents,[56] conjugated systems such as functionalized polyacetylenes[49–51,57] or even mixture of labels.[58,59] The main advantage of these sensors is their low cost, but the response transduction relies on the color variation of large matrices, which requires complex analysis and comparison with reference libraries. The response of a typical device is reported in Figure 1.2,[54] where an array of 36 labels containing pH indicators, solvatochromic dyes, and metalloporphirines shows different colorimetric changes to vapors (Figure 1.2 a). The response is analyzed by a camera to extract a color difference matrix (Figure 1.2 b), that is then used to create a library of responses for analytes identification (Figure 1.2 c). A clear disadvantage of such systems is the complex procedure necessary to determine analyte species and concentrations.

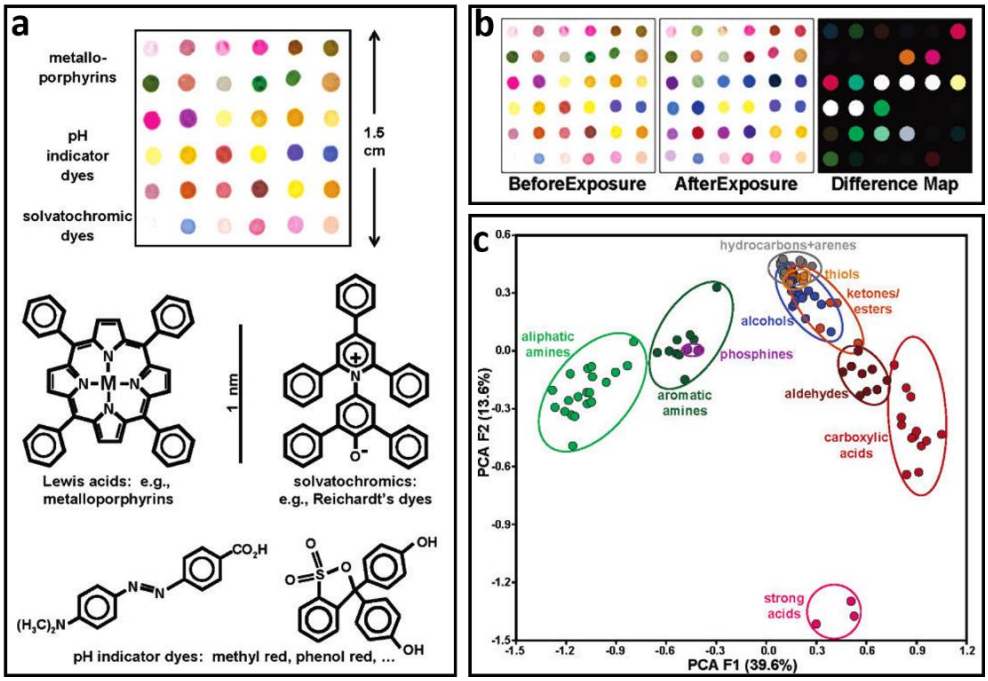

Figure 1.2: Chemically labelled colorimetric array sensor for vapor VOCs identification.[54]

Unfortunately, the need for chemical targeting increases complexity of data interpretation. Moreover, determination of concentration levels is very difficult, and makes this technology hardly suitable for extensive monitoring of air quality and for packaging technologies. On the

other side of the coin, these colorimetric sensors demonstrate selectivity without collection of large amounts of air, analyte separation and specific laboratory equipment, thus strongly simplifying the qualitative assessment of vapor molecules.

1.2 Assessment of Molecular Diffusion Coefficients in Polymers

As mentioned previously, beside chemical analyses, this Thesis project aim evaluate the diffusivity of molecular species in polymer films. Assessing the presence of degradation byproducts or the diffusion of external hazardous molecules in the packaging could indeed increase shelf-life and device performances. While pakaging environment is commonly not assesed during the shelf-life, diffusion coefficients in polymer films are evaluated *ex-situ* measuring sorption rates of the molecular species in the polymer. These measurements are performed via gravimetric or pressure decay methods. In both cases a polymer film/slab is exposed to an analyte to determine its mass intake along the exposure (Figure 1.3). In gravimetric measurements the sample is placed in a chamber at constant temperature and pressure and the sample weight is monitored during the exposure.[3] In the second case, the pressure of the chamber is not mantained constants and its decay is linked to the polymer mass intake.[4-5] The sorption curves retrived are used to determine the diffusivity at the non-steady state and the equilibrium solubility at the steady state. Indeed, The sorption typically exhibits two regimes: a non-steady-state one regulated by the diffusivity of the molecules within the polymer matrix (red part of the curve in Figure 1.3), and a steady-state one that depends on the polymer-solvent equilibrium solubility at saturation (black part of the curve in Figure 1.3).

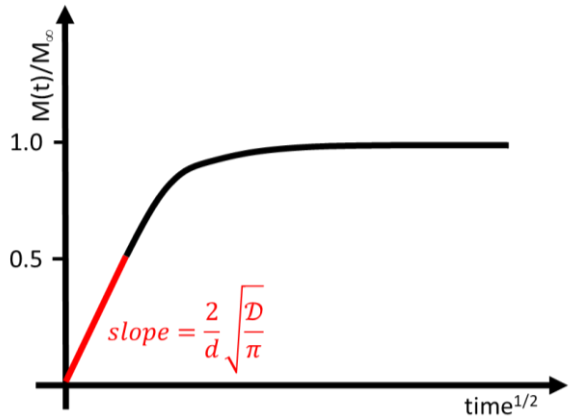

Figure 1.3: Typical gravimetric sorption curve for a polymer slab. The red line highlight the diffusive regime, while the black color represent the accumolation regime.

For a thin polymer slab with thickness *d*, such that the diffusion of the molecular species cannot occour through the sides (one-dimensional diffusion), the variation of concentration c (z,t) along the *z* axis can be described by the second Fick's law, $\frac{\partial c}{\partial t} = \left(\mathcal{D}\frac{\partial^2 c}{\partial z^2}\right)$, where $\mathcal{D}$ is the diffusion coefficient, c is the concentration of the molecular species within the slab and z is the diffusion distance. The boundary conditions are c (z, t) = 0 at t=0 for each z, then at $t > 0$ the surface concentration is equal to the equilibrium one, and $\frac{\partial c}{\partial z} = 0$ at $z = d$ for each t. Following this approach, one can espress the mass intake as decribed by Crank:[6-7]

$$\frac{M(t)}{M(\infty)} = \frac{\Delta\lambda(t)}{\Delta\lambda(\infty)} = \sqrt{\frac{Dt}{d^2}}\left(\sqrt{\pi} + 2\sum_{n=1}^{\infty}(-1)^n ierf\left(\frac{nd}{2\sqrt{Dt}}\right)\right) \quad (1.1)$$

where $ierf$ is the complex error function.[6] For short exposure time, where $M(t)/M(\infty) < 0.5$ the second term of Equation 1.1 can be neglected, and:[6,8]

$$\frac{\Delta\lambda(t)}{\Delta\lambda(\infty)} = \frac{2}{d}\sqrt{\frac{\mathcal{D}}{\pi}}\sqrt{t}. \quad (1.2)$$

Therefore, $\mathcal{D}$ can be evaluated from the angular coefficient of the linear part of the curve (Figure 1.3, highlighted in red). This approach assumes constant thickness of the polymer slab.[9] Beside gravimetric methods, other techniques such as microscopy[10] and infrared absorption,[11] which remained substantially unchanged for the last few decades, are employed. As well as gravimetric techniques, these methods need dedicated equipment and cannot be performed *in-situ.* Moreover, when very small polymer masses are involved, dedicated expensive and time consuming procedures such as nuclear magnetic resonance,[12-13] infrared spectroscopy,[14] and neutron reflectometry[15] are needed. Some attempts to measure diffusivity in thin films via UV-Vis spectroscopy have been done using chromophore analytes,[16] but the use of these colored compounds aims to detect opportunely labelled molecules and then, it cannot be employed for uncolored species. In this scenario, research for new low-cost, simpler, and portable technologies to gather lab-on-chip devices is strongly pursued.

1.3 Distributed Bragg Reflectors (DBRs): Vapor Sensing Mechanism

In regard of both the determination of vapor species and diffusion coefficients, PhC sensors could represent a paradigm changer. Many of these structures were demonstrated sensitive to chemical and biological molecules.[17-25] The sensing process relies on the modification of the optical PhC response triggered by external perturbations, like analyte diffusion in the structure. In this sense, polymer an porous PhCs based on silk,[26] cellulose and its derivatives,[27-30] block-copolymers,[31-38] gratings,[39-40] opals,[29, 41-49] molecularly imprinted polymers, colloidal crystals,[50-51] porous inorganic[52-55] and hybrid[56-57] multilayered structures, are highly sensitive to both liquid and gas analytes and offer low detection limits and high sensitivity. Among PhCs, low fabrication costs, ease of manufacturing and of integration in lab-on-a-chip devices made polymer and inorganic mesoporous DBRs[60] interesting for the sensing of vapor molecules.[61–67] In particular, mesoporous multilayers made of sintered metal oxide nanoparticles processes from solution are highly researched.[58] For this reason, we will use them as a benchmark for DBR sensing capabilities. DBRs consist in a stack of media with different refractive index alternated periodically (inset of Figure 1.4 a).[68] Reflection and refraction at every interface are responsible for their PBGs, manifested as maxima in its reflectance spectra (see Appendix A.1 and A.2 for details). Figure 1.4 b shows the calculated spectra for a polymer (black line) and a mesoporous inorganic (red line) DBR made of 15 +1 periods. The reflection peak assigned to the PBG of the inorganic DBR is more intense and about 5 times broader than for the polymer lattice. As explained in Appendix A.3, this difference arises from the high dielectric contrasts typical of inorganic material pairs compared to those available for polymers.

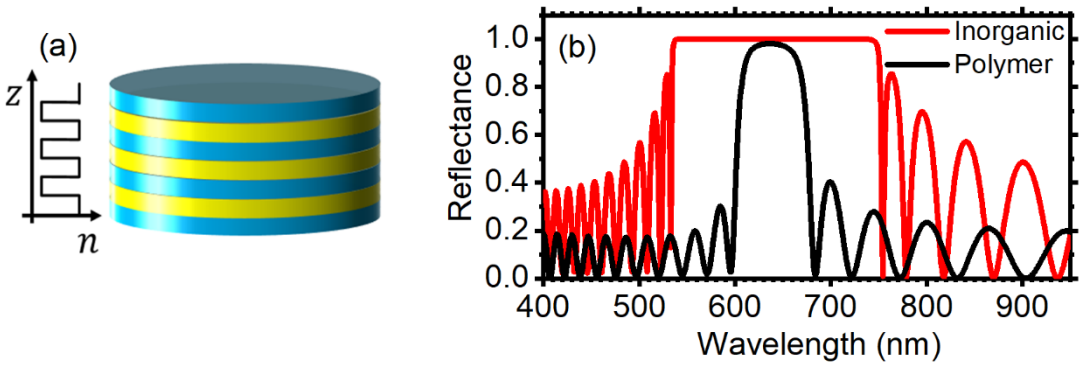

Figure 1.4: a) Shecmatic of a DBR architecture. b) Calculated spectra for DBRs made of cellulose acetate and polystyrene (black line) and of TiO_2 and SiO_2 (red line).

While large dielectric contrast is desirable for light control applications (Chapter 7),[69] it may hinder sensitivity and increase detection limit in sensing. Indeed, broad PBGs typically do not undergo large spectral variations. Then, polymer structures appear more suitable to this task.

To illustrate the differences in the optical response of inorganic mesoporous and polymer DBRs, it is first necessary to explain their sensing mechanism in more details. The phenomena occurring in the DBR upon exposure to analyte vapors can be related to its spectral response by simple equations. As shown in Appendix A.4, the Bragg Snell's law describes the spectral position of a DBR PBG (λ_b) as a function of the lattice periodicity (D), its effective refractive index (n_{eff}) and the angle of incidence of light (θ):

$$m\lambda_b = 2D\sqrt{n_{eff}^2 \sin^2\theta} \tag{1.3}$$

When a molecule penetrates the DBR, its effective refractive index and/or periodicity are affected, modifying the spectral position of the PBG. The variation of the dielectric contrast also affects the intensity of the reflectance peak (R) as described by Equations 1.4,

$$R \propto 1 - 4\left(\frac{n_1}{n_2}\right)^{2N} \tag{1.4}$$

which defines the reflectance intensity as a function of the dielectric contrast and the number of periods (N) in $\lambda/4$ condition (See Appendix A). The PBG width ($\Delta\omega/\omega_0$) is also affected by the presence of the analyte. In $\lambda/4$ condition, one can define the width as a function of the dielectric contrast:

$$\frac{\Delta\omega}{\omega_0} = \frac{4}{\pi}\frac{|n_2 - n_1|}{n_2 + n_1} = \frac{4}{\pi}\frac{\Delta n}{n}. \tag{1.5}$$

These simple equations allow describing the differences in the optical behavior of DBR sensors during the penetration of an analyte.

1.3.1 Response in Inorganic and Polymer DBR Sensors

As mentioned above, the dielectric contrast in the DBR can strongly affect its response. To explain this concept,

Figure 1.5 compares the calculated responses to an analyte for inorganic porous and polymer DBRs. The spectrum of the inorganic structure is modelled for 4+1 periods of media with comparable thickness and volumetric porosity (black line of

Figure 1.5 a). The spectrum shows a ~350 nm broad PBG which ranges from 430 nm to 790 nm with intensity close to the unit in the entire range. When an analyte with refractive index n_a penetrates the porous DBR, being $n_a > n_{air}$, the effective refractive index can only increase, and the PBG simply red shifts (blue line of

Figure 1.5 a). The mechanical rigidity of the layers does not allow variations of D. Although the optical response of these systems is straightforward and easy to interpret, the broad PBG often makes evaluation of the overall spectral response difficult.[73]

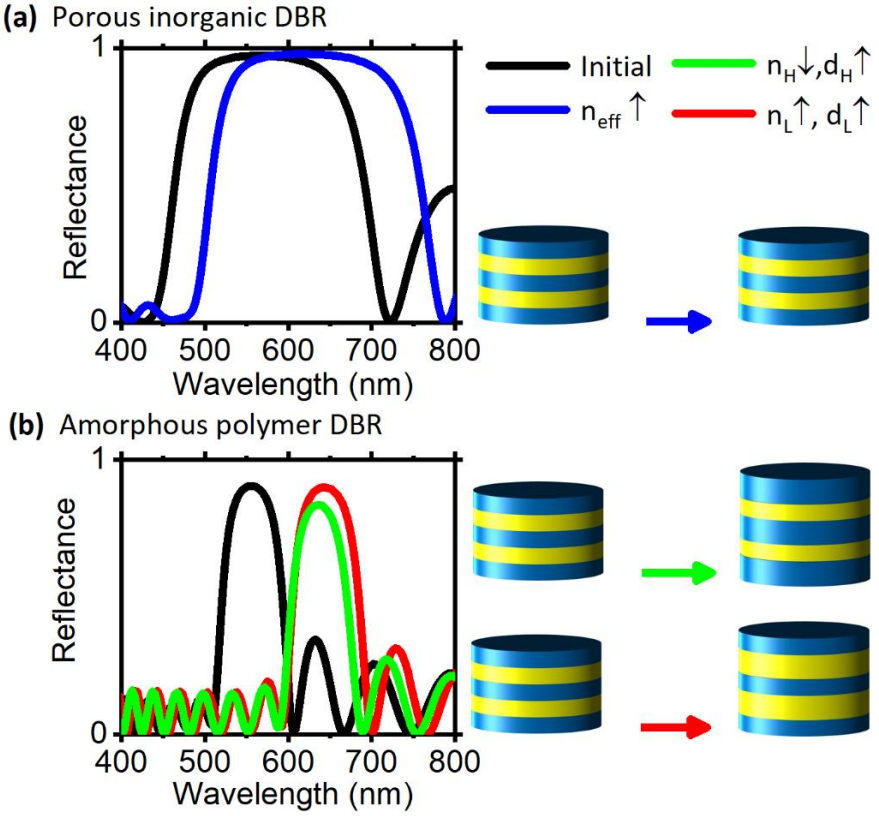

Figure 1.5: Schematic of the optical response induced by the analyte penetration in a) inorganic mesoporous and b) amorphous polymer DBRs.

For polymer DBRs, the lower dielectric contrast and sharp PBGs make the response much stronger. Moreover, the polymers ease of swelling (variation of D in Eq. 1.3) further enhances the response. The black line of

Figure 1.5 b indicates the calculated reflectance spectrum for 10+1 periods of two polymers with comparable thicknesses and refractive indexes $n_H = 1.68$ and $n_L = 1.46$. The spectrum shows a maximum of reflectance at about 550 nm, with band width of ~100 nm. When an analyte penetrates the multilayer, it induces both thickness and refractive index variation. The final position and intensity of the PBG is then defined by the combined variation of n_{eff} and D, as described by Equations 1.3 and 1.4. For sake of simplicity, we consider the variation of refractive index and thickness of a single medium at a time.

Figure 1.5 b shows a schematic of the processes occurring after the intercalation of an analyte with refractive index $n_a = 1.5$ within the DBR. When one of the polymer layers is swollen, *D* increases inducing a red shift of the PBG (green and red lines in

Figure 1.5 b). Moreover, if the analyte induces a decrease of the dielectric contrast, the intensity and width of the PBG will decrease accordingly (green line), and vice versa.

For what concern analytes permeation, polymer and mesoporous inorganic DBRs act as efficient membranes, where the permeation is ruled by diffusion mechanisms driven by a gradient of chemical potential at the two sides of the membrane. The ease of transport of each species is quantified by the membrane permeability ($\wp_i$). In the case of photonic sensors, the driving force is provided by the different concentrations at the two side of the DBR. For ideal gases, the flow (J) of a species through a membrane with thickness L along the diffusion direction can be related to the pressure difference ($p_i' - p_i''$) by the Fick's Law:

$$J = \frac{\wp_i}{L}(p_i' - p_i'') \tag{1.6}$$

Nowadays, DBR sensors rely on two main diffusion mechanisms. The first is typical of mesoporous structures, takes the name of Knudsen diffusion, and rules molecular diffusion in a membrane with pore dimension comparable or larger than the permeating molecules (Figure 1.6 a). In this case, light and smaller molecules diffuse faster than those with larger size and

weight, also allowing molecular sieving (Figure 1.6 b). In the case of vapor and gas analytes, this process may also favor capillary condensation, which causes strong refractive index changes within the DBR and then a variation of the DBR spectral response much larger than for simple vapor permeation. The second mechanism is instead typical of polymer DBRs, which often behave as dense membranes where solution-diffusion rules the permeation. In this case, the permeating elements are first dissolved into the membrane and then diffuse through it (Figure 1.6 c).[59-60] To be dissolved, these elements must have chemico-physical affinity with the dense matrix.

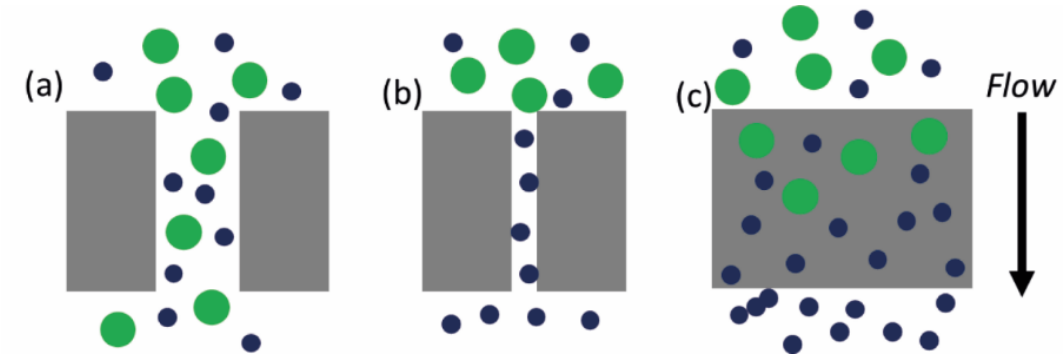

Figure 1.6: a) Knudsen diffusion through pores and (b) molecular sieving; (c) solution diffusion through dense membranes.

As mentioned above, the permeability of mesoporous DBR sensors, which allow capillary condensation and spectral responses, attract large interest in sensing.[61-63] In this regard, Ozin's group provided many examples of mesoporous structures made of silica, titania[56] and clay[64] sensitive to toluene,[65] ethanol,[56] food degradation by-products[66] and other organic molecules.[64] In this case, simple analysis of the PBG spectral shift to investigate the permeation process does not provide qualitative and quantitative information, and multivariate analysis must often be applied.[64, 66] Mesoporous inorganic DBR sensors usually achieve detection of about 10^{-1} ppm.[9, 67-68]

Recently, polymer DBRs aroused considerable interest due to remarkable spectral responses amplified by the ease of swelling of macromolecules. Moreover, relatively sharp PBGs is advantageous in term of sensitivity and to lower the detection limit. Indeed, block copolymer DBRs demonstrated high sensitivity and optical responses easily detectable by the naked eye for analytes in the liquid phase.[69-71] Concerning the detection of vapors, the first report on

polymer DBRs was by Convertino and co-workers. They demonstrated the detection of toluene, acetone and short chain alcohols using layers of a neat fluorinated polymer alternated to layers of the same polymer doped with gold nanoparticles fabricated by thermal vapor deposition.[72-74] Following this work, Zappe *et al.* reported cross-linked DBR made of polystyrene (PS) and poly (methyl methacrylate) (PMMA) sensitive to acetone and toluene.[75-76] However, from the fabrication point of view, chemical vapor deposition is costly and time consuming, while cross-linking introduces an additional step in the growth, which can be avoided using amorphous or even semi-crystalline polymers.

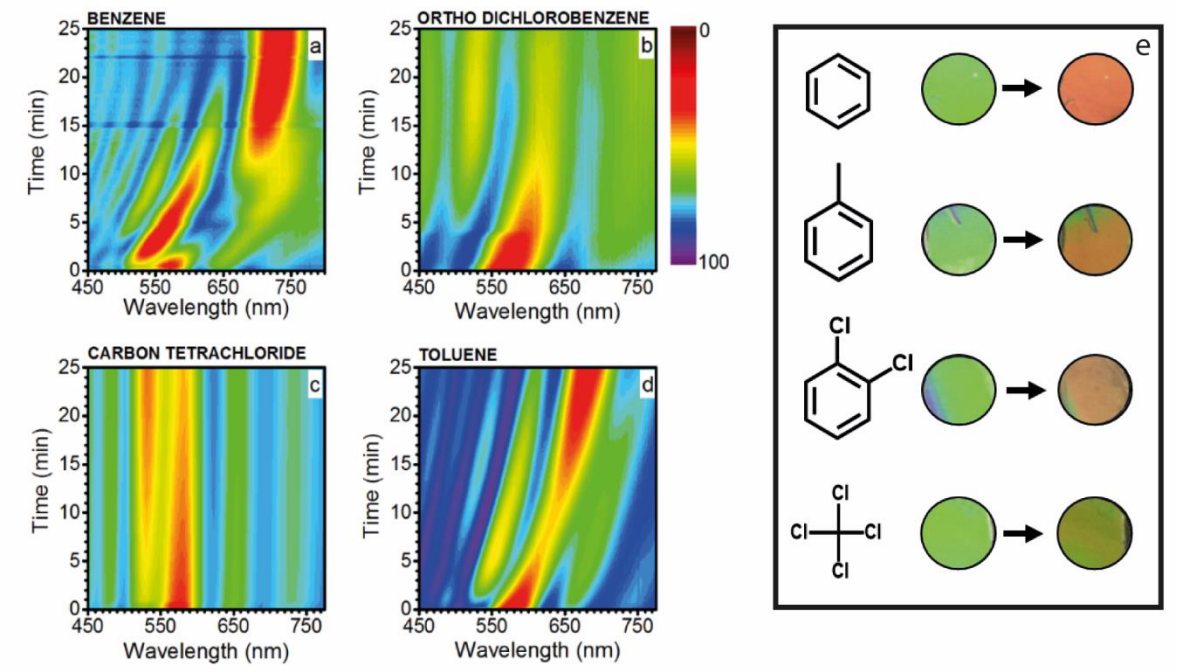

Figure 1.7: Contour plots of a PPO:CA DBR transflectance spectra upon 25 minutes of exposure to a) benzene, b) 1,2-dichlorobenzene and c) carbon tetrachloride, and d) toluene. (e) Digital images of the sensor surface collected before (right) and After (left) exposure to the four vapors.[9]

DBR vapor sensors fabricated by spin-coating of commodity polymers demonstrated sensitivity to several of organic solvents.[9, 77-78] For instance, PS:CA DBRs, where the PS matrix was doped with ZnO nanoparticles to enhance free-volume and then permeability, showed toluene sensitivity below 1 ppm and lower detection limit of 20 ppm.[77] In this case, selectivity relies on the different diffusion kinetics of the analytes within the DBR and on the steady state equilibrium response. Indeed, both the optical response and its kinetics are affected by physico-

chemical solvent-analyte interactions, analyte molecular size, and polymer free volume. The mechanism was shown in DBRs made of alternated layers of CA and poly (p-phenylene oxide) (PPO) as active medium for aromatic compounds.[9] PPO is well-known for its remarkable sorption properties correlated to its crystallinity.[79-80] The analytes intercalation in the structure brings to guest induced crystallization of the PPO layers[81] inducing changes in the refractive index and in the response kinetics.[9] These last favor an easy recognition of very similar analytes in term of molecular size and polarity such as benzene and toluene, beside carbon tetrachloride and 1,2-dichlorobenzene (Figure 1.7 a-d).[9] The response, can be perceived by the naked eye providing an easy to read safety system (Figure 1.7 e).[9]

1.4 Flory-Huggins Photonic Sensors (FHPSs)

Notwidstanding previous works clearly demonstrated that polymer-solvent interacion have a key role in sensitivity and selectivity of polymer DBRs sensors, these process were not fully understood yet. This Thesis proposes to describe these interaciton in terms of Flory-Huggins and Hildebrand parameters, which well describes the ability of a molecule to diffuse and interact with the polymer in the DBR sensors, and in turn the sensitivity to the analyte itself. For this reason, these sensors will be called Flory-Huggins photonic sensors.[82-83] This Paragraph proposes then new FHPSs that can both work as label-free selective colorimetri sensors and be employed to determine the diffusion kinetics within the polymer matrices themselves via UV-Vis spectroscopy.

As an ideal system to explain the working principle of FHPSs, we will employ the DBR sketched in Figure 1.8 a. The structure provides a typical optical response shown as a black line in the reflectance spectrum of Figure 1.8 b. The spectrum displays peak assigned to the PBG. When the DBR is placed in air polluted with a vapors, the molecules permeate into its structure, and can swell the one or both the mateirals composing the layers. As the diffusivity depends on the analyte solubilization, one can use the Flory-Huggins parameter (χ_{ap}^{H}, neglecting entropic contribution) as in indicator for compatibility. χ_{ap}^{H} can be expressed as a function of the analyte molar volume (V^{M}) and of the solubility parameter for the pairs. The latter is defined from the Hildebrand parameters of the two components of the mixtures (δ_P, δ_A) as $\Delta\delta^2 = (\delta_P - \delta_A)^2$, which expresses the difference of cohesive energy between the analytes and the polymers, the smaller is $\Delta\delta^2$, the larger is the solubility.[84-85]

$$\chi_{AP}^{H} = V^{M} \frac{\Delta\delta^2}{RT} \tag{1.7}$$

where R is the gas constant and T the temperature.[58] Then, the choice of suitable polymers as active media through their Flory-Huggins parameter would make them efficient detectors foe a variety of analytes in the vapor phase, and allows to extend the method to a large amount of chemical species. The interaction between the polymer and the analyte results in a variation of the thickness (swelling) and refractive index of the layers, and thus, of the light optical path (Figure 1.8 a). In turn, such variation affects the PBG spectral position, according Equation 1.3. Indeed, the red line spectrum of Figure 1.8 b shows that after 90 min of exposure the PBG red-shifts of about 13%.[86]

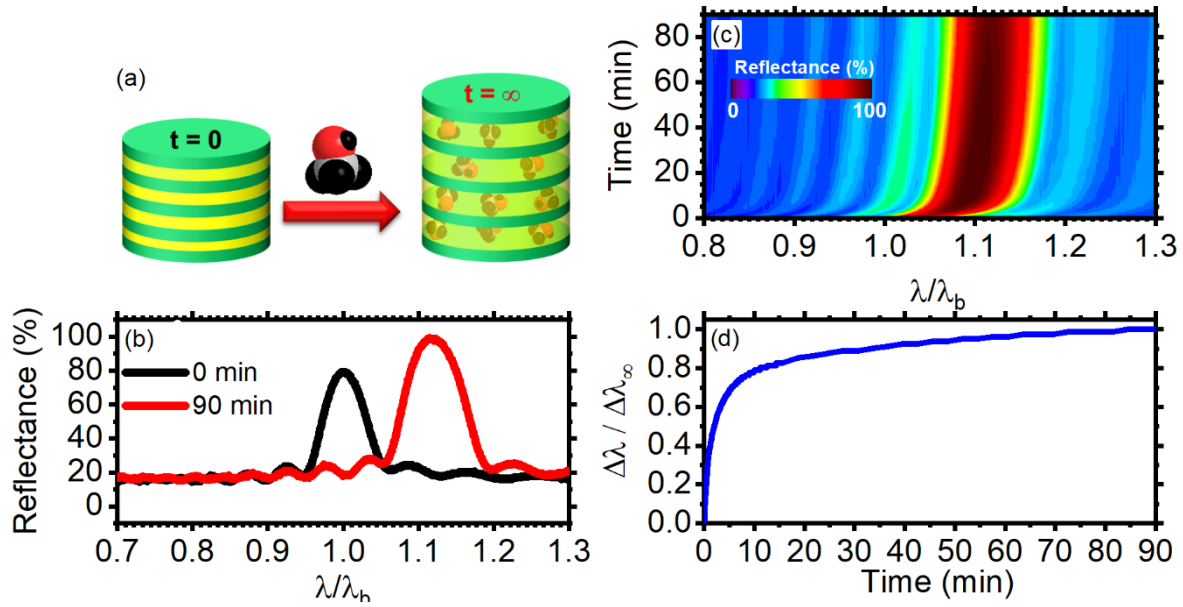

Figure 1.8: (a) Scheme of the intercalation of an analyte into FHPS, (b) reflectance spectra of a DBR before (black line) and after (red line) 90 min of exposure, (c) contour-plot of the temporal evolution of the FHPS spectra, and (d) normalized profile of the first (blue line) and second (open dots) order PBGs spectral position during the exposure.

Figure 1.8 c illustrates the dynamics of the optical response as a contour plot where the exposure time and the wavelength are represented as the y- and as the x- axis respectively, while the reflectance intensity is reported as a color code. The PBG feature is visible in red-tones, while the spectra background is represented in blue tones. The red-shift of the PBGs is initially very fast. Then, the dynamics slows down, and the system reaches the equilibrium. To highlight the temporal evolution of PBG spectral positions, Figure 1.8 d shows the maximum

of intensity of each spectrum collected, which correspond to the PBG, versus the exposure time. These data represent then the dynamic evolution of the PBG after normalization by the respective value of shift at the steady-state. These dynamic responses can be employed as the gravimetric sorption curves described in Paragraph 1.2.[6] Indeed, the penetration of a molecular species into the polymer films and their possible swelling affect both the refractive indexes (n_L and n_H) and geometrical thicknesses (d_L and d_H) of the layers. In turn, their optical thickness ($n * d$) is modified. Because for vapor analytes $\Delta d/d(0) \gg \Delta n/n(0)$,[77, 87-90] we can assume that the refractive index variation is negligible during the swelling process, $n(0) \approx n(t) \approx n(\infty)$ (see also Paragraph 1.3.1).[82] Then, because the volume variation occurs only along one direction, we can derive that, for additive volumes, the absorbed vapor mass, M(t), is proportional to the variation of thickness, which in turn affects the PBG spectral position.

$$\frac{M(t)}{M(\infty)} \div \frac{L(t) - L(0)}{L(\infty) - L(0)} \div \frac{\Delta\lambda(t)}{\Delta\lambda(\infty)} \tag{1.8}$$

where $M(\infty)$ is the mass of the molecular species permeated through the polymer film at the equilibrium obtained for an infinite exposure time ($t \to \infty$), $L = d_H + d_L$, $\Delta\lambda$ is the spectral shift of the PBGs at time t and at the equilibrium. Therefore, an effective diffusion coefficient $\mathcal{D}_{eff}$ can be evaluated from the angular coefficient of the linear part of the sorption curve of Figure 1.8 d, reported as $\Delta\lambda(t)/\Delta\lambda(\infty)$ versus $\sqrt{t}$. This approach assumes constant thickness and refractive index of the polymer slab accordingly to Crank model reported in Paragraph 1.2.[6] If we consider the early stages of the uptake process for which the thickness variation is below 20% of the total value, from Equation 1.2 we can derive $\mathcal{D}_{eff}$, with an error below 10%.[9] Similarly, the curves can be employed to distinguish the analytes diffusion kinetics, and then to identify them allowing to obtain information of the diffusing species and its diffusion coefficient with a single optical measurement.

References

(1) Janjarasskul, T.; Suppakul, P., *Crit. Rev. Food Sci. Nutr.*, **2018**, 58, 808-831.

(2) Sohail, M.; Sun, D.-W.; Zhu, Z., *Crit. Rev. Food Sci. Nutr.*, **2018**, 58, 2650-2662.

(3) Berens, A. R.; Hopfenberg, H. B., *J. Membr. Sci.*, **1982**, 10, 283-303.

(4) Vopička, O.; De Angelis, M. G.; Sarti, G. C., *J. Membr. Sci.*, **2014**, 449, 97-108.

(5) Flaconneche, B.; Martin, J.; Klopffer, M., *Oil Gas Sci. Technol.*, **2001**, 56, 245-259.

(6) Crank, J., *The Mathematics of Diffusion*. 2nd ed.; Oxford university press: Bristol, 1975.

(7) Linossier, I.; Gaillard, F.; Romand, M.; Feller, J. F., *J. Appl. Polym. Sci.*, **1997**, 66, 2465-2473.

(8) Fieldson, G. T.; Barbari, T. A., *Polymer*, **1993**, 34, 1146-1153.

(9) Lova, P.; Bastianini, C.; Giusto, P.; Patrini, M.; Rizzo, P.; Guerra, G.; Iodice, M.; Soci, C.; Comoretto, D., *ACS Appl. Mater. Interfaces*, **2016**, 8, 31941–31950.

(10) Mráček, A., *Int. J. Mol. Sci.*, **2010**, 11, 532-543.

(11) Ferrari, M.-C.; Catalano, J.; Giacinti Baschetti, M.; De Angelis, M. G.; Sarti, G. C., *Macromolecules*, **2012**, 45, 1901-1912.

(12) Meurer, B.; Weill, G., *Macromol. Chem. Phys.*, **2008**, 209, 212-219.

(13) Meier, R.; Herrmann, A.; Kresse, B.; Privalov, A. F.; Kruk, D.; Fujara, F.; Rössler, E. A., *ACS Macro Lett.*, **2013**, 2, 96-99.

(14) Davis, E. M.; Stafford, C. M.; Page, K. A., *ACS Macro Lett.*, **2014**, 3, 1029-1035.

(15) Xu, L.; Selin, V.; Zhuk, A.; Ankner, J. F.; Sukhishvili, S. A., *ACS Macro Lett.*, **2013**, 2, 865-868.

(16) Hall, D. B.; Miller, R. D.; Torkelson, J. M., *J. Polym. Sci. Part B Polym. Phys.*, **1997**, 35, 2795-2802.

(17) Hu, J.; Liu, S., *Macromolecules*, **2010**, 43, 8315-8330.

(18) Bisoyi, H. K.; Li, Q., *Acc. Chem. Res.*, **2014**, 47, 3184-3195.

(19) Fenzl, C.; Hirsch, T.; Wolfbeis, O. S., *Angew. Chem. Int. Ed.*, **2014**, 53, 3318-3335.

(20) Heuser, T.; Merindol, R.; Loescher, S.; Klaus, A.; Walther, A., *Adv. Mater.*, **2017**, 29, 1606842.

(21) Shen, H.; Wang, Z.; Wu, Y.; Yang, B., *RSC Advances*, **2016**, 6, 4505-4520.

(22) Dabrowski, M.; Cieplak, M.; Sharma, P. S.; Borowicz, P.; Noworyta, K.; Lisowski, W.; D'Souza, F.; Kuhn, A.; Kutner, W., *Biosens. Bioelectron.*, **2017**, 94, 155-161.

(23) López, C., *Adv. Mater.*, **2003**, 15, 1679-1704.

(24) Kittle, J. D.; Fisher, B. P.; Esparza, A. J.; Morey, A. M.; Iacono, S. T., *ACS Omega*, **2017**, 2, 8301-8307.

(25) Chen, C.; Dong, Z.-Q.; Shen, J.-H.; Chen, H.-W.; Zhu, Y.-H.; Zhu, Z.-G., *ACS Omega*, **2018**, 3, 3211-3217.

(26) Colusso, E.; Perotto, G.; Wang, Y.; Sturaro, M.; Omenetto, F.; Martucci, A., **2017**, 5**.**

(27) Zhao, Y.; Gao, G.; Liu, D.; Tian, D.; Zhu, Y.; Chang, Y., *Carbohydr. Polym.***, 2017**, 174, 39-47**.**

(28) Manfredi, G.; Mayrhofer, C.; Kothleitner, G.; Schennach, R.; Comoretto, D., *Cellulose***, 2016**, 23, 2853-2862**.**

(29) Wang, F.; Zhu, Z.; Xue, M.; Xue, F.; Wang, Q.; Meng, Z.; Lu, W.; Chen, W.; Qi, F.; Yan, Z., *Sens. Actuators, B***, 2015**, 220, 222-226**.**

(30) Perrin, L.; Nguyen, Q. T.; Sacco, D.; Lochon, P., *Polym. Int.***, 1997**, 42, 9-16**.**

(31) Fink, Y.; Urbas, A. M.; Bawendi, M. G.; Joannopoulos, J. D.; Thomas, E. L., *J. Lightwave Technol.***, 1999**, 17, 1963-1969**.**

(32) Chan, E. P.; Walish, J. J.; Thomas, E. L.; Stafford, C. M., *Adv. Mater.***, 2011**, 23, 4702-4706**.**

(33) Yoon, J.; Lee, W.; Thomas, E. L., *Macromolecules***, 2008**, 41, 4582-4584**.**

(34) Kang, Y.; Walish, J. J.; Gorishnyy, T.; Thomas, E. L., *Nat. Mater.***, 2007**, 6, 957-960**.**

(35) Guldin, S.; Kolle, M.; Stefik, M.; Lamgford, R.; Eder, D.; Wiesner, U.; Steiner, U., *Adv. Mater.***, 2011**, 23, 3664-3668**.**

(36) Parnell, A. J.; Tzokova, N.; Pryke, A.; Howse, J. R.; Mykhaylyk, O. O.; Ryan, A. J.; Panine, P.; Fairclough, J. P. A., *Phys. Chem. Chem. Phys.***, 2011**, 13, 3179-3186**.**

(37) Lim, H. S.; Lee, J.-H.; Walish, J. J.; Thomas, E. L., *ACS Nano***, 2012**, 6, 8933-8939**.**

(38) Noro, A.; Tomita, Y.; Shinohara, Y.; Sageshima, Y.; Walish, J. J.; Matsushita, Y.; Thomas, E. L., *Macromolecules***, 2014**, 47, 4103-4109**.**

(39) Palermo, G.; Barberi, L.; Perotto, G.; Caputo, R.; De Sio, L.; Umeton, C.; Omenetto, F. G., *ACS Appl. Mater. Interfaces***, 2017**, 9, 30951-30957**.**

(40) Weili, C.; D., L. K.; Jonas, K.; Margaret, H.; Hojeong, Y.; A., H. B.; T., C. B., *Adv. Opt. Mater.***, 2015**, 3, 1623-1632**.**

(41) Ben-Moshe, M.; Alexeev, V. L.; Asher, S. A., *Anal. Chem.***, 2006**, 78, 5149-5157**.**

(42) Janzen, M. C.; Ponder, J. B.; Bailey, D. P.; Ingison, C. K.; Suslick, K. S., *Anal. Chem.***, 2006**, 78, 3591-3600**.**

(43) Li, Y. Y.; Cunin, F.; Link, J. R.; Gao, T.; Betts, R. E.; Reiver, S. H.; Chin, V.; Bhatia, S. N.; Sailor, M. J., *Science***, 2003**, 299, 2045-2047**.**

(44) Nucara, L.; Piazza, V.; Greco, F.; Robbiano, V.; Cappello, V.; Gemmi, M.; Cacialli, F.; Mattoli, V., *ACS Appl. Mater. Interfaces***, 2017**, 9, 4818-4827**.**

(45) Min, K.; Kim, S.; Kim, S., *Proc. Natl. Acad. Sci.*, **2017**, 114, 6185-6190.

(46) Zhang, Y.; Fu, Q.; Ge, J., *Nat. Commun.*, **2015**, 6, 8510-6.

(47) Gam-Derouich, S.; Bourdillon, C.; Lakhdar Chaouche, S.; Coolen, L.; Maître, A.; Mangeney, C.; Schwob, C., *Angew. Chem. Int. Ed.*, **2017**, 56, 1433-7851.

(48) Yu, W.; Meng, L.; Elena, C.; Wenyi, L.; G., O. F., *Adv. Opt. Mater.*, **2018**, 6, 1800066.

(49) Palma, P. D.; Taddei, C.; Borriello, A.; Luca, G. D.; Giordano, M.; Iadicicco, A.; Campopiano, S.; Sansone, L., *IEEE Photonics J.*, **2017**, 9, 1-11.

(50) Xu, X.; Goponenko, A. V.; Asher, S. A., *J. Am. Chem. Soc.*, **2008**, 130, 3113–3119.

(51) Krüger, M.; Marso, M.; Berger, M. G.; Thönissen, M.; Billat, S.; Loo, R.; Reetz, W.; Lüth, H.; Hilbrich, S.; Arens-Fischer, R.; Grosse, P., *Thin Solid Films*, **1997**, 297, 241-244.

(52) Xie, Z.; Cao, K.; Zhao, Y.; Bai, L.; Gu, H.; Xu, H.; Gu, Z. Z., *Adv. Mater.*, **2014**, 26, 2413–2418.

(53) Hinterholzinger, F. M.; Ranft, A.; Feckl, J. M.; Ruhle, B.; Bein, T.; Lotsch, B. V., *J. Mater. Chem.*, **2012**, 22, 10356-10362.

(54) Lazarova, K.; Awala, H.; Thomas, S.; Vasileva, M.; Mintova, S.; Babeva, T., *Sensors*, **2014**, 14, 12207-12218.

(55) Exner, A. T.; Pavlichenko, I.; Baierl, D.; Schmidt, M.; Derondeau, G.; Lotsch, B. V.; Lugli, P.; Scarpa, G., *Laser Photonic Rev.*, **2014**, 8, 726–733.

(56) Choi, S. Y.; Mamak, M.; von Freymann, G.; Chopra, N.; Ozin, G. A., *Nano Lett.*, **2006**, 6, 2456-2461.

(57) Karaman, M.; Kooi, S. E.; Gleason, K. K., *Chem. Mater.*, **2008**, 20, 2262-2267.

(58) Lova, P.; Manfredi, G.; Comoretto, D., *Adv. Opt. Mater.*, **2018**, 6, 1800730-26.

(59) Baker, R. W., Overview of membrane science and technology. In *Membr. Technol. Environ. Appl.*, 2nd ed.; John Wiley & Sons, L., Ed. John Wiley & Sons, Ltd: Southern Gate, 2004; pp 1-14.

(60) Kerry, F. G., *Industrial gas handbook: gas separation and purification*. CRC Press: Boca Raton, 2007.

(61) Szendrei, K.; Jiménez-Solano, A.; Lozano, G.; Lotsch, B. V.; Míguez, H., *Adv. Opt. Mater.*, **2017**, 5, 1700663-n/a.

(62) Calvo, M. E.; Colodrero, S.; Hidalgo, N.; Lozano, G.; Lopez-Lopez, C.; Sanchez-Sobrado, O.; Miguez, H., *Energ. Environ. Sci.* , **2011**, 4, 4800-4812.

(63) Ruminski, A. M.; Barillaro, G.; Chaffin, C.; Sailor, M. J., *Adv. Funct. Mater.*, **2011**, 21, 1511-1525.

(64) Lotsch, B. V.; Ozin, G. A., *Adv. Mater.*, **2008**, 20, 4079-4084.

(65) Kobler, J.; Lotsch, B. V.; Ozin, G. A.; Bein, T., *ACS Nano*, **2009**, 3, 1669-1676.

(66) Bonifacio, L. D.; Ozin, G. A.; Arsenault, A. C., *Small*, **2011**, 7, 3153-3157.

(67) Pacholski, C., *Sensors*, **2013**, 13, 4694.

(68) Alexeev, V. L.; Das, S.; Finegold, D. N.; Asher, S. A., *Clin. Chem.*, **2004**, 50, 2353-2360.

(69) Kang, H. S.; Lee, J.; Cho, S. M.; Park, T. H.; Kim, M. J.; Park, C.; Lee, S. W.; Kim, K. L.; Ryu, D. Y.; Huh, J.; Thomas, E. L.; Park, C., *Adv. Mater.*, **2017**, 29, 1700084-n/a.

(70) Chiang, Y.-W.; Chou, C.-Y.; Wu, C.-S.; Lin, E.-L.; Yoon, J.; Thomas, E. L., *Macromolecules*, **2015**, 48, 4004-4011.

(71) Chiang, Y.-W.; Chang, J.-J.; Chou, C.-Y.; Wu, C.-S.; Lin, E.-L.; Thomas, E. L., *Adv. Opt. Mater.*, **2015**, 3, 1517-1523.

(72) Convertino, A.; Capobianchi, A.; Valentini, A.; Cirillo, E. N. M., *Sens. Actuators, B*, **2004**, 100, 212-215.

(73) Convertino, A.; Capobianchi, A.; Valentini, A.; Cirillo, E. N. M., *Adv. Mater.*, **2003**, 15, 1103 - 1105.

(74) Convertino, A.; Valentini, A.; Ligonzo, T.; Cingolani, R., *Appl. Phys. Lett.*, **1997**, 71, 732-734.

(75) Mönch, W.; Dehnert, J.; Prucker, O.; Rühe, J.; Zappe, H., *Appl. Opt.*, **2006**, 45, 4284-4290.

(76) Mönch, W.; Dehnert, J.; Jaufmann, E.; Zappe, H., *Appl. Phys. Lett.*, **2006**, 89, 164104.

(77) Lova, P.; Manfredi, G.; Boarino, L.; Comite, A.; Laus, M.; Patrini, M.; Marabelli, F.; Soci, C.; Comoretto, D., *ACS Photonics*, **2015**, 2, 537-543.

(78) Lova, P.; Manfredi, G.; Boarino, L.; Laus, M.; Urbinati, G.; Losco, T.; Marabelli, F.; Caratto, V.; Ferretti, M.; Castellano, M.; Soci, C.; Comoretto, D., *Phys. Status Solidi C*, **2015**, 12, 158-162.

(79) Rizzo, P.; Ianniello, G.; Longo, S.; Guerra, G., *Macromolecules*, **2013**, 46, 3995-4001.

(80) Tarallo, O.; Petraccone, V.; Daniel, C.; Fasano, G.; Rizzo, P.; Guerra, G., *J. Mater. Chem.*, **2012**, 22, 11672-11680.

(81) Guerra, G.; Daniel, C.; Rizzo, P.; Tarallo, O., *J. Polym. Sci., Part B: Polym. Phys.*, **2012**, 50, 305-322.

(82) Lova, P.; Manfredi, G.; Bastianini, C.; Mennucci, C.; Buatier de Mongeot, F.; Servida, A.; Comoretto, D., *ACS Appl. Mater. Interfaces*, **2019**, 11, 16872-16880.

(83) Gao, S.; Tang, X.; Langner, S.; Osvet, A.; Harreiβ, C.; Barr, M.; Spiecker, E.; Bachmann, J.; Brabec, C. J.; Forberich, K., *ACS Appl. Mater. Interfaces*, **2018**, 10, 36398–36406.

(84) Hansen, C. M., *Hansen Solubility Parameters: A User's Handbook*. 2nd ed.; CRC press: Boca Raton, USA, 2002.

(85) Cowie, J. M. G., *Polymers: Chemistry and Physics of Modern Materials*. Chapman&Hall: London, 1991.

(86) Scotognella, F.; Varo, S.; Criante, L.; Gazzo, S.; Manfredi, G.; Knarr III, R. J.; Comoretto, D., Spin-Coated Polymer and Hybrid Multilayers and Microcavities. In *Organic and Hybrid Photonic Crystals*, 1st ed.; Comoretto, D., Ed. Springer: Cham, 2015; Vol. 1, p 493.

(87) Bolton, B. A.; Kint, S.; Bailey, G. F.; Scherer, J. R., *J. Phys. Chem.*, **1986**, 90, 1207-1211.

(88) Watanabe, T.; Ooba, N.; Hida, Y.; Hikita, M., *Appl. Phys. Lett.*, **1998**, 72, 1533-1535.

(89) Ogieglo, W.; Wormeester, H.; Eichhorn, K.-J.; Wessling, M.; Benes, N. E., *Prog. Polym. Sci.*, **2015**, 42, 42-78.

(90) Habicht, J.; Schmidt, M.; Rühe, J.; Johannsmann, D., *Langmuir*, **1999**, 15, 2460-2465.

Chapter 2: Experimental Procedures

In the previous Chapter we observed that the strong spectral response and ease of fabrication of polymer structures, also on the square meter area scale, promise new generation lab-on-a-chip sensor that can be used without complex instrumentation and can be potentially implemented into packaging systems. This motivation drove us to develop new selective and selective polymer FHPSs, which beside the capability to identify and quantify vapor analytes, are powerful tools to assess the diffusivity of the latter within polymer matrices via UV-Vis spectroscopy. In this part, we describe methodologies and characterization techniques used through the Thesis work.

This section is substantially published at:

Lova, P.; Megahd, H.; Comoretto, D. Thin Polymer Films: Simple Optical Determination of Molecular Diffusion Coefficients. ACS Applied Polymer Materials **2020**, 2, 563-568

Lova, P. et al. Flory-Huggins Photonic Sensors for the Optical Assessment of Molecular Diffusion Coefficients in Polymers, ACS Appl. Mater. Interfaces**, 2019**, 11, 16872-16880**.**

Lova, P.; Manfredi, G.; Boarino, L.; Comite, A.; Laus, M.; Patrini, M.; Marabelli, F.; Soci, C.; Comoretto, D. Polymer Distributed Bragg Reflectors for Vapor Sensing. ACS Photonics **2015**, 2, 537-543.

2.1 Fabrication of FHPSs

The FHPSs were fabricated by dynamic spin-coating deposition of alternated solutions of high and low refractive index polymers.[1] The polymer-solvent couples employed were chosen to ensure sufficient dielectric contrast, mutual processability and optical response to the selected analytes (See Paragraph 3.2). The three systems investigated in this study are listed below:

1. PS:CA DBR - made of polystyrene (PS, Sigma Aldrich MW = 92 000) dissolved in toluene and cellulose acetate (CA, Sigma Aldrich, MW = 61 000) dissolved in diacetone alcohol.
2. PSZnO:CA DBR - This system is prepared like the previous one but the PS solution is loaded with ZnO nanoparticles synthetized via solvothermal route, modified and loaded as reported in details in Section 2.1.1.[2-3]
3. PVK:Hy DBR - made of poly-(N-vinylcarbazole) (PVK, Acros Organics, MW = 40 000) dissolved in toluene and Hyflon AD polymer (HY, Solvay Specialty Polymers).

All the polymers solutions had concentrations ranging from 30 to 50 mg/ml and were casted using rotation speed ranging from 120 RPS to 200 RPS.

Chapter 5 also reports the use on unstructured commercial polymeric films as sensors and the evaluation of diffusion coefficients in these matrices by optical spectroscopy. In this case a commercial polyvinyl chloride (PVC) cling film was employed. For the sensing measurements the film was supported on a silicon substrate to enhance back-reflectivity and simplify the measurements.

2.1.1 ZnO nanoparticles Synthesis and modification

To fabricate the PSZnO:CA DBR, ZnO nanoparticles were synthetized via a solvothermal route and their surface was modified to favor their dispersion in the non-polar polystyrene matrix. The modified nanoparticles were then loaded in polystyrene solutions used to grow thin films and DBRs by spin coating.

ZnO nanoparticles were synthetized from zinc acetate dihydrate and potassium hydroxide. In a typical process, 0.07 mol of zinc acetate are dissolved in methanol and heated at 63 °C under sonication. Then, 0.14 mol of potassium hydroxide are dissolved in the same solvent and slowly added to the first solution. After 3 hours of reaction, the particles are purified by five cycles of decantation and washing with methanol, and finally dried.

ZnO formation is attributed to the acetate hydrolyzation initiated by the alcoholic solvent (Figure 2.1, reactions 1 and 2) and a further esterification between the hydrolyzed acetate molecules (reaction 3). The esterification produces ZnO and water by condensation.[6, 7]

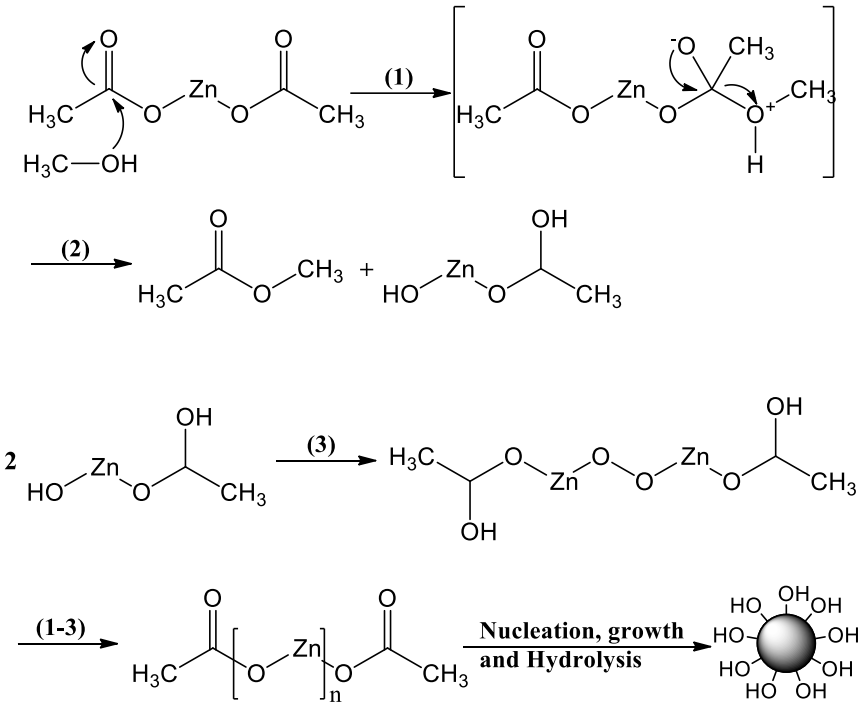

Figure 2.1: Mechanism of ZnO nanoparticles formation.

To avoid particles aggregation, responsible for light scattering in the non-polar polystyrene, methoxy (dimethyl) octadecylsilane (DMMOS) was grafted on their surface. To achieve the grafting, 10 g of nanoparticles were dispersed in 30 ml of methanol and sonicated. Then, 70 ml of dichloromethane containing 2.5 g of DMMOS were added to the dispersion. The overall dispersion was then sonicated until complete evaporation and desiccated in a vacuum at 40 °C for 2 h. The reaction between the surface and the adsorbed DMMOS was run at 135°C under nitrogen flux for 2 h.[8]

The graft reaction between the surface and the adsorbed DMMOS consists in the formation of a covalent bond between the only DMMOS functional group (-OCH_3) and the ZnO nanoparticles hydroxyl groups (Figure 2.2).

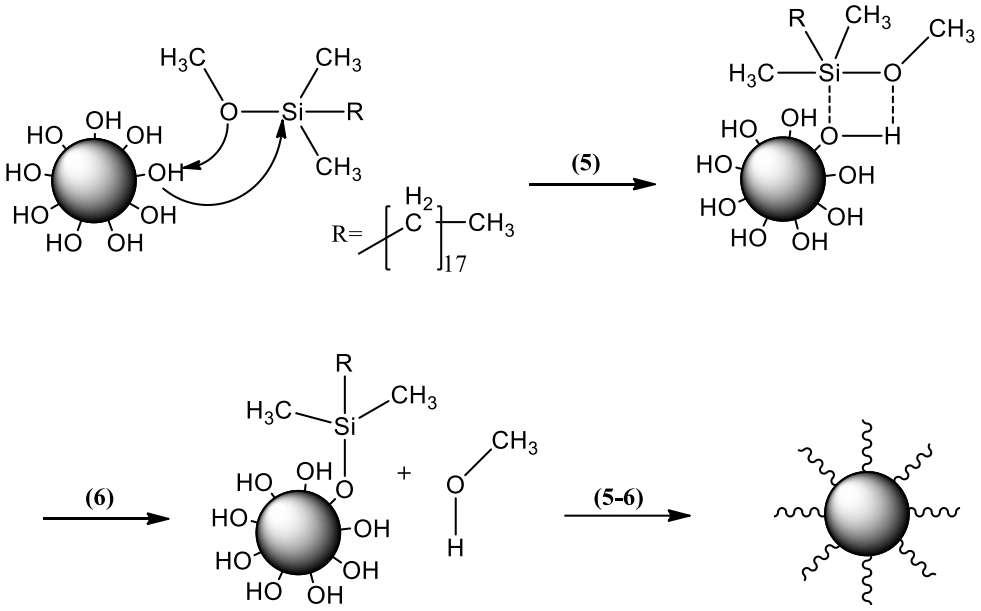

Figure 2.2: Mechanism of ZnO nanoparticles grafting.

To fabricate the nanocomposite thin films, the grafted ZnO nanoparticles were dispersed into toluene solutions of polystyrene (Sigma Aldrich, MW = 200000) and stirred for more than 36 h at room temperature. The thin films were grown by dynamic spin coating of colloidal solutions with polystyrene concentration ranging from 3 to 5 % (w/v) and nanoparticle load of 1% (v/v_{PS}). These films were then alternated to layer of cellulose acetate (Sigma Aldrich, MW = 61 000) dissolved in diacetone alcohol. The polymer concentrations ranged from 3 to 5 % (w/v) and the rotation speed during the deposition was kept at about 100 rps.

2.2 FHPSs Optial Characterization

The optical characterization of all the DBRs was performed trough reflectance measurement with a home-made setup. For the analysis, we used a Y-fiber probe made of a bundle of 7 fibers, 6 of which connecting the light source to the sample and 1 for light collection, which connects the sample to the spectrometer (Figure 2.3). The fiber is coupled to an AvaSpec-2048 spectrometer (200−1150 nm, resolution 1.4 nm). The light source is a halogen-deuterium Micropak DH2000BAL. The setup allows measuring a wide spectral range (200 nm to 2600 nm) with resolution of 1.5 nm.

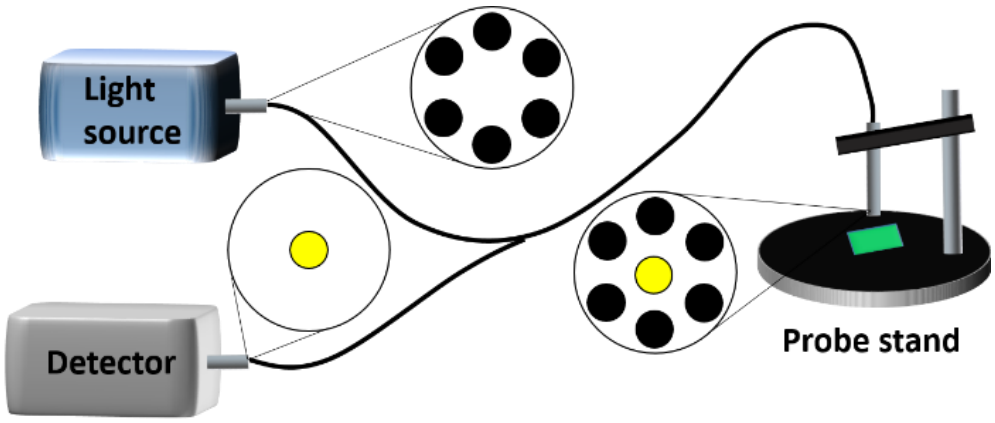

Figure 2.3: Schematic of the experimental setup used for normal incidence reflectance measurements.

2.3 FHPSs Optical Response to Vapors

The optical response of the FHPSs to vapor analytes was assessed with a home-made system similar to the one shown in Figure 2.3. In this case, the reflectance probe is substituted by an immersion probe endowed with a small open chamber containing a scattering surface (Figure 2.4).[4-7] The sample is positioned within this chamber at normal incidence with respect to the impinging light. The collected signal consists of the sum of the light reflected from the sample and part of the light scattered from the holder.

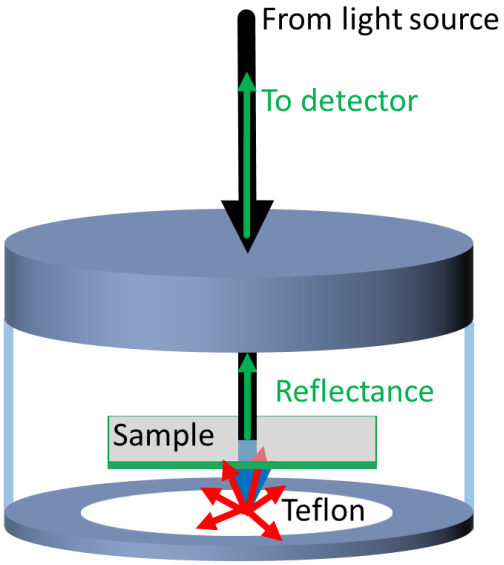

Figure 2.4: Schemes of an immersion probe used for sensing measurement.

The optical response to vapor analytes was measured immersing the probe containing the sample into a sealed tube at room temperature and humidity, typically 20 °C and 70% and 1 atm. The tube is loaded with 0.5 ml of liquid analyte to saturate the atmosphere. The analytes tested in this Thesis, their thermodynamic parameters together with the motivation that led to their choice are described in Chapters 3, 4, and 5.

2.4 DBRs and FHPSs Modeling

DBR thickness was estimated via modelling of their reflectance spectra using a home-made Matlab® software based on the Transfer Matrix Method (TMM) described in Appendix A.5. The software inputs are:

- A vector (L) containing the wavelength sampled with interval (IL).
- A vector containing the angles of incidence (T) sampled with interval (IT).
- The geometrical thickness of the substrate (d_s) low (d_l) and high (d_h) refractive media.
- Three vectors containing the complex refractive index dispersion of the two dielectric media (n_l, n_h) and of the substrate (n_s).
- The geometry of the system in terms of number and order of periods.

Given these inputs, the software calculates the global matrix for the given geometry and returns six matrices with size TxL containing the reflectance and transmittance spectra for P and S light polarization, as well as for unpolarized light.

2.5 Other Characterizations

Some of the FHPSs required specific characterizations or preparation methodologies, in the following we briefly describe the methods employed.

2.5.1 Thin Film Geometrical Thickness Variations

The thicknesses variation of PS and the CA single films during vapor exposure casted on glass substrates were measured by light interferometry using an interference microscope GBS smart WLI with a 20x interference objective.[8] The measurements were done placing the sample in a container loaded with the analyte and endowed with a small observation aperture. This set-up does not allow full saturation with the analytes but allows to gather qualitative information about the interacting layer in the FHPS.

2.5.2 Thin Film Morphology

The surface morphology of FHPSs before and after exposure to certain analytes was assessed to investigate possible irreversible effects of the exposure. The morphology of the FHPS was investigated by atomic force microscopy using a Nanosurf microscope on an area of 10 μm x 10 μm with a sampling rate of 512 points/line.

2.5.3 Composition of Commercial Polymer Films

Raman spectroscopy was employed to assess the composition of the commercial polymer films reported in Chapter 5. The Raman spectrum of the film was collected in the range 400-2000 cm^{-1} with a Rigaku Xantus^{TM}-1 using excitation at 1064 nm with power of 400 mW.

2.5.4 Surface Activation Treatments

Due to the low surface energy of HY, after the deposition of each HY layer a low power O_2-N_2 mixtures vacuum plasma treatment (15 W, 30 s) was performed to improve PVK adhesion by using a Gambetti Colibri system.[9] The surface wettability was then assessed for 24 h by water drop contact angle. The measurement were done with a Theta Lite optical tensiometer by Biolin Scientific[10] using the sessile drop technique.[11]

References

(1) Scotognella, F.; Varo, S.; Criante, L.; Gazzo, S.; Manfredi, G.; Knarr, R. J.; Comoretto, D., Spin-coated polymer and hybrid multilayers and microcavities. In *Organic and Hybrid Photonic Crystals*, Springer: Cham, CHZ 2015; pp 77-102.

(2) Lova, P.; Manfredi, G.; Boarino, L.; Comite, A.; Laus, M.; Patrini, M.; Marabelli, F.; Soci, C.; Comoretto, D., *ACS Photonics***, 2015**, 2, 537-543**.**

(3) Lova, P.; Manfredi, G.; Boarino, L.; Laus, M.; Urbinati, G.; Losco, T.; Marabelli, F.; Caratto, V.; Ferretti, M.; Castellano, M.; Soci, C.; Comoretto, D., *Phys. Status Solidi C***, 2015**, 12, 158-162**.**

(4) Lova, P.; Manfredi, G.; Bastianini, C.; Mennucci, C.; Buatier de Mongeot, F.; Servida, A.; Comoretto, D., *ACS Appl. Mater. Interfaces***, 2019**, 11, 16872-16880**.**

(5) Lova, P.; Megahd, H.; Comoretto, D., *ACS Applied Polymer Materials***, 2019.**

(6) Giusto, P.; Lova, P.; Manfredi, G.; Gazzo, S.; Srinivasan, B.; Radice, S. V.; Comoretto,

D., *ACS Omega*, **2018**, 3, 7517-7522.

(7) Lova, P., *Polymers*, **2018**, 10, 1161.

(8) Kim, S.-W.; Kim, G.-H., *Appl. Opt.*, **1999**, 38, 5968-5973.

(9) Radice, S. V.; Gavezoti, P.; Simeone, G.; Albano, M.; Congiu, S.; Canazza, G.; Comoretto, D. Photonic crystals. Filing date 20 March 2014, 2014.

(10) Rudakova, A. V.; Maevskaya, M. V.; Emeline, A. V.; Bahnemann, D. W., *Sci. Rep.*, **2016**, 6, 34285.

(11) Jokinen, V.; Suvanto, P.; Franssila, S., *Biomicrofluidics*, **2012**, 6, 016501-016501-10.

Chapter 3: FHPSs for Label-Free Selectivity and Determination of Diffusion Coefficients

This Chapter reports on commodity polymer multilayers as proof-of-principle systems to demonstrate that FHPSs sensitivity and selectivity can be explained in term of Flory-Huggins interaction parameters. It reports on the optical response of PS:CA multilayers to five short chain alcohols, the determination of their diffusion coefficient in the polymer matrix, and their recognition, also in binary mixtures. Eventually, sensitivity, lower detection limit and reversibility of these systems will also be reported.

This section is substantially published at:

Lova, P. et al. Flory-Huggins Photonic Sensors for the Optical Assessment of Molecular Diffusion Coefficients in Polymers, ACS Appl. Mater. Interfaces**, 2019**, 11, 16872-16880**.**

Chapter 1 summarizes previous findings in the field of polymer multilayered sensors for vapor analytes employng UV-Vis spectroscopy. In this regard, label-free selectivity was achieved using phase-transition polymers providing different analytes diffusion kinetics. Based on these findings, this Thesis proposes to use such kinetics to quantify the diffusion coefficient of the molecular species into the polymer multilayers. This Chapter aims to demonstrate the feasibility of the method proposed in Paragraph 1.4 using FHPSs made of commodity polymers. The possibility to relate the permeation kinetics of the molecular species to the simple FHPS optical response could indeed lead to a new powerful tool able to determine vapor diffusivity into polymer multilayers and to operate efficient vapor label-free qualitative analyses, also suitable *in-situ.* This could make colorimetric sensors interesting for safety devices, industrial, households, and offices pollution monitoring and in food industry.[1]

The FHPSs sensor object of this study are made of 31 alternated layers of PS and CA. The FHPS spectrum shows three maxima of reflection located at 845 nm, 430 nm and 300 nm corresponding to the first order PBG and its two higher order replicas (Figure 3.1, black line). The spectrum background displays a Fabry-Pérot pattern typical of DBR structures. All these spectral features were modelled in the range between 290 nm and 1150 nm using the TMM formalism reported in Chapter 2 and Appendix A.5[1-2] using the refractive index of PS and CA[3] as inputs and the layer thicknesses as fitting parameters. The red line of Figure 3.1 shows the calculated spectrum which, in full agreement with the experimental data, provides thicknesses of 160 nm for PS and 111.5 nm for CA for a total FHPS thickness of 4232 nm.

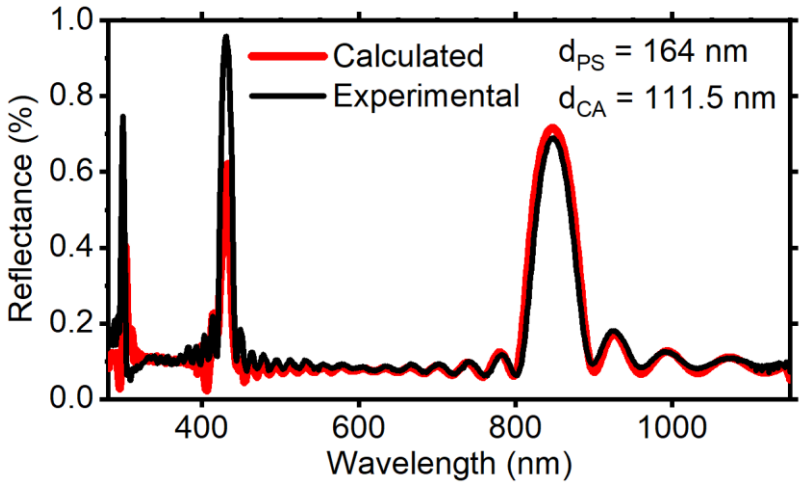

Figure 3.1: Experimental (black line) and calculated (red line) spectra of the PS:CA FHPS sensors.

The optical reponse of this system was registered for a chemical series of short chain alcohols with chemico-physical properties scaling with the number of carbons. The sensors were then divided into five portions, which were exposed to methanol (MeOH), Ethanol (EtOH), 1-propanol (1POH), *2*-propanol (2POH), and 1-butanol (BuOH). These analytes were chosen for two reasons. First, owing to similar molecular weight and comparable Van der Waals volumes, polarity, hydrogen bonding, and volatility, their discrimination is challanging. Second, the ability to disentangle these alcohols and to study polymer barrier properties to ther vapors is imprtant to prevent toxic effects. Indeed, while EtOH is used in food industry, MeOH, which is a byproduct of EtOH fermentation, generates toxic effects in both acute and cronic forms[4-6] Moreover, 1POH and 2POH share a similar structure, physical properties, and applications, but 2POH is less toxic than 1POH and finds applications in many antibacterial and personal care products.[6] Similarly, BuOH, which is interesting for biofulel,[7] shows a very low toxicity, but causes eye and skin irritation and is harmful if inhaled.[6]

3.1 FHPS Response to Alcohol Vapor Exposure

Figure 3.2 displays the FHPS optical response to MeOH (a, a'), EtOH (b, b'), 1POH (c, c'), 2POH (d, d') and BuOH (e, e') vapors. At a first look, the responses are rather complex and characterized by very different kinetics and spectral behaviors. However, these data allow to recognize the analytes. In details, when exposed to MeOH, the first two PBGs are initially located at 845 nm and 430 nm, respectively (Figure 3.2 a). These features are visible in red-tones, while the spectra background is represented in blue tones. The red-shift of the PBGs is initially very fast, and reaches ~80% of the final value within the first 10 min of exposure. Then, the dynamics slows down, and the system reaches the equilibrium in 90 min. Figure 3.2 a' shows the maximum of intensities for the first order PBG versus the square root of the exposure time after normalization by the shift observed at the steady-state (~90 min, $\Delta\lambda_{1\infty}$ = 100 nm).

In EtOH, within 600 min of exposure the two spectral features assigned to the PBGs red-shift of $\Delta\lambda_{\infty 1\,EtOH} = 153\,nm$, $\Delta\lambda_{\infty 2\,EtOH}$ = 64 nm. Again, at the begin of the exposure the shift is faster than at longer times. The analyte uptake increases until t =325 min ($\sqrt{t}$=18 min$^{1/2}$). Then, the band position oscillates within less than one twentieth of $\Delta\lambda_t / \Delta\lambda_\infty$ (Figure 3.2 b'). This behavior is assigned to the relaxation and rearrangement of the polymer chains from stresses associated with the swelling.[8] This phenomenon, was already observed for CA,[9] and it is known

to slow down the permeation process. Indeed, the relaxation corresponds to a chain rearrangement resulting in a slower uptake rate owing to cooperative movements of polymer segments necessary to make larger volume changes. Under this condition the permeation mechanism leads to additional uptake of molecules with a first order kinetics and induces a non-Fickian deviation of the sorption curve at the long time scale.[10] A similar behavior is visible for all the other analytes but for MeOH.

Concerning the exposure to 1POH, the kinetics is slower than in the previous cases, and PBG shifts of $\Delta\lambda_{\infty 1\,1POH}$ = 180 nm and $\Delta\lambda_{\infty 2\,1POH}$ = 85 nm are reached in ~ 1500 min (Figure 3.2 c). In this case, the shift of the PBG appears almost monotone till t=600 min ($\sqrt{t}$ >25 min$^{1/2}$). Then, it shifts to the blue (decrease of $\Delta\lambda_t\,/\Delta\lambda_\infty$) and suddenly shifts again to the red part of the spectrum several times (increase of $\Delta\lambda_t\,/\Delta\lambda_\infty$, Figure 3.2 c'). This behavior is assigned to slow intercalation kinetics, which swells the FHPS layers one by one from the top to the bottom of the sample.[1-2]

In the case of exposure to 2POH, the PBGs reach a red-shift of $\Delta\lambda_{\infty 1\,2POH}$ = 182 nm and $\Delta\lambda_{\infty 2\,2POH}$ = 90 nm respectively within 600 min. The entire shift is characterized by a discontinuous behavior. Indeed, the first order PBG initially moves of ~50 nm to the long wavelength side of the spectrum, then suddenly shifts back to the blue in ~100 min (Figure 3.2 d and d') and then move again to the red monotonically for 200 mins. At this time, the peak suddenly shifts of ~ 70 nm from 900 nm to 970 nm. Here the stationary condition is almost reached. Indeed, the sorption curve of Figure 3.2 d' approaches the plateau. At longer time, we notice other discontinuities in the band position assigned to self-stress relaxation.

The exposure to BuOH displays a similar optical behavior with respect to 2POH. The first order PBGs undergoes the largest shift at the equilibrium conditions, which corresponds to $\Delta\lambda_{\infty 1\,1BuOH}$ = 220 nm and $\Delta\lambda_{\infty 2\,1BuOH}$ = 100 nm. In Figure 3.2 e and e', the position of the PBG moves to the red part of the spectrum discontinuously. After an initial shift from 845 nm to 861 nm, at 50 min of exposure the peak suddenly shifts to 820 nm. Then, it linearly moves to 940 nm at ~300 mins. At this time, the PBG starts oscillating within a 60 nm interval, corresponding to a $\Delta\lambda_t\,/\Delta\lambda_\infty$ ~ 0.25. Last, we notice again a discontinuity of $\Delta\lambda_t\,/\Delta\lambda_\infty$ at 50 min ($\sqrt{t}$ = 7 min$^{1/2}$) and relaxation of the polymer chains after 890 min ($\sqrt{t}$ = 17 min$^{1/2}$).

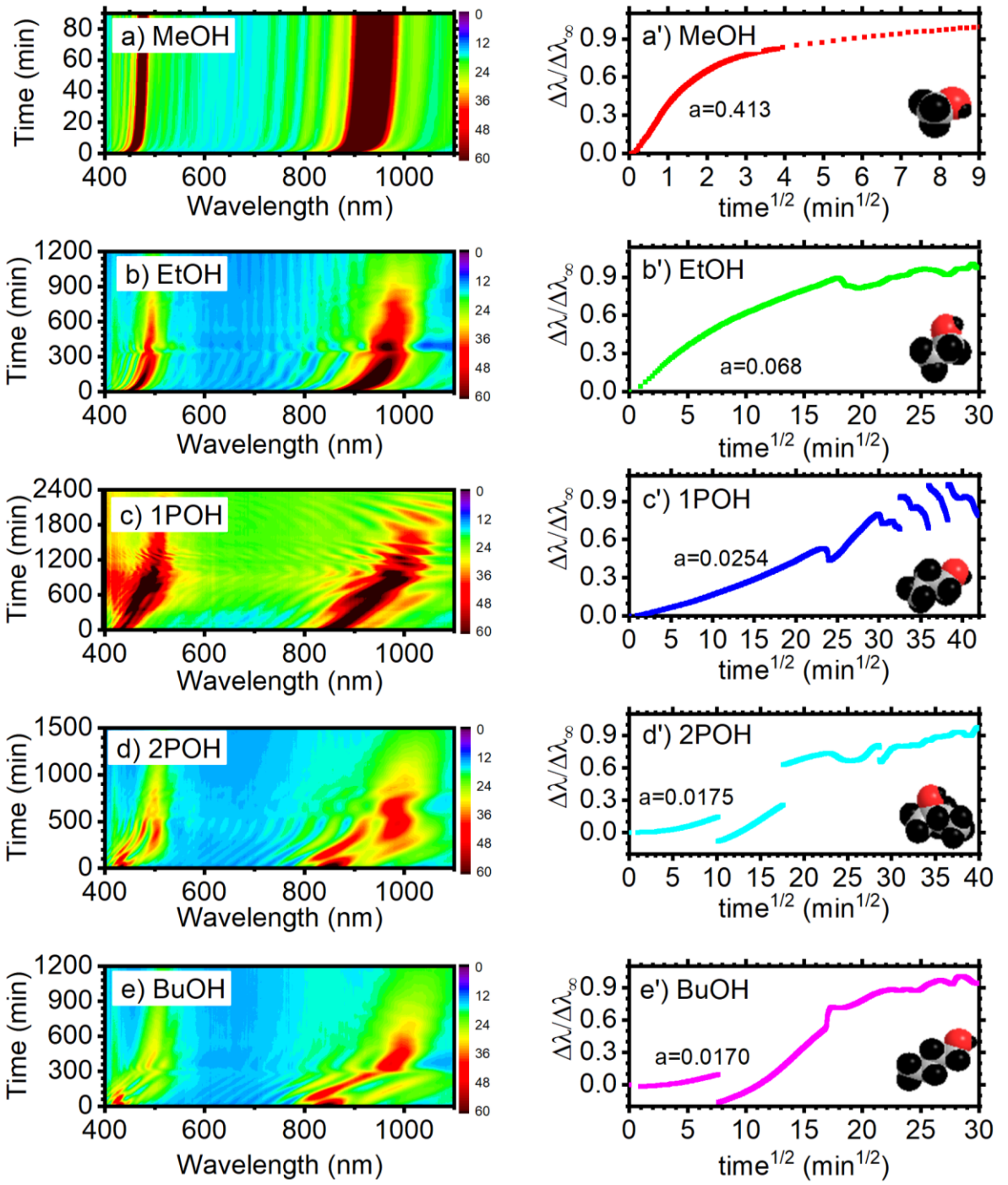

Figure 3.2: Optical response of the FHPS for exposure to (a-a') MeOH, (b-b') EtOH, (c-c') 1POH, and (d-d') 2POH and (e-e') BuOH. (a-e) entire spectral response. (a'-e'), Optical sorption curves retrieved from the spectral position of the first order PBG.

In summary, the curves show two behaviors; the first characterizes the sorption of MeOH and EtOH and consists in a linear increase of the analyte intake followed by the steady-state regime. The second, observed for 1POH, 2POH and BuOH, shows several discontinuities in the PBG

position that occurs both at the steady and at the non-steady state regimes. In agreement with previous findings,[1-2] in the case of alcohols with larger steric hindrance (C3-C4), the intercalation is slower, and the layers swell gradually from the top one in contact with air to the bottom one in contact with the substrates.[1-2] The presence of swollen and un-swollen layers breaks the DBR order destroying the PBG and creating those discontinuities. Conversely, discontinuities at longer exposure time, can be assigned to relaxation and rearrangement of the polymer chains from stresses associated to the large swelling induced by the intercalation, as already reported in literature.[8]

3.2 Detemination of Diffusion Coefficients

According to Equation 1.2, the optical sorption curves can be used to assess the effective diffusion coefficient of the analytes in the whole polymer composite ($\mathcal{D}_{eff}$) from their angular coefficient and the initial thickness of the FHPS.[1, 3, 11] The slope of the optical sorption curves has then been retrieved within their interval of linearity for values of $\Delta\lambda_t / \Delta\lambda_\infty < 0.2$ (Figure 3.2), while the value of $\Delta\lambda_\infty$ was evaluated as the average $\Delta\lambda$ in the plateau region of the curves. The values of $\mathcal{D}_{eff}$ are summarized in Table 3.1 and Figure 3.3 a where the data are also compared with results available in literature for MeOH and EtOH.[9, 12]

Table 3.1: Steric and chemico-physical parameters of the species and retrieved $\mathcal{D}_{eff}$.

	v (Å^3)[13]	δ (MPa$^{1/2}$) [14-17]	χ^H_{eff}	$\Delta\lambda_\infty$ (nm)	$\mathcal{D}_{eff}$ (cm^2 min^{-1})	LOD (mg/l)	Sensitivity (min-max)
MeOH	67.6	29.6	1.22	100	2.5*10^{-8}	29	19.5 – 0.8
EtOH	97.1	26.1	0.81	141	7.9*10^{-10}	12	15.6 – 0.9
1POH	124.9	24.4	0.64	180	3.8*10^{-11}	12	6.1 – 2.9
2POH	127.5	23.6	0.56	182	2.2*10^{-11}	6	13.4 – 3.5
BuOH	151.9	23.3	0.65	220	4.2*10^{-11}	64	6.3 – 1.0
PS	-	18.7	-	-	-		
CA	-	27.2	-	-	-		

v=Van der Waals volume, δ=Hildebrand parameter, χ^H_{eff}=effective Flory-Huggins parameter, $\Delta\lambda_\infty$=PBG shift at the equilibrium, $\mathcal{D}_{eff}$ =effective diffusivity within the DBR.

The diffusivity of MeOH in CA has been reported as 8-9 x 10^{-8} cm^{2}s^{-1} while for PS it is 1.4 x 10^{-8} cm^{2}s^{-1} (at 55°C),[25,37] in full agreement with the effective values retrieved for our composite

PS-CA DBR. For EtOH, the literature proposes 1-7 x 10^{-10} cm^2s^{-1} for CA and 9 x 10^{-10} cm^2s^{-1} (at 55°C) for PS,[9, 12] again in agreement with our data. Concerning the other alcohols, 1POH shows diffusion coefficient of 3.8 x 10^{-11} cm^2s^{-1}, for 2POH we retrieved 2.2*10^{-11} cm^2s^{-1}, while for BuOH 4.2*$10^{-11}$$cm^2s^{-1}$.

Because, the behavior of the sorption curves, and in turn $\mathcal{D}_{eff}$, can be affected by the analyte steric hindrance and by its chemico-physical affinity with the polymers. Figure 3.3 a compares the values of $\mathcal{D}_{eff}$ with the effective FHPS-analytes Flory-Huggins parameters (χ^H_{eff}, see Equation 1.2) calculated form the volume fraction of PS and CA within the DBR and neglecting the entropic contribution.[13] The panel b of the same Figure compares instead the FHPS PBG shift at the equilibrium, with the Van Der Waals volume of the analytes. Interestingly, the latter are strongly correlated to $\Delta\lambda_\infty$, and then to the polymer swelling. Conversely, there is a strong correlation between $\mathcal{D}_{eff}$ and χ^H_{eff}, and in turn with the solubility parameters between the polymers and the analytes (Figure 3.3 a and c).[16]

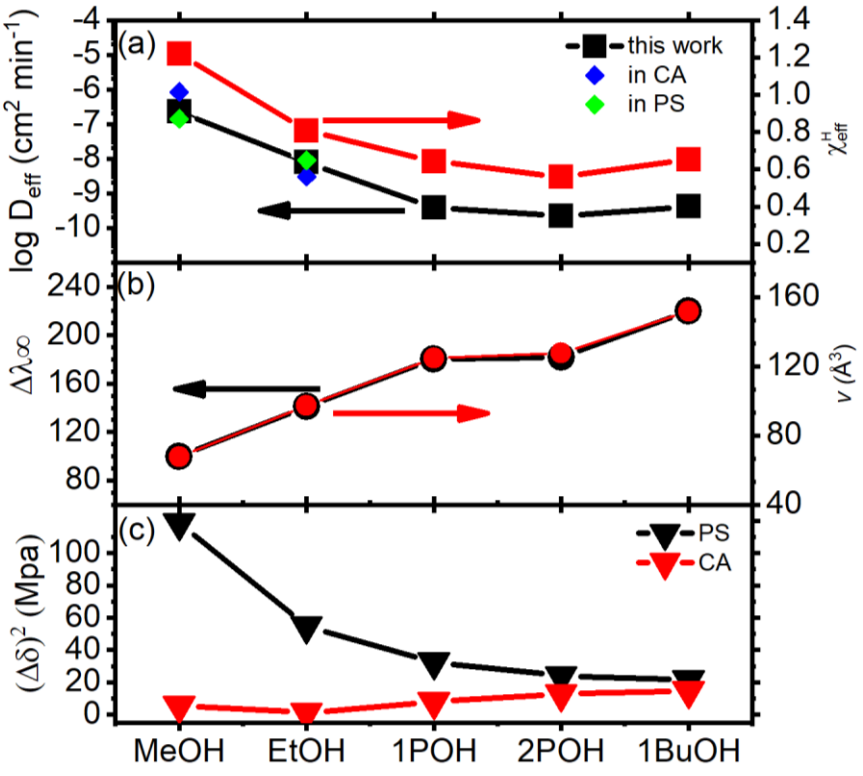

Figure 3.3 (a) Comparison between the retrieved value of $\mathcal{D}_{eff}$ for the five alcohols with literature data for CA and PS,[9, 12] and effective Flory-Huggins parameter (χ^H_{eff}). (b) Comparison of the FHPS $\Delta\lambda_\infty$ for five alcohols and the alcohol Van der Waals volumes. (c) Solubility parameters for the five alcohols with PS and CA.

Figure 3.3 c shows that, within the alcohols, the solubility of CA is larger than the solubility of PS and it is roughly constant. Conversely, for PS $\Delta\delta^2$ decreases with the molecular weight of the alcohols, affecting also $\chi_{\text{eff}}^{\text{H}}$. These data prove that the decrease of $\mathcal{D}_{eff}$ with the increase of the analyte molecular weight (panel a) is not linked by their solubility in the CA layers but in PS, which act as reservoir slowing down the analyte diffusion. Then, CA plays as the active medium undergoing swelling, while PS rules the diffusion kinetics. This information provide a general rule for the design of FHPSs, which requires a polymer with large solubility in the analyte to swell and provide the sensor with sensitivity, and a second polymer with lower solubility that act as barrier layer ruling the diffusion kinetics of the analytes and providing the sensors with selectivity. Then, knowing the Flory-Huggins and Hildebrand parameters for the polymer-analyte couples, it is potentially possible to design a selective sensor for any class of chemical compounds without using any chemical label.

This interpretation is also confirmed by the measurements of thickness variation measured by interference microscopy upon MeOH exposure of single PS and CA films (Figure 3.4).

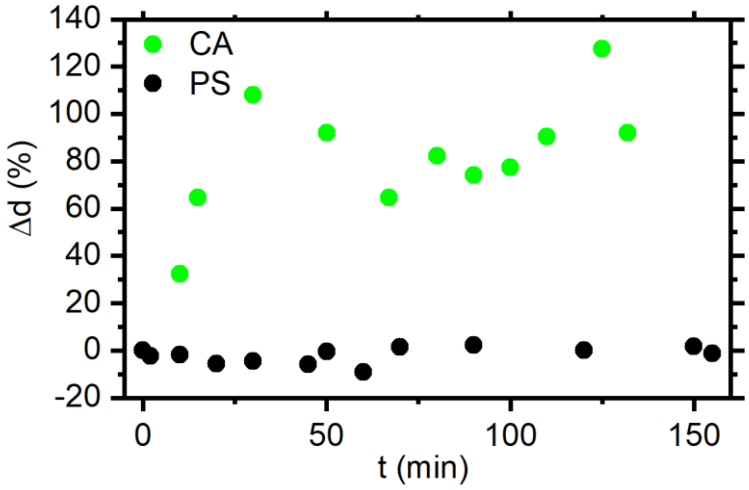

Figure 3.4: Measured PS and CA thicknesses during MEOH exposure by interference microscopy.

Figure 3.4 reports the polymer swelling as the percent variation with respect to the initial thickness value and shows that when CA is exposed to MeOH (green dots), the layer doubles its thickness within the first 25 minutes of exposure. Conversely, when PS is exposed to MeOH, thickness varies within ±5% with respect to the initial value, that is the instrumental sensitivity. These data confirm that CA is the only polymer interacting with MeOH. Notice that the values obtained for these single layers are not comparable with those of the same polymers within the

FHPS, where layer confinement constrains the swelling. Then, these measurements represent the upper limit for the swelling values.

3.3 Label-Free Selectivity

This simple and powerful optical method for the determination of $\mathcal{D}_{eff}$ also applies to the discrimination of the analytes. Figure 3.2 and Figure 3.3 show that even molecules with very similar structure and properties, such as 1POH and 2POH, provide a very different optical sorption kinetics and then different values of $\mathcal{D}_{eff}$. The optical sorption curves the dynamic of the overall FHPSs responses are indeed characteristic fingerprints of the analytes.[1-2] Moreover, the large spectral shifts make possible to discriminate the analytes also at short times. As an example, Figure 3.5 shows the spectra of the FHPS collected before and after 50 min of exposure to the five alcohols. While the sample initially shows two PBGs at ~845 nm and 430 nm, when exposed to MeOH, the PBGs width increases, and their spectral position shift to 931 nm and 474 nm, respectively. For EtOH the shift is smaller and the PBGs reaches 919 nm and 465 nm. 1POH instead provides a reduction of the peak width which, after 10 min of exposures moves to 861 nm and 436 nm. Concerning BuOH, the alcohols with higher molecular weight, its intercalation induces disorder and inhomogeneous broadening of the PBGs, which reaches maxima of intensities at 860 nm and 425 nm after the exposure. The dynamics of these spectral responses are shown in Figure 3.5 b and d for the five alcohols as contour plots.

The simple colorimetric analysis and the assessment of the entire diffusion kinetics represent an effective method for the discrimination of the analytes. On the other hand, analyzing the entire curves is rather complex, time consuming, and does not allow to easily distinguish mixtures. To achieve this goal and simplify data interpretation, one must consider that the dynamical optical responses are a typical playground for multivariate analyses, and then a principal component analysis (PCA) can be applied to disentangle pure analytes and their mixtures. Figure 3.5 g shows that the response can be described using only two variables (principal components PC1 and PC2) instead of the entire dynamics. We can indeed easily distinguish the five alcohols (squares) and binary mixtures of MeOH and BuOH. Such result represents a promising approach for the identification of complex mixtures in real systems.

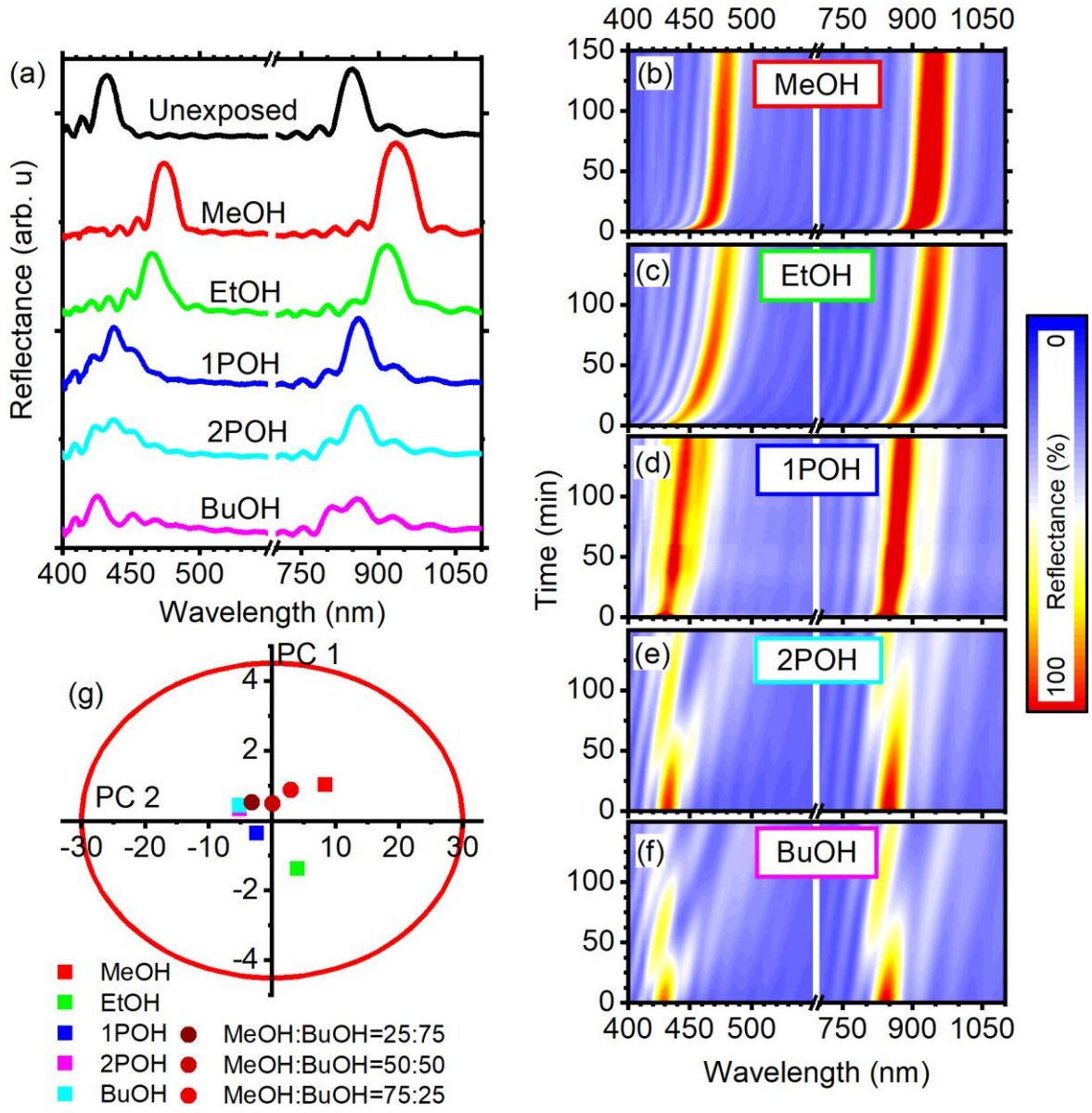

Figure 3.5: (a) Reflectance spectra before (black line) and after 50 min of exposure to the five analytes. (b-f) Contour-plots of the dynamic FHPSs response. (g) Power component analysis of the FHPS response for pure analytes and for MeOH:BuOH binary mixtures.

3.4 Response Time, Sensitivity and Lower Detection Limit

To evaluate the quantitative figures of merit of the FHPS, we exposed it to different concentrations of pure vapor analytes. The data displayed in Figure 3.6 a were retrieved for a FHPS made of 5.5 bilayers with PBG tuned at 450 nm, where the thinner layers and the smaller number of films allows responses almost 20 times faster than those seen so far. The plot reports

the response as the FHPS PBG shift obtained after only 5 min of exposure. The data were collected in concentration ranging from the analyte vapor pressure to the limit of detection (LOD) of the FHPS, that is the concentration inducing spectral shift as large as the spectrometer resolution (1.5 nm) within 5 min. Intuitively, increasing the response time, it is possible to further decrease the LOD. The LOD ranges from a minimum of 6 mg/l for BuOH to a maximum of 65 mg/l for 2 POH. Table 3.1 helps to evince that for linear alcohols the longer the carbon chains, the smaller is the LOD. For non-linear 2POH instead, the slow response induced by the steric hindrance of the molecules produces larger LOD.

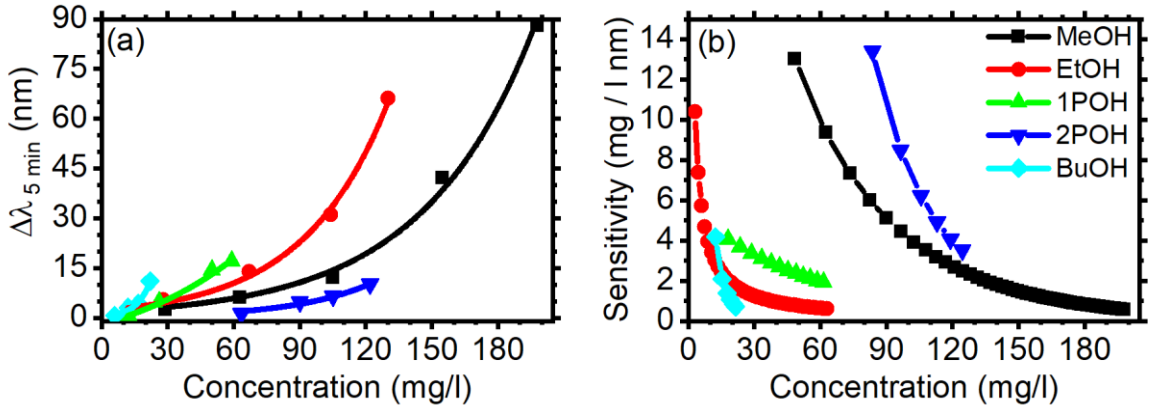

Figure 3.6: (a) PBG spectral shift collected after 5 minutes of exposure to different concentration of the five alcohols. The concentration ranges from the analyte vapor tension to the LOD of the sensor. (b) FHPS sensitivity at the different concentrations.

To evaluate the sensitivity of the devices we fitted the response of Figure 3.6 a with a first order kinetics and calculated the minimum concentration variation detectable by our optical system, which corresponds to a PBG optical shift of 1.5 nm. Such data are reported in Figure 3.6 b and show that due to the exponential dependence of the PBG shift with increasing concentration, the sensitivity of the system varies for different concentration intervals in the range 0.8-16 mg/l from the largest concentration to the smallest concentration of MeOH. The values for the other alcohols are within this range. The sensitivity is in full agreement with data previously reported in literature for other polymer photonic crystal sensors.[1, 18]

3.5 Reversibility

Last, concerning the reversibility of the FHPSs, Figure 3.7 shows the spectra collected during five cycles of exposure (panels a-e) and desorption (panels a'-e') to MeOH vapors for a FHPS with PBG tuned at about 460 nm.

The spectral behavior of the FHPS during the first exposure cycle (Figure 3.7 a) is consistent with the one reported for the sample with PBG tuned in the near infrared part of the spectrum reported in Figure 3.2. On the other hand, the kinetics of the first is 18 times faster than the latter owing to the thinner polymer layers. In this sample the equilibrium is indeed reached within 5 minutes of exposure. This data demonstrates that modifying the thickness of the layers, and in turn the PBG spectral position, it is possible to tune the response time, and consequently the limit of detection and the sensitivity of the FHPS.

The spectra collected during the first MeOH desorption (Figure 3.7 a') display that the PBG position return from the equilibrium position reached in 300 s of exposure to its initial position in about 1 minute, indicating desorption and deswelling of the polymer layers. The sample was then exposed and desorbed other four times without performing any treatment between the cycles. The sample shows similar swelling (a-e) and de-swelling (a'-e') behavior, but the spectral position of the PBG at the equilibrium (at 300 s in panels a-e) is different in any cycle, testifying a lack of full reversibility. The partial reversibility can be explained analyzing the atomic force microscope micrographs collected for the sample before (Figure 3.7 f) and after (Figure 3.7 f') the 5 cycles of exposure and desorption. While the surface of the sample before the exposure appears smooth (roughness about 1.9 nm) with only few irregularities embedded in the polymer during the deposition, after the 5 cycles the surface appears much rougher (roughness 13 nm) with the presence of globules, probably due to a variation of the polymer morphology occurred during the several swelling processes.

Even though we cannot exclude that reversibility could be achieved through thermal treatment, such characteristics makes these FHPSs interesting as disposable sensors, similarly to the colorimetric quantitative test tubes already available on the market (See Paragraph 1.1.1), but with the capability to perform qualitative analytìses.[19]

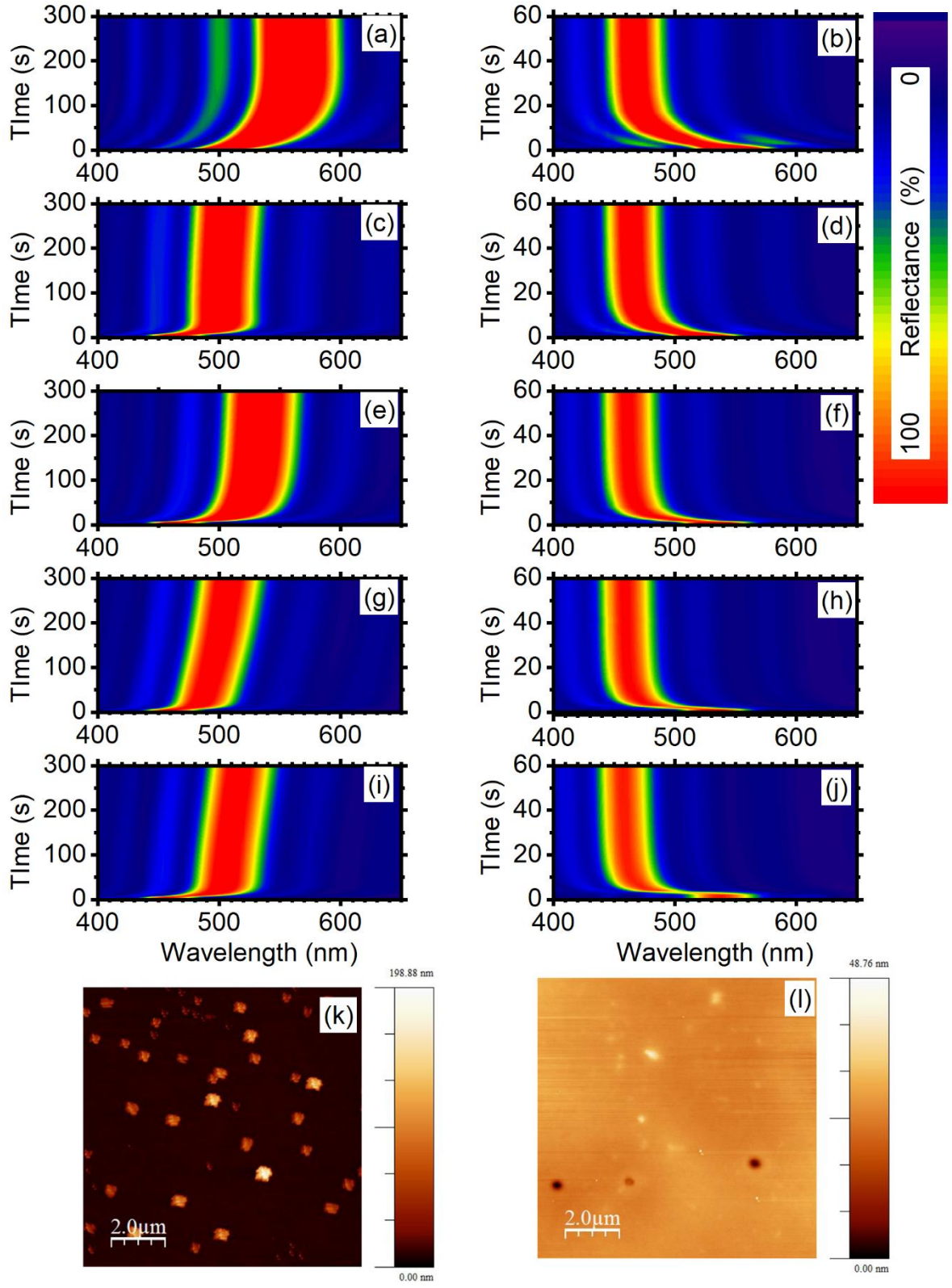

Figure 3.7: Contour plot of the spectra collected during 5 cycles of exposure (a-e) and desorption (a'-e') of the same sample to methanol vapor with concentration 238 mg/l. Atomic force microscopy of the sample surface before (f) and after the 5 cycles of exposure and desorption.

The optical transductors are few millimeters in size and fully processed from solution using commodity polymers. Furthermore they can also be grown over square meters by coextrusion,[20-23] a technique widely used in the industrial production of packaging,[19, 24] making realistic the production of FHP sensors on large scale and at low costs. Exploiting the fundamental thermodynamic of polymer-analyte mixtures allows then to engineer FHPSs affinity with degradation by-products or harmful chemical species. We envision their integration in smart packaging systems to monitor *in-situ* internal and external environments and assess diffusion of small molecules. This will also be possible thanks to small and compact detection systems already available on the market.[25-26]

3.6 Outcomes

This Chapter demonstrates a versatile tool for the optical determination of the effective diffusion coefficients of vapors within simple multilayered polymer DBRs in excellent agreement with the values reported in literature. The analysis of the FHPS response kinetics can also be related to the chemico-physical interaction between the analyte and the polymers allowing simple and label-free molecular recognition by sensors engineered *ad hoc*. The optical behavior of a DBR made by commodity polymers, which are easy to integrate in smart packaging devices, has been fully investigated during the exposure to five short chain alcohols. The study of the dynamic optical responses of the FHPS allows to retrieve sorption curves characteristic of the analytes that provides their diffusion coefficients and permits their discrimination. Sensitivity, lower detection limit, response time and reversibility were also investigated. This proof of concept device is promising for the development of sensors to be used on-site for the assessment of environmental pollution and for smart packaging.

References

(1) Lova, P.; Bastianini, C.; Giusto, P.; Patrini, M.; Rizzo, P.; Guerra, G.; Iodice, M.; Soci, C.; Comoretto, D., *ACS Appl. Mater. Interfaces*, **2016**, 8, 31941–31950.

(2) Lova, P.; Manfredi, G.; Boarino, L.; Comite, A.; Laus, M.; Patrini, M.; Marabelli, F.; Soci, C.; Comoretto, D., *ACS Photonics*, **2015**, 2, 537-543.

(3) Frezza, L.; Patrini, M.; Liscidini, M.; Comoretto, D., *J. Phys. Chem. C*, **2011**, 115, 19939 - 19946.

(4) Martin-Amat, G.; McMartin, K. E.; Hayreh, S. S.; Hayreh, M. S.; Tephly, T. R., *Toxicol.*

Appl. Pharmacol., **1978**, 45, 201-208.

(5) McMartin, K. E.; Ambre, J. J.; Tephly, T. R., *Am. J. Med.*, **1980**, 68, 414-418.

(6) Patocka, J.; Kuca, K., *Mil. Med. Sci. Lett.*, **2012**, 81, 142-163.

(7) Ezeji, T. C.; Qureshi, N.; Blaschek, H. P., *Curr. Opin. Biotechnol.*, **2007**, 18, 220-227.

(8) Soney, G. C.; Sabu, T., *Prog. Polym. Sci.*, **2001**, 26, 985-1017.

(9) Perrin, L.; Nguyen, Q. T.; Sacco, D.; Lochon, P., *Polym. Int.*, **1997**, 42, 9-16.

(10) Berens, A. R.; Hopfenberg, H. B., *Polymer* **1978**, 19, 489-496.

(11) Manfredi, G.; Mayrhofer, C.; Kothleitner, G.; Schennach, R.; Comoretto, D., *Cellulose*, **2016**, 23, 2853-2862.

(12) Bernardo, G., *J. Appl. Polym. Sci.*, **2013**, 127, 1803-1811.

(13) Hansen, C. M., *Hansen Solubility Parameters: A User's Handbook*. 2nd ed.; CRC press: Boca Raton, USA, 2002.

(14) Bernardo, G.; Vesely, D., *Eur. Polym. J.*, **2007**, 43, 938-948.

(15) Daubert, T. E.; Danner, R. P.; Sibul, H. M.; Stebbins, C., *Physical and Thermodynamical Properties of Pure Chemicals.* Taylor and Francis: New York, 1988.

(16) Cowie, J. M. G., *Polymers: Chemistry and Physics of Modern Materials.* Chapman&Hall: London, 1991.

(17) Brandrup, J.; Immergut, E. H.; Grulke, E. A.; Abe, A.; Bloch, D. R., *Polymer Handbook (4th Edition)* John Wiley & Sons New York, 2005.

(18) Lova, P.; Manfredi, G.; Comoretto, D., *Adv. Opt. Mater.*, **2018**, 6, 1800730-26.

(19) COLORIMETRIC TEST TUBES - https://www.shopcross.com/draeger-tubes. (accessed 11/12/2019).

(20) 3M DICHROIC - https://www.3m.com/3M/en_US/company-us/all-3m-products/~/3M-Dichroic-Films-for-Architectural-Laminated-Glass/?N=5002385+3291680356&rt=rud. (accessed 11/12/2019).

(21) TORAY - http://www.toray.com/. (accessed 11/12/2019).

(22) Chamaleonlab - http://chameleonlab.nl/. (accessed 11/12/2019).

(23) Kazmierczak, T.; Song, H.; Hiltner, A.; Baer, E., *Macromol. Rapid Commun.*, **2007**, 28, 2210-2216.

(24) Jing, L.; Jianhua, X.; Shuang, X., *Energy Procedia*, **2011**, 12, 625-631.

(25) FrinGOe - https://fringoe.com/. (accessed 11/12/2019).

(26) Das, A. J.; Wahi, A.; Kothari, I.; Raskar, R., *Scientific Reports*, **2016**, 6, 32504.

Chapter 4: Design of FHPSs for Different Analyte Families

The previous Chapter defines a general method for the design of FHPSs able to detect and disentangle any class of vapor analyte compound. In the follow, we test this method for the detection of hydrocarbons and perfluorinated compounds.

This section is substantially published at:

Lova, P., Selective Polymer Distributed Bragg Reflector Vapor Sensors, *Polymers***, 2018**, 10, 1161**.**

Giusto, P. et al., Colorimetric Detection of Perfluorinated Compounds by All-Polymer Photonic Transducers *ACS Omega***, 2018**, 3, 7517-7522**.**

In the Previous Chapter, we demonstrate that FHPSs need two active media. The first is a polymer soluble in the analyte that provide strong swelling and therefore the optical response; the second is a polymer with low solubility in the analyte, that plays as a barrier layers, thus ruling the diffusion kinetics of the analyte within the FHPS. Following this receipt, it is then potentially possible to design FHPSs for any class of chemical species. As a proof of principle, this chapter reports on two detection systems for the detection of aryl and halogenated hydrocarbons and for the detection of perfluorinated compounds. As discussed in the next Paragraphs, these two class of materials were chosen owing to their potential toxicity and the necessity to develop extensive detection methods for the assessment of air quality.

4.1 Hydrocarbon Analytes

Among vapor pollutants, aryl and halogenated hydrocarbons pose serious environmental harm and concern to the human body. Table 4.1 classifies some of them on the base of their effect on the body. The list shows that, among others, commonly used solvents such as tetrachloroethylene, frequently used for dry cleaning, is a suspected carcinogenic agent.[1-2]

Table 4.1: List of common hydrocarbon based on their effect on human body.

Effect	Compound
Toxic to organ systems[1]	Toluene, xylenes, chlorobenzene, dichlorobenzenes, styrene, chloroform, bromoform, tetrachloroethane, dichloroethane, dichloroethane, dichloropropene, bromomethane.
Mutagen and developmental[1]	Xylenes, vinyl chloride, ethylbenzene, chloroform, chloroethane, dichlorobenzenes, phalates.
Neurological[1]	Fuel and mineral oil, toluene, benzene, xylenes, trichloroethane, carbon tetrachloride, chloroform, ethylbenzene, mercaptans, naphtalenes.
Potential carcinogen[2]	Polycyclic aromatic hydrocarbons, naphtalenes, halogenated hydrocarbons (e. g. chloroform, carbon tetrachloride, dichlorobenzenes, trichloroethylene, hexachloroethane polyhalogenated biphenyles)
Carcinogen[2]	Benzene, vinyl chloride, benzidine, bis(chloromethyl) ether.

These compounds are released by industrial processes such as oil refinery, power plants, and chemical manufactures, and in urban areas by vehicles, painting works, dry cleaning, refrigerators and wood burning.[3-5] Their high toxicity and wide spreading make their identification and extensive monitoring in living and working environments critical to preserve people's health and to identify proper treatments in case of poisoning.

For the detection of these compounds we designed a FHPSs similar to the one reported in Chapter 3 made of CA as low index and barrier medium and a PS nanocomposite doped with ZnO nanoparticles (ZnONP@PS, n=1.59 [6]) as high refractive index and active sensing medium to detect and recognize toluene (TOL), Benzene (BEN), ortho dichlorobenzene (o-DCB), and carbon tetrachloride (CTC) (Figure 4.4). Indeed, CA Flory-Huggins parameter ranges from 1.2 to 2.1 for the four analytes (Table 4.2) making it a an appropriate barrier medium.[6] Conversely, PS permeability is usually low, but its Flory-Huggins parameter is very small for the chemical species under consideration, making it well suitable as sensitive medium (Table 4.2). To increase PS permeability, we doped the dense matrix with silanized nanoparticles to increase of the polymer free-volume, allowing sensitivity below the part per million (ppm) and lower detection limit of ~20 ppm to toluene vapors.[6] This allows faster response than those reported for bare polymer FHPSs,[6-8] but maintaining the high processability typical of amorphous polymers. The optical nanocomposite (NC) was prepared by spin-coating of ZnO nanoparticles dispersion in polystyrene-toluene solutions. The nanoparticles XRD pattern shows peaks at angles 2θ: 31.7, 34.3, 36.3, 47.5, 56.6, 62.9 and 68.1, corresponding to Wurtzite crystallographic orientations (100), (002), (101), (102), (110), (103) and (112). The pattern indicates 13 nm crystallites as derived from Debye-Scherrer data. This data is confirmed by SEM analysis showing an average size of 14 nm.

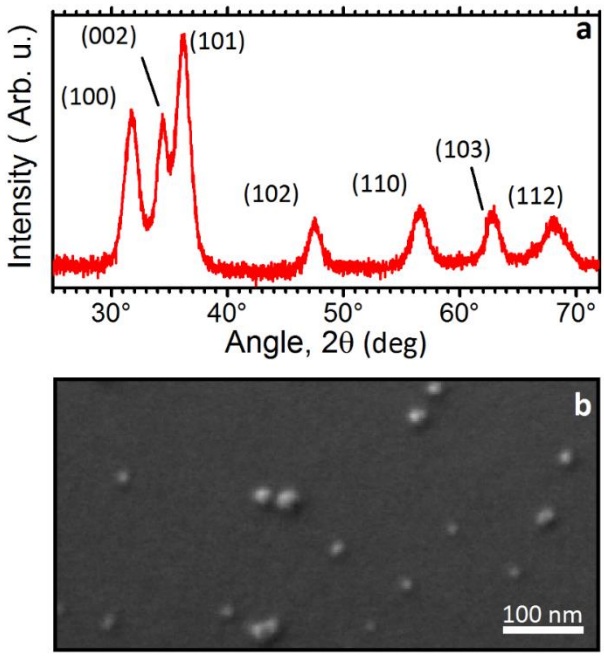

Figure 4.1: a) ZnO nanoparticles powder XRD pattern and b) SEM micrograph.

To achieve good dispersion within the polystyrene matrix, the particles were grafted with a monolayer of DMMOS (see Paragraph 2.1.1). Figure 4.2 a and b compare the SEM images for thin polystyrene film loaded with 2.5% V/V_{PS} of bare and grafted nanoparticles While several aggregates of few microns in size are visible in the film prepared with bare nanoparticles, the surface of the film with the grafted particles is smoother. Grafting allows the reduction of the aggregate number and dimension from ~12000 mm^{-2} with average diameter of 1.1 μm to ~2300 mm^{-2} with average diameter of 0.4 μm. Negligible light scattering is thus expected from the grafted material.

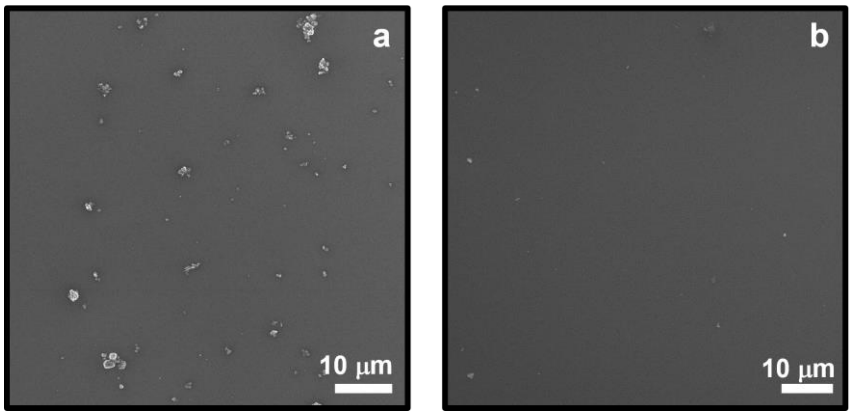

Figure 4.2: SEM micrographs of nanocomposite thin films loaded with: a) bare ZnO nanoparticles and b) particles grafted with DMMOS.

The increase of permeability induced by the load was evaluated by permeation of helium on free-standing nanocomposite and bare polystyrene thin films. Figure 4.3 shows that the permeability of polystyrene is very low, and does not depend on the applied pressure. This behavior is due to the non-porous nature of the polystyrene film, and is typical of amorphous polymers.[3, 4] Remarkably, the nanocomposite is 3.5 times more permeable and shows strong dependence on applied pressure. Such permeability increase is attributed to free-volume at the nanoparticles-polystyrene interface, which facilitates gas permeation.

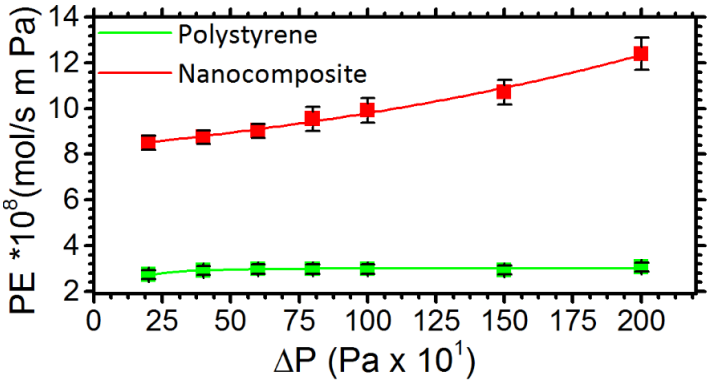

Figure 4.3: Permeability to Helium of polystyrene (green dots) and nanocomposite (red squares) films as a function of applied pressure.

The FHPS sensors investigated in this work are made of 10 bilayers of CA and ZnONPs@PS nanocomposite supported on glass substrates (Figure 4.4 a). The FHPSs appear blue, with the typical iridescence of photonic crystals (inset of Figure 4.4 b). In their reflectance spectrum, shown in Figure 4.4 b, it is indeed possible to detect a maximum of intensity in the blue region at ~460 nm, which is assigned to the PBG. In the spectrum background, an interference pattern indicates the presence of well-defined external interfaces and an overall good optical quality.[9-11]

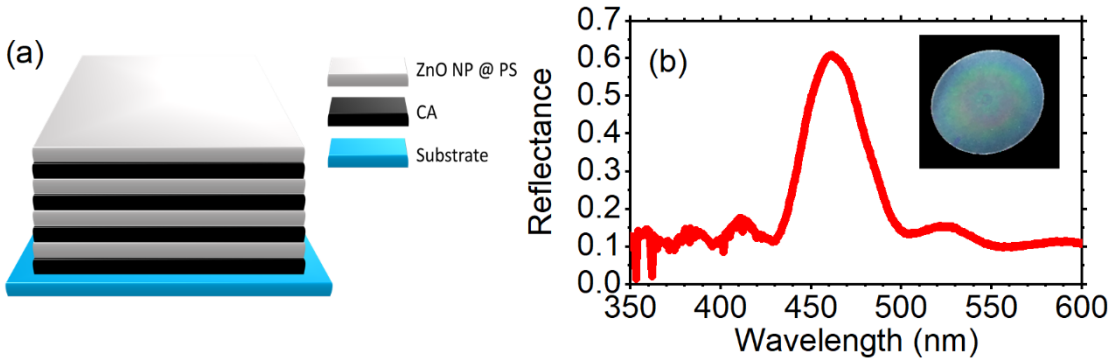

Figure 4.4: (a) Schematic, (b) reflectance spectrum and photograph of the ZnONP@PS:CA FHPS.

The DBR sample shown in Figure 4.4 was cut into different portions, and each of them was exposed to saturated vapor of BEN, TOL, o-DCB, and CTC in a close environment. Figure 4.5 shows dynamic response during the exposures. The top panels (a'- d') report the spectra

collected before the exposure (black line) and after the equilibrium saturation is reached (red line). The bottom panels show instead the dynamic response over the entire exposure time as a contour plot.

Figure 4.5 a and a', displays the data collected for CTC. The PBG is initially positioned at 460 nm and undergoes several intensity oscillations until its intensity fades at ~16 min. Contemporary, a new peak appears at 535 nm, assigned to the swollen structure. This feature undergoes a monotone red-shift until 640 nm in ~18 mins, when the response reaches the steady state. The PBG fading in the time interval between 5 min and 15 min is due to the progressive swelling of the FHPSs layers, which breaks the DBR periodicity (see Chapter 3).[6]

When exposed to BEN and TOL, the sensor shows a similar behavior, but in the case of benzene the PBG of the swollen structure is detectable at the steady-state at ~600 nm after 11 min (Figure 4.5 b and b'), while for toluene the kinetics is slower, and the PBG reaches 550 nm in the same amount of time, while it requires double the time of BEN to reach the steady state (Figure 4.5c and c'). O-DCB provides a further different response (Figure 4.5 d and d'). The PBG observed at 460 nm shows the intensity oscillation previously observed, and completely fades with 35 min of exposure. On the other hand, the spectral feature assigned to the swollen DBR sensor is not detectable. This particular effect was assigned to the large steric hindrance of this molecule, which induces severe swelling and disorder in the DBR breaking the periodicity and hindering the formation of the PBG.[12]

These very different optical responses allow to recognize the analytes. Indeed, setting an arbitrary response time, it is possible to distinguish the analyte by the different spectral position of the PBG. To this end, Figure 4.6 compares the spectra of the sensors collected after 10 min of exposure to the vapors. Here we notice that while the fingerprints of the response for TOL and BEN are similar (compares Figure 4.5 b and c), their very different dynamic allows their recognitions. Indeed, after 10 min, toluene only induce a decrease in intensity of the PBG, which appear slightly blue-shifted with respect to its initial position (compare red and black lines in Figure 4.6). Conversely, the same exposure time allows the formation of a PBG assigned to the swollen structure when benzene is used. In this case the PBG appears indeed at ~590 nm. CTC and o-DCB instead induce shifts of ~20 nm and ~30 nm respectively. These data demonstrate that the sensors response time can be as low as 10 min.

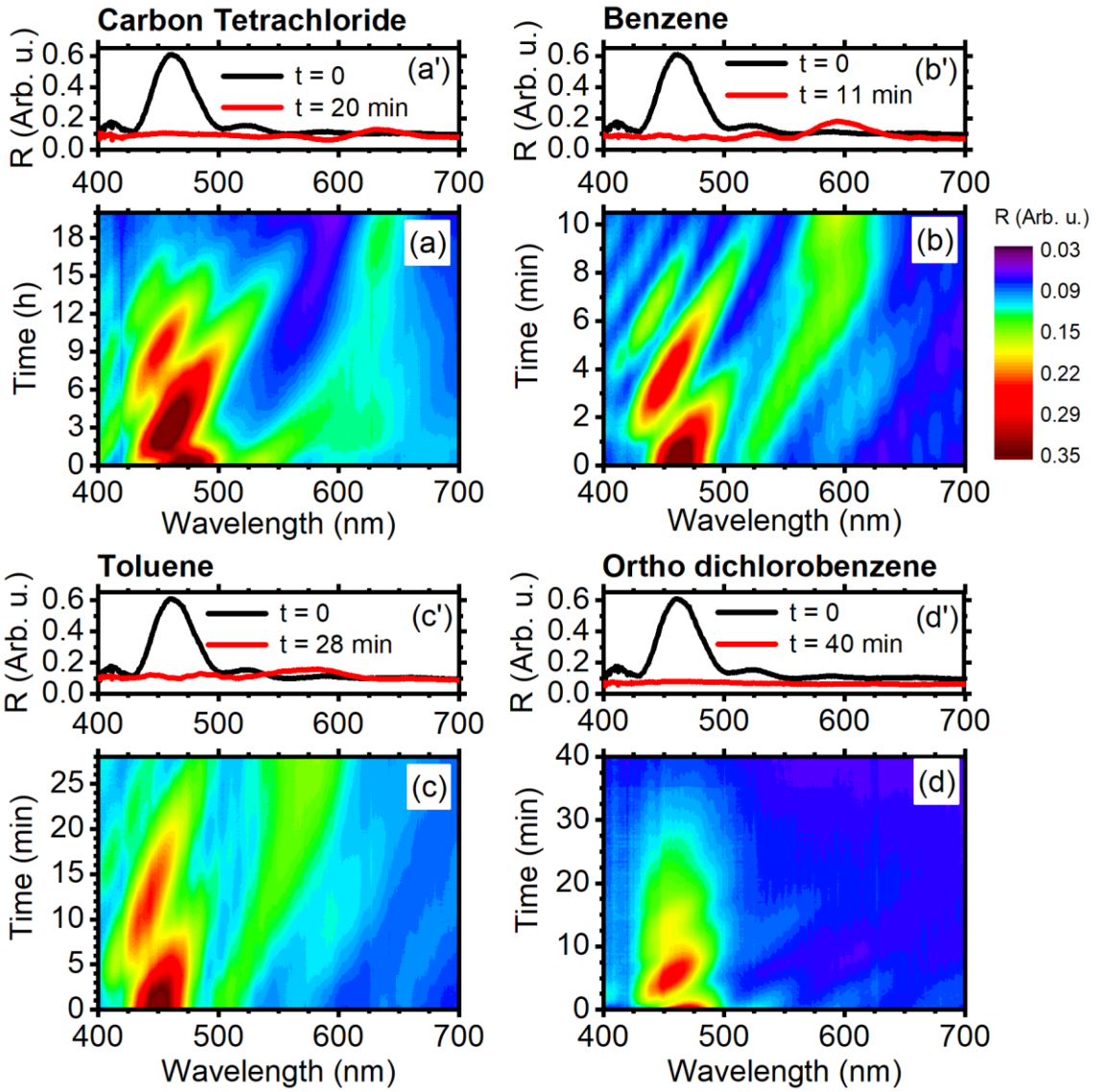

Figure 4.5: optical response of the CA:ZnONP@PS FHPS to vapors. The bottom panel reports the dynamic responses as contour plots (a-d). The top panels (a'-d') show the spectra collected before and after the exposures for CTC (a, a'), BEN (b, b'), TOL (c, c') and o-DCB (d, d').

Table 4.2 compares the optical shift of the PBG and the time required to reach saturation retrieved for the four analytes with their van der Waals volumes, and Flory-Hugging interaction parameters. We notice that for the aryl derivates (BEN, TOL, and o-DCB) the values of $\Delta\lambda_{eq}$ and t_{eq} increases with the analyte volumes and with χ_{PS}, while no correlation appears with the interaction parameter calculated for CA, confirming that the PS matrix acts as active sensing medium. No correlation between the analyte concentration and the time or spectral shift can be evinced, suggesting that the selective response is independent from these parameters. For what

concern CTC, both PBG spectral shift at saturation and saturation time do not follow the same trend, and the response time is up to 100 times slower than for benzene derivates, while the spectral shift is lower than the one induced by these molecules, which have larger van der Waals volumes. Such behavior has already been observed and can be ascribed to different intermolecular forces instauration with the two polymers with respect to the aryl derivates.[12]

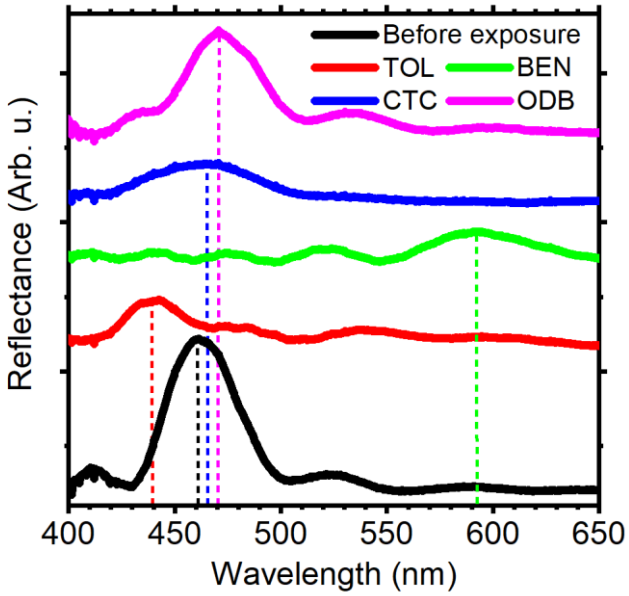

Figure 4.6: Reflectance spectra of ZnONP@PS @CA DBRs collected before (black line) and after 10 minutes of exposure to vapors of TOL (red), BEN (green), CTC (blue), o-DCB (magenta).

Table 4.2: Van der Waals Volumes (V), Flory-Huggins parameter for PS (χ_{PS}), CA (χ_{CA}) and for the entire DBR (χ_{eff}), PBG spectral shift at the equilibrium ($\Delta\lambda_{eq}$), time required to reach saturation (t_{eq}), and analyte vapor pressure.

	V (Å^3)[12]	χ_{PS}[13]	χ_{CA}[13]	χ_{eff}[13]	$\Delta\lambda_{eq}$ (nm)	t_{eq} (min)	Vapor Pressure (kPa)
BEN	89.4	0.001	1.635	1.183	130	11	10.5
TOL	106.8	0.006	2.090	1.512	120	28	2.8
O-DCB	112.8	0.088	1.223	0.887	--	40	0.13
CTC	97.1	0.008	1.942	1.406	175	>1200	11.95

This part of the project demonstrates FHPSs sensors made of commodity polymers with high optical responsivity and selectivity to benzene, toluene, 1,2-dichlorobenzene and carbon tetrachloride vapor exposure. Such systems where designed and obtained by simple

investigation of the polymer-analyte Flory-Huggins and Hildebrand parameters. This allowed sensitivity to vapors and label-free selectivity. Sensitivity and good response time were also achieved increasing the overall DBR permeability using a polystyrene-ZnO nanocomposite.

4.2 Perfluorinated Compounds

Nowadays, fluorinated products and polymers offer a wide range of materials with outstanding performances and technological solutions for high demanding applications which often constitute challenges in many key sectors like automotive, aeronautics, healthcare, energy, and storage. Properties related to performances may include chemical inertness, thermal resistance, abrasion and weathering protection, water and stain repellency, biocompatibility, transparency and many others.[14-15] Usually, these materials are soluble only in fluorinated solvents, while their non-wettability prevents the adhesion of overcoatings and makes them difficult to manage together with non-fluorinated compounds. The increasing use of these materials made the detection of perfluorinated compounds (PFC) an important task, which makes any progress to increase the capability to assess their presence highly interesting to monitor and preserve environmental health and safety.

Because the polymer-analyte interaction is critical to govern the FHPS sensitivity and the selectivity, this Paragraph proposes the use of a perfluorinated polymer (PFC-P, copolymer of tetrafluoroethylene and 2,2,4-trifluoro-5-trifluoromethoxy 1,3-dioxole, known commercially as Hyflon AD® polymer, by Solvay Specialty Polymers) to detect PFCs. In addition to its affinity with PFCs, this polymer possesses a very low refractive index (~1.33), allowing remarkable increase of the dielectric contrast with respect to polymer-pairs commonly used to grow DBRs.[8] The large dielectric contrast implies that high reflectance values can be obtained using a relatively small number of bilayers, thus saving materials and making the device fabrication faster.[16] However, as any other PFC, these polymers are highly solvophobic and scarcely wettable. This implies low mutual processability with other polymers. As a consequence, despite their optical transparency and low refractive index, very few examples of DBRs made of PFC-P have been reported in literature so far.[17-20]

The FHPSs used in this work are made of Hyflon AD® polymers (HY):PVK. While Galden HT55®®, PFPE (perfluoropolyether) polymer vapors were used as a prototype analyte. The low surface energy and solvophobicity make HY films difficult to implement into multilayered structures. To make HY layers wettable with the PVK solution, their surface was activated by

room temperature plasma treatments that improved the adhesion properties.[21-23] To develop a routine for the HY activation, we tested plasmas with different O_2/N_2 ratios.[24] The surface activation was assessed by water contact angle measurements over 24 hours after the treatment. Before the treatment the sample shows a contact angle of 119±1° (Black dot in Figure 4.7). Upon surface treatment, the contact angle dramatically decreases to an upper value of ~103° for O_2 plasma, and a lower value of 97° for air-plasma (colored dots in Figure 4.7). N_2 and different O_2/N_2 mixtures induce instead contact angles between these limit values. The surface activation was then monitored for 24 hours storing the samples in a petri dish in room conditions without any specific precaution. The data in Figure 4.7 show that small variations occur when the samples are treated with all the gas mixtures but air, where the contact angle further decreases over 24 h. These results suggest that the surface of the HY film remains wettable over time suitable for the preparation of multilayered structures. In this regard, N_2 plasma induces the lowest and more stable contact angle stable, and was then employed during the FHPSs fabrication.[25]

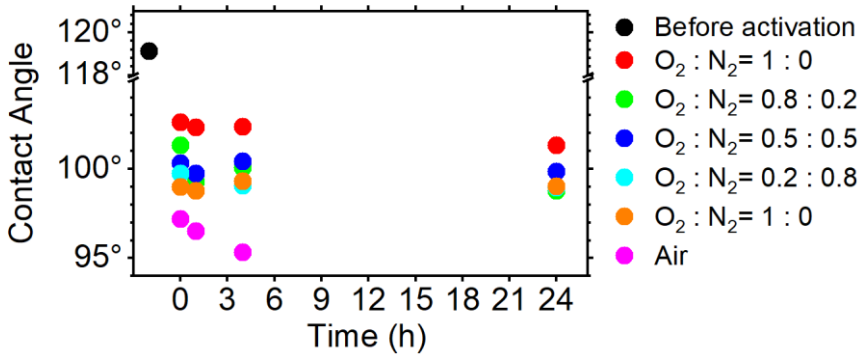

Figure 4.7: Average water contact angle of bare HY films (black dot), and after 0, 1, 4 and 24h since the plasma treatment with different O_2/N_2 mixtures (colored dots).

FHPSs were then grown on 1 in^2 glass substrate starting from the deposition of a PVK layer. After PVK deposition, a layer of HY was cast on the latter and the surface activation was performed. This operation was repeated 7 times to grow the multilayer. Figure 4.8 a and b show the photographs and Figure 4.8 c shows the spectra of a sample resulting from this routine. Panel a displays the sample as cast on the glass substrate, which appears blue and homogeneous. Panel b shows instead a similar sample after peeling-off from the substrate. The Figures demonstrates that homogeneous, free-standing, and flexible DBRs can be fabricated

with the method we proposed. The FHPS homogeneity was also confirmed by the reflectance spectra of the sample collected over six different spots of its surface. The spectra also show a well-defined interference pattern in the background, demonstrating very high quality of the top and bottom surfaces.[2] The spectra show a prominent reflectance peak at ~900 nm assigned to the PBG and a second order peak at ~450 nm, responsible for the brilliant blue color observed in the pictures reported in Figure 4.8 a and b. The very high reflectance intensity of the PBG is due to the large dielectric contrast achieved with HY and PVK.[7] The experimental spectra can be nicely reproduced with those calculated via TMM (dashed black line in Figure 4.8 c)[11, 26] using layer thicknesses d_{Hy} = 102 nm and d_{PVK} =196 nm and refractive index values d_{Hy} = 1.33[27] for HY and n_{PVK} as retrieved in previously published data.[11]

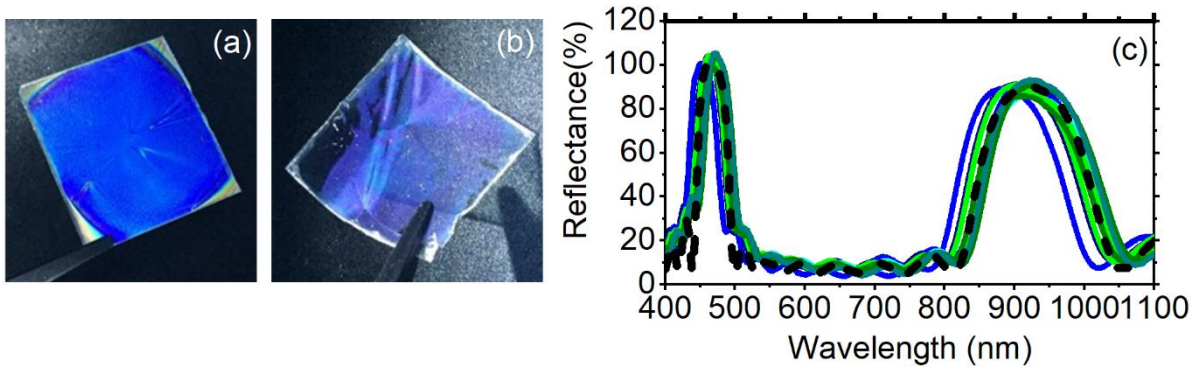

Figure 4.8: (a, b) Photographs and (c) experimental (continuous lines) and calculates (dashed line) reflectance spectra of HY: PVK DBR.

The sensitivity of the HY:PVK FHPS to fluorinated compounds was assessed exposing the sample to vapors of Galden® HT55 polymer for 100 min. Figure 4.9 a displays the contour plot of the spectra collected as a function of the exposure time. There, the PBG is observed in red tones, while the spectra background is in blue shades. At the initial stages of the exposure, the first and second order PBGs are detected at 900 nm and 450 nm respectively. These spectral features remain unchanged for the first 20 min. According to models reported in a previous work,[2] this induction time is assigned to the analyte permeation across the first PVK layer and can be increased or decreased, changing its thickness. After the induction time, the FHPS spectrum undergoes a dramatic change. The first order PBG quickly fades while shifting toward longer wavelengths. At 50 mins of exposure, it is shifted at about 1100 nm. For longer exposures, the feature keeps shifting deeper in the near infrared part of the spectrum and

broadens inhomogeneously. This behavior takes place until 90 mins of exposure, when the peak intensity decreases, and the feature cannot be distinguished clearly from the background. Concerning the second order PBG, at 450 nm, the glass substrate and the PVK absorptions reduce the effects of the analyte intercalation in the optical response. The diffraction peak remains indeed unchanged for about 20 mins, and then its intensity fades indicating the loss of periodicity of the structure (see Chapters 3 and Paragraph 4.1). To prove the role of HY in the detection of the perfluorinated compounds, we compared the response to perfluorinated analytes of CA-PVK DBRs. Figure 4.9 b shows the response of CA:PVK DBR to Galden© HT55 polymer vapors. No effects, even minor, are observed on the spectral position and intensity of the PBGs over 100 min of exposure. This demonstrates that the fluorinated analyte does not interact with the CA and PVK.

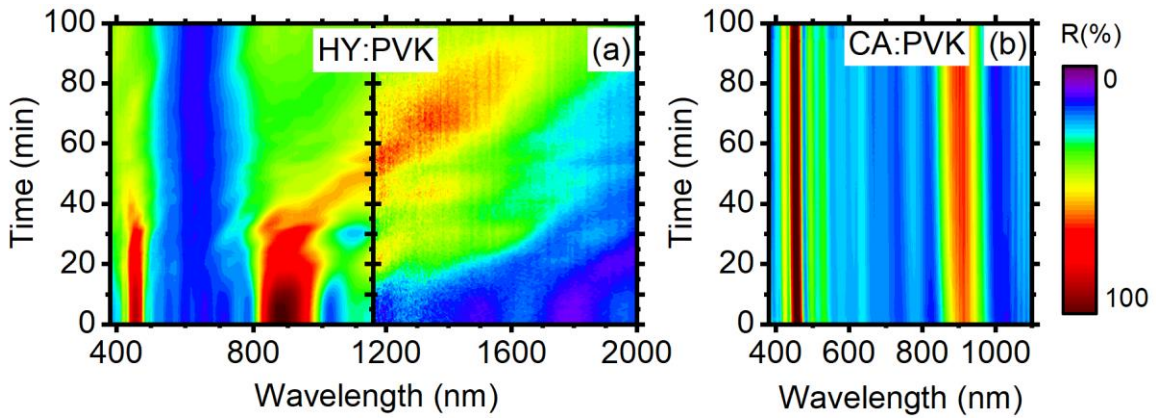

Figure 4.9:Contour plot of the (a) HY:PVK and (b) CA:PVK DBR spectra collected during the exposure to Galden® HT55 polymer saturated vapors.

The analysis of the combined optical response of the two systems to Galden® vapors clearly indicates that only the presence of a perfluorinated polymer like Hyflon AD® polymer in the DBR allows the detection of the PFC analytes. Then, HY films undergoes strong swelling upon intercalation of Galden® HT 55, inducing the strong bathochromic shift of the PBG spectral position observed. Conversely, when CA is used as low index medium, the chemico-physical interaction between the fluorinated analytes and the hydrogen-based polymer forbid the polymer swelling and the optical response. To the best of our knowledge, this is the first report for optical detection of fluorinated persistent volatile species by polymer photonic crystals.

This work represents then a proof-of-concept for easy chromatic detection of novel relevant analytes. However, a deeper investigation of the Figures of merit of the sensors, including lower detection limit, sensitivity and selectivity is necessary to develop the sensors.

4.3 Outcomes

This Chapter reports on the use of two different FHPSs for the analysis of volatile organic compounds with very different chemical structure confirming another time that the proper design of the FHPSs trough a simple study of the polymer-solvent thermodynamic parameters allow to fabricate systems sensitive to any potential analyte. In the first part we exploited PC:CA FHPSs where the PS was loaded with ZnO nanoparticles to enhance free-volume, and therefore permeability and response time. This approach allows to detect and disentangle benzene, toluene, ortho-dichlorobenzene vapors. In the second part instead, the use of a perfluorinated polymer coupled to PVK allowed to detect vapors of a perfluorinated molecule trough simple optical spectroscopy.

References

(1) Agency for Toxic Substances and Disease Registry (ATSDR). Toxicological Profiles. (accessed 28/07/2016).

(2) Straif, K.; Cohen, A.; Samet, J., *Air pollution and cancer, IARC scientific publication No. 161*. International Agency or Research on Cancer: Lyon, France, 2013.

(3) Guo, H.; Lee, S. C.; Chan, L. Y.; Li, W. M., *Environ. Res.***, 2004**, 94, 57-66**.**

(4) Wang, S.; Ang, H. M.; Tade, M. O., *Environ. Int.***, 2007**, 33, 694-705**.**

(5) Vlaanderen, J.; Straif, K.; Ruder, A.; Blair, A.; Hansen, J.; Lynge, E.; Charbotel, B.; Loomis, D.; Kauppinen, T.; Kyyronen, P.; Pukkala, E.; Weiderpass, E.; Guha, N., *Environ. Health Perspect.***, 2014**, 122, 661-666**.**

(6) Lova, P.; Manfredi, G.; Boarino, L.; Comite, A.; Laus, M.; Patrini, M.; Marabelli, F.; Soci, C.; Comoretto, D., *ACS Photonics***, 2015**, 2, 537-543**.**

(7) Gao, S.; Tang, X.; Langner, S.; Osvet, A.; Harreiβ, C.; Barr, M.; Spiecker, E.; Bachmann, J.; Brabec, C. J.; Forberich, K., *ACS Appl. Mater. Interfaces***, 2018**, 10, 36398–36406**.**

(8) Lova, P.; Manfredi, G.; Comoretto, D., *Adv. Opt. Mater.***, 2018**, 6, 1800730-26**.**

(9) Lova, P.; Cortecchia, D.; S. Krishnamoorthy, H. N.; Giusto, P.; Bastianini, C.; Bruno, A.; Comoretto, D.; Soci, C., *ACS Photonics***, 2018**, 5, 867-874**.**

(10) Manfredi, G.; Lova, P.; Di Stasio, F.; Rastogi, P.; Krahne, R.; Comoretto, D., *RSC Advances*, **2018**, 8, 13026-13033.

(11) Lova, P.; Grande, V.; Manfredi, G.; Patrin, M.; Herbst, S.; Würthner, F.; Comoretto, D., *Adv. Opt. Mater.*, **2017**, 5, 1700523.

(12) Lova, P.; Bastianini, C.; Giusto, P.; Patrini, M.; Rizzo, P.; Guerra, G.; Iodice, M.; Soci, C.; Comoretto, D., *ACS Appl. Mater. Interfaces*, **2016**, 8, 31941–31950.

(13) Hansen, C. M., *Hansen Solubility Parameters: A User's Handbook*. 2nd ed.; CRC press: Boca Raton, USA, 2002.

(14) Lindstrom, A. B.; Strynar, M. J.; Libelo, E. L., *Environ. Sci. Technol.*, **2011**, 45, 7954-7961.

(15) *CDC (Centers for Disease Control and Prevention), Fourth national report on human exposure to environmental chemicals* - Atlanta, GA, 2009.

(16) Gazzo, S.; Manfredi, G.; Pötzsch, R.; Wei, Q.; Alloisio, M.; Voit, B.; Comoretto, D., *J. Polym. Sci., Part B: Polym. Phys.*, **2016**, 54, 73-80.

(17) Convertino, A.; Valentini, A.; Ligonzo, T.; Cingolani, R., *Appl. Phys. Lett.*, **1997**, 71, 732-734.

(18) Convertino, A.; Capobianchi, A.; Valentini, A.; Cirillo, E. N. M., *Adv. Mater.*, **2003**, 15, 1103 - 1105.

(19) Song, H.; Singer, K.; Lott, J.; Wu, Y.; Zhou, J.; Andrews, J.; Baer, E.; Hiltner, A.; Weder, C., *Journal of Materials Chemistry*, **2009**, 19, 7520-7524.

(20) Karaman, M.; Kooi, S. E.; Gleason, K. K., *Chem. Mater.*, **2008**, 20, 2262-2267.

(21) Vesel, A.; Kovac, J.; Primc, G.; Junkar, I.; Mozetic, M., *Materials*, **2016**, 9, 1-14.

(22) Junkar, I., Vesel, A., Cvelbar, U., Mozetič, M. & Strnad, S. , *Vacuum*, **2009**, 84, 83-85.

(23) Vesel, A., Junkar, I., Cvelbar, U., Kovac, J. & Mozetic, M., *Surf. Interface Anal.*, **2008**, 40, 1444-1453.

(24) Radice, S. V.; Gavezoti, P.; Simeone, G.; Albano, M.; Congiu, S.; Canazza, G.; Comoretto, D. Photonic crystals. Filing date 20 March 2014, 2014.

(25) Pascu, M.; Nicolas, D.; Poncin-Epaillard, F.; Vasile, C., *J. Optoelectron. Adv. Mater.*, **2006**, 8, 1062.

(26) Manfredi, G.; Lova, P.; Di Stasio, F.; Krahne, R.; Comoretto, D., *ACS Photonics*, **2017**, 4, 1761–1769.

(27) Groh, W.; Zimmermann, A., *Macromolecules*, **1991**, 24, 6660-6663.

Chapter 5: Unstructured Commercial Polymeric Films

This Chapter reports on the use of optical spectroscopy to determine the diffusion coefficient of small molecules in commercial polymer film used in packaging. Using the same working principle demonstrated for FHPS it is indeed possible to employ the interference pattern typical of thin polymer films for the assessment of diffusion coefficients and even to recognize the analyte diffusing into the polymer itself.

This section is substantially published at:

Lova, P.; Megahd, H.; Comoretto, D. Thin Polymer Films: Simple Optical Determination of Molecular Diffusion Coefficients. ACS Applied Polymer Materials 2020, 2, 563-568

This Chapter investigates the possibility to achieve label-free selective sensors and to asses diffusion coefficients in unstructured commercial polymer thin films by means of optical spectroscopy. This task is important to evaluate barrier properties of packaging systems in food industry, in device encapsulation, and even for artwork protection.[1-2] Monitoring these properties directly on the shelf or along the fabrication line, without the need to implement a sensor in the packaging system can indeed provide significant information on both the polymer barrier properties, and on the formation of degradation byproducts. This section shows that using an approach like the one used for FHPSs, the method can be extended to commercial unstructured polymer films used in packaging. In this case, the packaging itself can be used as an active detection medium, making the method suitable for bare or multilayered polymer films used in both food industry and device encapsulation, allowing the assessment of properties that cannot be studied with standard techniques neither *in-situ*, nor for very small amounts of material.

5.1 Diffusion Coefficient and Selectivity Using Commercial Polymer Films

When their roughness is small enough, thin films provide interference patterns that depend on their thickness and refractive index. Such patterns arise from the constructive and destructive interference between light beams reflected and refracted from the upper and bottom interfaces. As depicted in Figure 5.1 a, for a film with thickness L and refractive index n, when a light beam (I_1) impinges on the film, it is partially reflected (R_1) and partially refracted (T_1) through the interface. Since the refractive index of the polymer is always larger than the one of air, $n > n_{air}$, the phase of R_1 is is shifted by $\lambda/2$ with respect to I_1.[3] The refracted beam T_1 hits instead the lower interface of the thin film where it is again partially reflected within the polymer (R_2) and partially transmitted (T_2). In this case, no phase shift occurs for the reflected beam R_2.[3] The beam R_2 reaches then the upper interface where it is transmitted and can interfere with the beam R_1. Whether the interference between the beams R_1 and T_3 is constructive or destructive depends on their phase difference. At normal incidence, without any phase shift, we would obtain constructive interference when the difference of the optical path $2nL$ equals a multiple of the beam wavelength ($m\lambda$). Because the phase of the beam $R_1$is shifted by 180 degrees, R_1 and T_2 are in-phase when the path difference $2Ln$ equals $\lambda\left(m+\frac{1}{2}\right)$.[4] This condition corresponds to full constructive interference between the two beams, that arises in the thin film

spectrum as relative maxima (Figure 5.1 b). The beams are instead out-of-phase (disruptive interference, corresponding to minima in the spectrum of Figure 5.1 b) when the path difference equals $m\lambda$. [4] When a small molecule diffuses into a polymer film, it can swell so that the thickness variation modifies the position of the interference maxima and minima. Then, the spectral variations occurring in the interference pattern during the intercalation of the molecular species can be directly linked to the variations of film thickness.

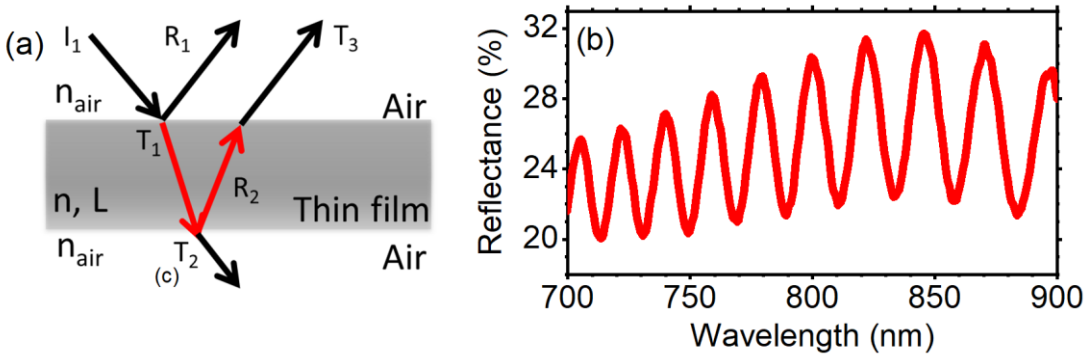

Figure 5.1: (a) Scheme of thin film reflectance. (b) reflectance of PVC film.

As a proof of principle, we exposed a commercial cling wrap film, to different solvents including some found in foods. This wrap is indeed commonly used in food packaging for preservation and protection from chemical (gases and moisture), biological (microorganisms and animals), as well as physical and mechanical damages.[5] The film composition was characterized through Raman spectroscopy. The spectrum presents four principal peaks positioned at 1429, 1310, 696 and 638 cm^{-1}, which are consistent with PVC (Figure 5.2).[6-7]

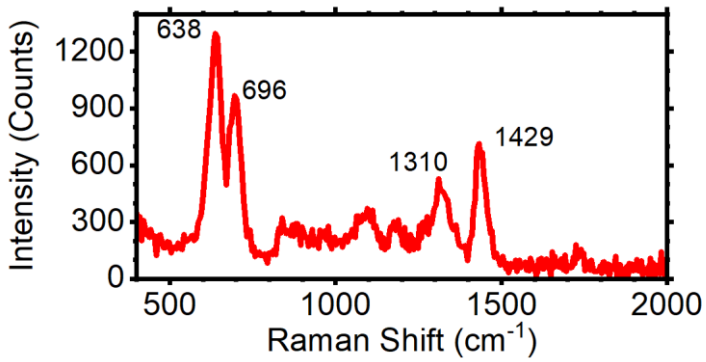

Figure 5.2: Raman spectrum of the PVC thin film

Figure 5.3 a shows the variations occurring in the interference pattern of the pristine commercial PVC cling film (red line) and after 5 min in toluene vapors (black line). The variations consist in a reduction of the reflectance intensity of the interference pattern and in a densification of the fringes. The latter characteristic is assigned to the increase of thickness of the film induced by the swelling.[8] The intensity reduction can be instead linked to two phenomena: first, the reduction of the optical quality of the PVC film and second, the decrease of the dielectric contrast at the PVC-air interface.

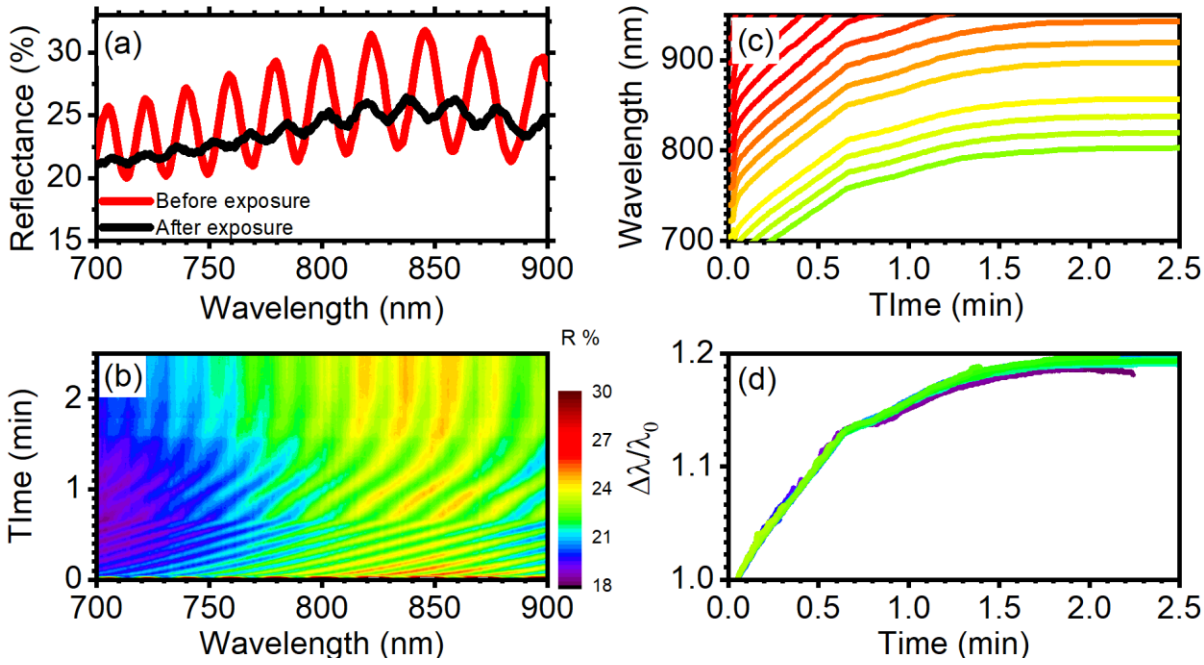

Figure 5.3: a) Response of PVC film to toluene: Reflectance of the PVC film before (red line) and after (black line) ~5 min in toluene vapor. (b) Dynamic PVC spectral response during toluene exposure (c) spectral position of relative maxima during the exposure and (d) normalized relative maxima during the exposure.

Figure 5.3 b reports the dynamic of these variations during the exposure to toluene as a contour-plot. We notice that the interference pattern is smoothly modified during the exposure. Indeed, all the fringes shift monotonically to the longer wavelengths side of the spectrum, in agreement with an increase of the film thickness. In this system, which undergoes monodimensional swelling, the volume variation induced by the intercalation of molecules can be described as the thickness variation. Moreover, dealing with vapor analytes, we can also neglect refractive index modifications,[8] so that for additive volumes the polymer mass intake (M) can be related

to the film thickness (L) as in Equation 1.8: As a consequence, it is possible to retrieve the molecular diffusion coefficient in the linear regime of the sorption from Equation 1.2. Such curves can be obtained from the data reported in Figure 5.3 b by extrapolation of the fringes spectral position (relative maxima) during the exposure. Due to the small film thickness (8.5 μm), concentration gradients that could affect the local diffusion coefficient can be neglected, as demonstrated in previous works on molecular diffusion in multilayered thin films.[8-9] Figure 5.3 c shows the retrieved data as the variation of spectral position (Δλ), while Figure 5.3 d show the normalized spectral position of the same fringes. Notice that once normalized the behavior of all the fringes is identical, and the retrieved curves are perfectly superimposable.

Notwithstanding PVC is used for its barrier properties for food preservation, it strongly interacts with many compounds. Figure 5.4 reports the evolution of spectral position of the fringe initially placed at 800 nm (Figure 5.1) collected during PVC exposure to water (a), commercial ammonia (4% in water, b), methanol (c), ethanol (d), toluene (e) and even of a perfluorinated compound (f). In all the cases, we see that the maxima shift to longer wavelengths with kinetics that depends on the different chemical species.

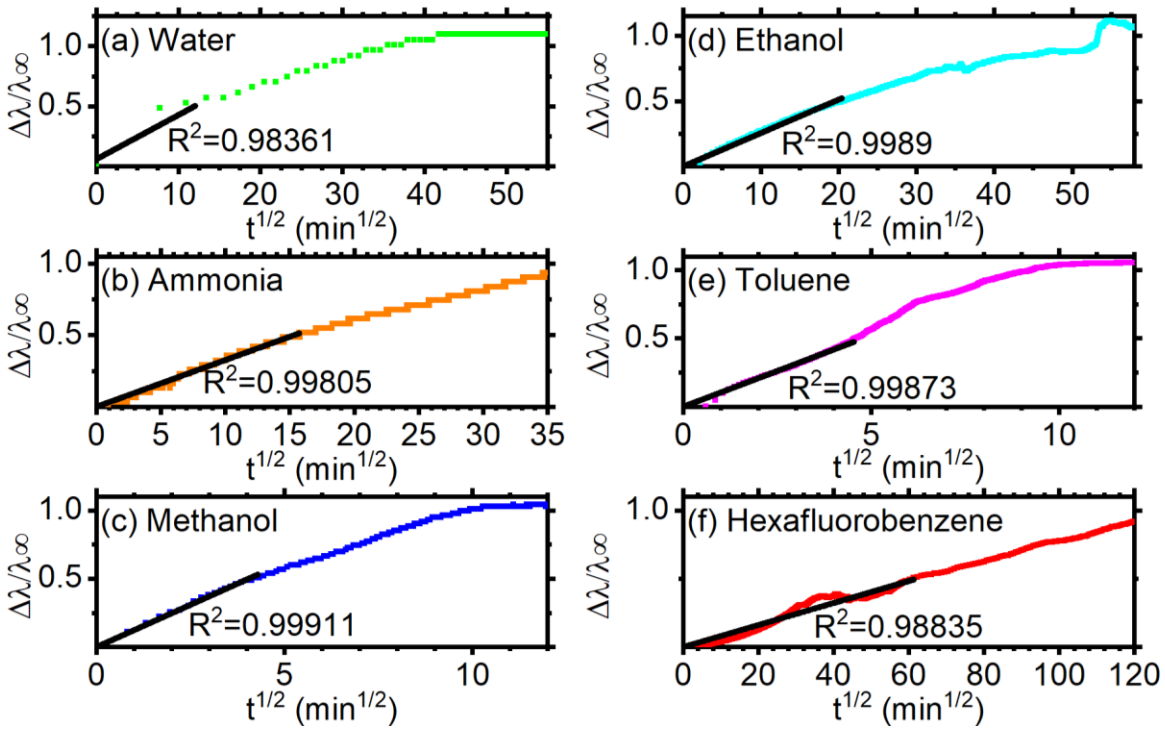

Figure 5.4: PVC optical sorption curves during exposure to water(a), ammonia solution (4% in water), b), methanol (c), ethanol (d), toluene (e), and hexafluorobenzene (f). The black line is the linear fit of the optical sorption curves retrieved for $\Delta\lambda(t)/\Delta\lambda\,(t_\infty) < 0.5$.

It is worth to notice that the large interaction between the PVC film with solvents present in food such as water and ethanol can increase the migration of plasticizers,[10] which are largely present in these films.[11] Then, decreasing such interaction could make the use of these materials safer.

The data of Figure 5.4 were analyzed accordingly to Equation 1.2 to retrieve the diffusion coefficients (*D*) within the PVC film. We did not extract the coefficient for hexafluorobenzene because the system did not reach the steady state even after 4 h of exposure. Figure 5.5 shows the value of D as black squares and compares them with different analyte properties and thermodynamic parameters for the polymer-solvent pairs (see also Table 5.1). We notice that, in opposition to the FHPSs, the diffusion coefficients appear inversely proportional to the Flory-Huggins parameter of the polymer-solvent pairs (green squares). Hence, we can state that the diffusion of the species within the film is affected by the molecular dimensions and by their solubility within the polymer.[12] The value of *D* seems to increase when the solubility increases. Figure 5.4 b also reports the quadratic difference between the Hildebrand and Hansen parameters calculated for all the analytes with respect to PVC. The Hildebrand parameter is dominated by hydrogen bonding forces (orange squares in Figure 5.4 b), while dispersive and polar forces (blue and green squares respectively in the same Figure) have a secondary role. The diffusion coefficient in PVC appears then lower for highly polar molecules (ammonia and water) that are characterized by strong hydrogen bonding making their solubilization in the PVC unfavorable and the diffusivity lower. Conversely, *D* increases when hydrogen bonding within the solvent is weaker or absent and other intermolecular forces, which are present in PVC, become predominant. Then, it appears that the formation of weak polymer-analyte intermolecular interactions increases the efficiency of the diffusion process. Concerning instead the molecular volume, it does not appear correlated to the diffusion parameter, as observed for the FHPSs. On the other hand, in analogy with the multilayered systems, it perfectly matches the optical shift of the interference pattern maxima measured at the steady state, indicating that the larger the molecular volume, the larger is the spectral shift, and thus the swelling of the polymer at the steady state. This characteristic also allows to use this simple method to discriminate molecules in the vapor phase without the use of any chemical target or complex laboratory equipment, [13]

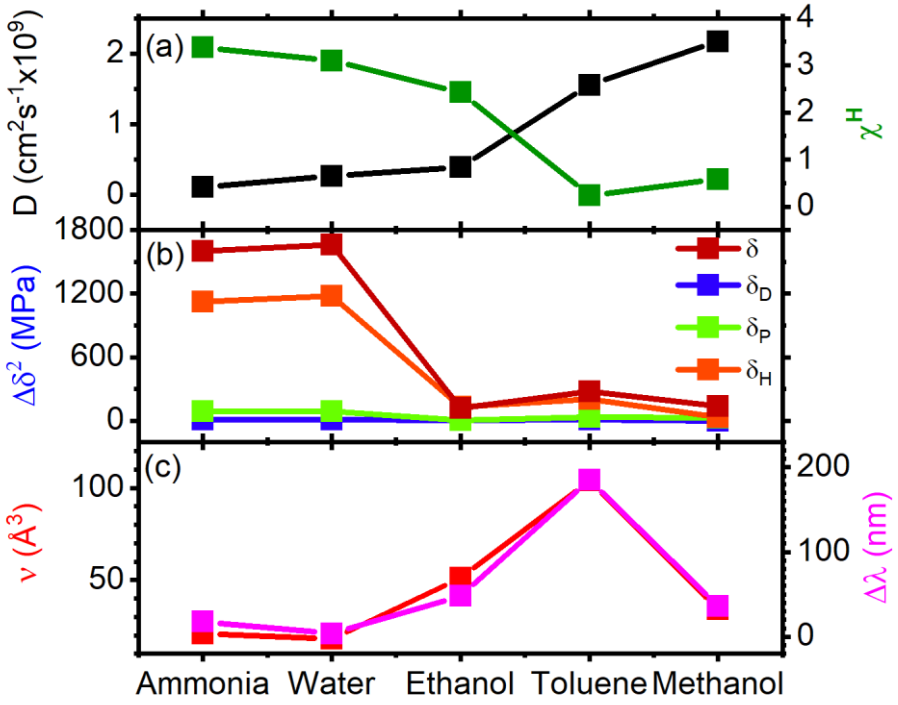

Figure 5.5: (a) Diffusion coefficient (black squares) and Flory-Huggins parameter (green squares) for ammonia, water, ethanol, toluene and methanol in the PVC film. (b) Quadratic difference between the polymer-solvent Hildebrand parameters (red), and Hansen Parameter for dispersive (blue), polar (green) and Hydrogen-bonding (orange) forces. (c) Comparison between analytes van der Waals volume and spectral shift of the relative maximum detected at 800 nm in the initial PVC reflectance spectra.[12]"

Table 5.1: Diffusion coefficient (D), van der Waals volume (ν), Quadratic difference of the Hildebrand Parameters ($\Delta\delta^2$), Flory-Huggins Parameter (χ^H), percentual optical shift of the interference pattern (Δλ) and the concentration for the 5 analytes.

	D (cm²/s)	ν (Å³)[12]	$\Delta\delta^2$ (MPa)[12]	χ^H	Δλ (%)	Concentration (mg/L)
Ammonia	1.1 E-10	21	666	3.4	1.5	23
Water	2.7 E-10	18	707	3.1	1	23
Ethanol	3.9 E-10	51	195	2.4	7	155
Toluene	1.6 E-9	104	9	0.2	20	120
Methanol	2.2 E-9	34	70	0.6	5	238

The values of diffusion coefficient retrieved optically are in good agreement with literature data where available. For instance, the literature coefficient for the two alcohols varies between 10^{-9} and 10-12 cm²/s,[14] while the value for water ranges from 10^{-5} to 10^{-9} cm²/s.[14-15] We would like to highlight that the differences in the coefficient retrieved for water may arise because we

performed the measurement in equilibrium with the environmental humidity instead of on dry films. This makes the water concentration larger than zero in the PVC, and thus the diffusion driving force smaller and the process slower. Moreover, the diffusion coefficient can vary by orders of magnitude depending on the polymer molecular weight,[16] thickness,[17-19] and on the use of additives and plasticizers that are widely used in commercial films. In any case, to be compatible with the PVC films, the plasticizers Hildebrand parameters must be similar to those of the PVC cling, then, we do not expect strong variation of the value reported in this discussion for the neat film.

5.2 Outcomes

This Chapter demonstrates that the diffusion coefficient of molecular species in the vapor phase can be performed by mean of simple optical spectroscopy also for polymer thin films used for food packaging. This method is based on the thickness variation of the polymer thin film induced by the diffusion of molecules and on the variation of the interference pattern of the film itself. The procedure allows the simple extraction of optical sorption curves that can be employed to assess the diffusion coefficient. Moreover, this approach allows to easily distinguish different penetrants, providing a smart tool for assessment of goods quality directly in the shelf.

Comparing these results with those obtained for the FHPSs, we can reasonably state that the possibility to use the packaging itself as active medium can certainly extend the method to several systems, without the need to implement a photonic structure in the polymer film. On the other hand, the possibility to obtain colorimetric response to the presence of an analyte that can be identified by any user is of great interest for safety devices and smart labelling.

References

(1) Giuliani, C.; Pascucci, M.; Riccucci, C.; Messina, E.; Salzano de Luna, M.; Lavorgna, M.; Ingo, G. M.; Di Carlo, G., *Prog. Org. Coat.*, **2018**, 122, 138-146.

(2) Salzano de Luna, M.; Castaldo, R.; Altobelli, R.; Gioiella, L.; Filippone, G.; Gentile, G.; Ambrogi, V., *Carbohydr. Polym.*, **2017**, 177, 347-354.

(3) Hecht, E., Chapter 4: The Propagation of Light In *Optics*, 5th ed.; Limited, P. E., Ed. Pearson Education Limited: Harlow, 1998; pp 147-148.

(4) Hecht, E., Chapter 9: Interference. In *Optics*, Pearson Education Limited: Harlow, 1998;

pp 416-418.

(5) Marsh, K.; Bugusu, B., *J. Food Sci.*, **2007**, 72, R39-R55.

(6) Solodovnichenko, V. S.; Polyboyarov, V. A.; Zhdanok, A. A.; Arbuzov, A. B.; Zapevalova, E. S.; Kryazhev, Y. G.; Likholobov, V. A., *Procedia Eng.*, **2016**, 152, 747-752.

(7) Kerr, T. J.; Duncan, K. L.; Myers, L., *Vib. Spectrosc.*, **2013**, 68, 225-235.

(8) Lova, P.; Manfredi, G.; Bastianini, C.; Mennucci, C.; Buatier de Mongeot, F.; Servida, A.; Comoretto, D., *ACS Appl. Mater. Interfaces*, **2019**, 11, 16872-16880.

(9) Lova, P.; Manfredi, G.; Boarino, L.; Comite, A.; Laus, M.; Patrini, M.; Marabelli, F.; Soci, C.; Comoretto, D., *ACS Photonics*, **2015**, 2, 537-543.

(10) Sharma, V.; Nani, D.; Kumar, R., *Spectrochim. Acta, Part A*, **2019**, 206, 558-568.

(11) Union, E. Allowed Plasticizers and Additives in EU - https://eur-lex.europa.eu/eli/reg/2011/10/oj. (accessed 4 June 2019).

(12) Hansen, C. M., *Hansen Solubility Parameters: A User's Handbook*. 2nd ed.; CRC press: Boca Raton, USA, 2002.

(13) Pavia, D. L., *Introduction to Organic Laboratory Techniques: A Small Scale Approach*. 2nd ed.; Thomson Brooks/Cole: Belmont, USA, 2005; Vol. 1, p 1021.

(14) Mura, C.; Yarwood, J.; Swart, R.; Hodge, D., *Polymer*, **2001**, 42, 4141-4152.

(15) Cox, S. S.; Zhao, D.; Little, J. C., *Atmos. Environ.*, **2001**, 35, 3823-3830.

(16) Tiemblo, P.; Guzmán, J.; Riande, E.; Mijangos, C.; Reinecke, H., *Polymer*, **2001**, 42, 4817-4823.

(17) Lin, E. K.; Wu, W.-l.; Satija, S. K., *Macromolecules*, **1997**, 30, 7224-7231.

(18) Frank, B.; Gast, A. P.; Russell, T. P.; Brown, H. R.; Hawker, C., *Macromolecules*, **1996**, 29, 6531-6534.

(19) Hall, D. B.; Miller, R. D.; Torkelson, J. M., *J. Polym. Sci. Part B Polym. Phys.*, **1997**, 35, 2795-2802.

Chapter 6: Discussion and Perspectives

In this section we discuss the results achieved during this Thesis project and propose a research path for further development of polymer FHPSs for selective detection of vapor pollutants and monitoring of packaging systems.

This Thesis first introduced the issues related to the assessment of vapor molecules in air and packaging. The current techniques imply the use of quantitative portable detectors or laboratory analysis to retrieve qualitative information. Conversely, the presence of molecular species such as degradation markers or moisture in packaging is not assessed continuously. Moreover, also the determination the barrier properties of these packaging requires laboratory instrumentation and cannot be performed *in-situ*. In this sense, as explained in Chapter 1, quali-quantitative colorimetric sensors that provide a simple colorimetric response are of high technological relevance both to allow immediate and extensive air quality monitoring, and for the assessment of the quality of goods in packaging. In this regard, the possibility to asses also barrier properties and diffusivity of small molecule in the polymer packaging itself could further enhance goods control and shelf-life. As explained in the introduction, polymeric DBRs demonstrated promising achievement in the detection of vapor pollutants. Previous works showed that these systems can display broad label-free selectivity to a variety of analytes with lower detection limit of few parts per million and sensitivity below 1 ppm. On the other hand, the selectivity mechanism was not fully understood and a general method for the design and fabrication of these sensors was not proposed.

Paragraph 1.3 depicts the working principle of new sensors treating the polymer thin films as dense matrices that undergo intercalation of the analytes and solubilize them. It also envisages the possibility to use the spectral responses of these systems to define the diffusion coefficient of the molecular species intercalating within the polymer slabs using simple optical spectroscopy and classical diffusion models.

After describing the experimental procedures, in Chapter 3 this method is applied to PS:CA multilayers demonstrating that their response can be used in a duplex manner, first the full dynamic spectral response is used to extract optical sorption curves and the diffusion coefficients for short chain alcohols. Second, was employed to disentangle pure alcohols trough the analysis of the diffusion kinetics and even binary mixtures using multivariate analysis. Also, the analysis of the retrieved coefficients, compared with the polymer-solvent thermodynamic parameters (Flory-Huggins and Hildebrand parameters) allows to design a general method for the fabrication of FHPSs that can be potentially used to achieve responsivity and selectivity to any analyte. Such method is tested in Chapters 4 and 5, where the FHPSs were designed to disentangle analytes from different families, including hydrocarbons and even perfluorinated compounds. The simple analyses of Flory-Huggins interaction parameters

allowed indeed to design sensors able to detect and disentangle toluene, benzene, ortho dichlorobenzene and carbon tetrachloride. This result was achieved using CA as barrier active material to rule the diffusion kinetics and a ZnO nanoparticle-PS nanocomposite as sensitive medium. The use of a perfluorinated polymer also allows to easily detect a perfluorinated compound in the vapor phase.

Most interestingly, the working principle of FHPSs can also be demonstrated for unstructured films commonly used in packaging. Chapter 5 shows that the method can be applied even to commercial polymer films used in every kitchen. The analysis of the interference pattern of a PVC cling wrap demonstrated indeed that it is possible to use the dynamic variation of its interference patter to asses both the diffusion coefficient and the species intercalating.

These results are very promising for the development of lab-on-a-chip devices as well as portable instrumentation that can be used in polluted environment and to asses barrier properties *in-situ.* On the other hand, the technology is still immature for real application (Technology readiness level, TRL 4). This Thesis provides a new methodology that now need to be optimized and tested *in-situ*. The future path of the project then aims to develop commercial systems through the following steps:

- *Design the ideal geometry of the FHPF in term of number of layers and layer thickness*. Indeed, while this Thesis demonstrates that unstructured film can replace FHPSs, they lack colorimetric response that make the sensors ON-OFF detectors suitable for smart labelling or safety devices. To this end, several FHPS made with different number of layers and/or with different layer thickness are currently under investigation to identify the systems providing the faster response with the largest sensitivity.
- *Creation of a response library:*

  Once developed the sensitive elements, the DBR spectral response will be investigated during exposure to pure vapors and their mixtures to build a database of kinetic responses to pure analytes and mixtures. The sensor response will be assigned by multivariate analysis.
- *Development of a measuring prototype and test in-situ*

  All the optical set-up used in this Thesis project are based on optical fibers and portable light sources and detectors. One of the next steps to reach real application will be the further miniaturization of the systems to obtain a full-portable system for the detection of vapor in polluted environments using FHPSs and to be used directly in packaging films. Once the prototype will be tested in the lab, it will be used to assess the technology *in-situ.*

Although the use of FHPSs in real environment still represent a challenge, the results reported in this Thesis appears technologically relevant and promise a new powerful tool for the monitoring of vapor species.

Chapter 7: Related Project

This section reports on the use of polymer planar photonic crystals and microcavity for light emission control and lasing. This project, together with the other discussed in this Thesis aims to demonstrates that polymer photonic structures are technologically feasible.

The Chapter first introduces the concept of microcavities, and their effect on light matter interaction. Then, it briefly discusses the results achieved in both light emission control and in lasing, demonstrating the capability to couple several emitters, including perovskites, organic molecules and inorganic nanocrystals into microcavity structures.

This section is substantially published at:

- Lova, P. et al.,Advances in Functional Solution Processed Planar One-Dimensional Photonic Crystals, *Adv. Opt. Mater.*, **2018**, 6, 1800730-26**.**
- Lova, P. et al., All-Polymer Methylammonium Lead Iodide Perovskite Microcavity, *Nanoscale*, **2019**, 11, 8978-8983
- Lova, P. et al.,Solution Processed Polymer-ABX_4 Perovskite-Like Microcavities, *Appl. Sci.*, **2019**, 9**.**
- Lova, P. Et al., Engineering the Emission of Broadband 2D Perovskites by Polymer Distributed Bragg Reflectors, *ACS Photonics*, **2018**, 5, 867-874**.**
- Lova, P. et al., All-Polymer Photonic Microcavities Doped with Perylene Bisimide J-Aggregates, *Adv. Opt. Mater.*, **2017**, 5, 1700523**.**
- Manfredi, G. Et al.,Lasing From Dot-In-Rod Nanocrystals in Planar Polymer Microcavities, *RSC Advances*, **2018**, 8, 13026-13033**.**
- Manfredi, G. Et al., Directional Fluorescence Spectral Narrowing in All-Polymer Microcavities Doped with CdSe/CdS Dot-in-rod Nanocrystals, *ACS Photonics*, **2017**, 4, 1761–1769**.**
- Lova, P. et al., All-Polymer Photonic Microcavities Doped with Perylene Bisimide J-Aggregates, *Adv. Opt. Mater.*, **2017**, 5, 1700523**.**

In parallel to this Thesis work, other projects aimed to demonstrate the feasibility of polymer photonic structure in optoelectronic devices where carried out focusing on emission control and lasing. The possibility to enhance the emission intensity of a material, together with the possibility to reshape its spectral profile and directionality, is indeed of great interest for lightening devices, including LED and for lasing. So far, these applications have been limited to inorganic bulky dielectric media due to their large dielectric contrast (see Appendix A.2). On the other hand, as discusses in Chapter 1, beside their high performances bulky inorganic photonics need for complex and time demanding high vacuum processing, that forbids the mass scale production and the use of temperature sensitive emitters.[1-2] Polymer building blocks can overcome these limitations thanks to well-known solution and melt processings.[3] Moreover, they allow to couple the photonic structures to a variety of dyes including inorganic, hybrid, molecular and polymer photoemitters. This Chapter will discuss the possibility to implement such materials within polymer microcavities and their performances.

7.1 Microcavities

Before discussing the effects of photonic structures on photoemitters, it is useful to make a brief introduction to microcavities (MCs). As depicted in Figure 7.1 a, the insertion of a defect layer in a DBR lattice creates a microcavity. The defect layer, with thickness L_c and refractive index n_c, breaks the DBR periodicity and creates allowed photonic states within the PBG, the so-called the cavity modes. Then, the MC reflectance spectrum shows a very sharp feature with low intensity within the PBG band (Figure 7.1 b) with spectral position depending on the resonance condition within the optical path of the cavity layer, which generates a standing wave with wavelength λ_c:

$$2n_cL_c = m\lambda_c \tag{7.1}$$

The spectral full width half maximum (FWHM, $\Delta\lambda_c$) of the cavity mode is mainly affected by the reflectivity of the DBRs surrounding the defect (R_{bottom} and R_{top}) and represent the Figure of merit for these structures, that is the quality factor (Q-factor):[4-5]

$$Q = \frac{\lambda_c}{\Delta\lambda_c} = \frac{2\pi n_c L_{eff}}{\lambda_c} \frac{1}{\alpha L_{eff} - ln\sqrt{R_{bottom}R_{top}}} \quad (7.2)$$

where L_{eff} *is* the effective cavity length (Equation 7.4) and α is factor that accounts common loss mechanisms. The Q-factor is then defined by the total energy stored in the cavity and by the energy dissipation rate. For α constant, higher reflectance result in a higher Q-factor and then, in a sharper cavity mode. For polymer microcavities, this value spans in the range 40-250.[6-10] values approaching 10^3, are typical of MCs fabricated by vacuum technologies with bulky inorganic materials,[11-12] while those using metal oxide nanoparticles and those employing metallic mirrors, which introduce loss mechanisms, show Q~10.[13-14] Notwithstanding polymer MCs show relatively low Q-factor, they present superior mechanical properties, easy processing and economic advantages. These characteristics secure the research in the integration of several novel photoactive materials including organic molecules,[6-7, 10, 15-18] inorganic quantum dots,[9] hybrid perovskites,[19] photochromic and non-linear organic materials,[16, 20-23] which are hardly compatible with the high temperature processing of inorganic bulky and mesoporous DBRs.[7-9, 16, 24-29]

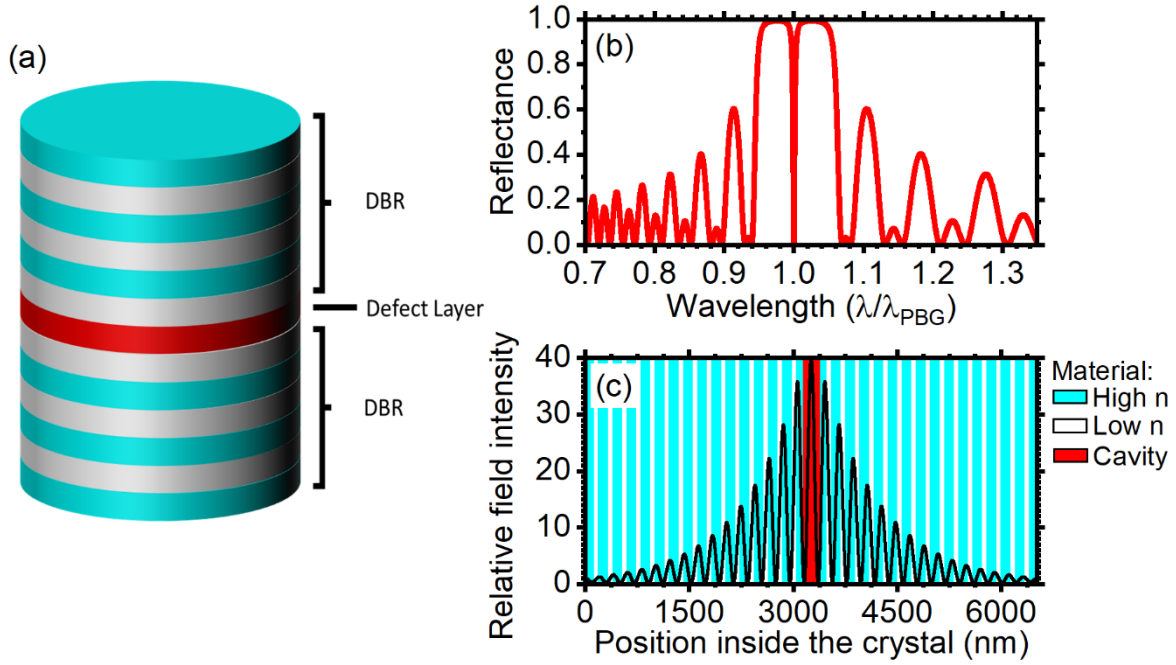

Figure 7.1: (a) Schematic of a MC. (b) Calculated reflectance spectrum of a polymer planar MC. (c) Intensity of electric field inside a planar PVK:CA MC.

7.1.1 Emission Enhancement

Conversely to DBRs, MCs allow strong spatial light confinement, that modifies light-matter interaction when fluorophores are embedded within the defect layer.[6, 10] This allows emission intensity enhancement, strong directional control and spectral redistribution.[6, 17, 30] Such effects depend on the MCs modal volume, a small volume permits tighter light confinement within the resonator and intensifies light-matter interactions.[5, 31-36] In the case of dielectric mirrors the field penetrates the DBRs and low confinement is commonly achieved. [37] The modal volume can be easily linked to the microcavity effective length (L_{eff}) by simple geometrical considerations:

$$L_{eff} = L_C + L_{DBR} = L_C + \frac{\lambda_c}{2n_c}\frac{n_L}{n_H}(n_H - n_L) \tag{7.4}$$

Where L_{DBR} sums the length of light penetration within the two DBRs at the cavity mode wavelength. Equation 7.4 shows that the distribution of the electromagnetic field is centered within the cavity layer and extends into the DBR mirrors depending on their dielectric contrast. This effect is shown in Figure 7.1 c for a PVK:CA microcavity containing a PVK defect layer. For low dielectric contrast media, including polymers and highly porous systems, relatively large L_{DBR} values generate large cavity volumes. Since several light-matter interaction mechanism like strong-coupling and Purcell effect require small cavity volumes,[4, 32-35, 38-41] observation of such effects in polymer and mesoporous inorganic systems have not been reported so far.

As mentioned above, the cavity modifies the fluorescence of fluorophores embedded into the cavity layer. This action deals with the fundamental light-matter interaction process. We must remind that optical transitions are driven by the Fermi's golden rule:

$$W(\omega) = \frac{2\pi}{\hbar}|< \boldsymbol{\mu} \cdot \boldsymbol{E} >|^2 \rho(\omega) \tag{7.5}$$

Where $\boldsymbol{\mu}$ is the transition dipole moment, **E** is the electric field, and $\rho(\omega)$ is the final electronic density of states. In PhCs, we must consider **E** related to the allowed optical modes $\mathbf{E}_{n,\mathbf{k}}(\mathbf{r}, \omega)$

of the photonic band structure ($\omega_{n,\boldsymbol{k}}$) and, introducing the local PDOS ($\rho_l(\mathbf{r},\omega)$), the transition rate becomes:[6, 36, 42-46]

$$W(\omega) = \frac{2\pi}{\hbar}\rho_l(\boldsymbol{r},\omega) = \frac{2\pi}{\hbar}\frac{1}{2\pi^3}\sum_n \int d^3\boldsymbol{k} \left| < \boldsymbol{\mu}\cdot\boldsymbol{E}_{n,\boldsymbol{k}}(\boldsymbol{r},\,\omega) > \right|^2 \delta\left(\omega - \omega_{n,\boldsymbol{k}}\right) \qquad (7.6)$$

To understand the role of ($\rho_l(\mathbf{r},\omega)$) on the emission, we need to consider its relation with the Q-factor at the cavity mode:[36, 47-48]

$$\rho_l(\boldsymbol{r},\omega) \propto \frac{1}{\Delta\lambda_c} \propto Q \qquad (7.7)$$

This effect is sketched in Figure 7.2. For a homogeneous medium the PDOS has a parabolic energy dependence (Figure 7.2 a), while in a DBR it is suppressed at the PBG with a slight increase at its edges (Figure 7.2 b).[45-46, 49-50] In a MC, a sharp peak in the PDOS arises at the cavity mode within the PBG (Figure 7.2 c).[6, 36] Then, when an emitter, whose luminescence is tuned on the PBG is inserted in the cavity layer and overlapped to the MC standing wave antinodes, the PDOS is suppressed at the PBG frequencies and increased at the cavity mode ones. This results in a drastic spectral redistribution of the emission (Equation 7.6), which includes the directionality properties of the photonic band structure (see Appendix A.2) and can be observed in angle resolved fluorescence spectra.[8-9]

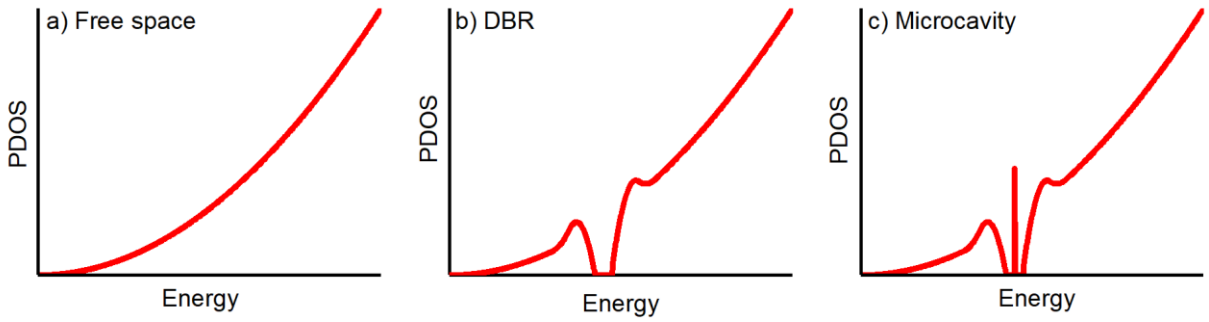

Figure 7.2: Schematics of the PDOS (a) in free space, (b) in a DBR, and (c) in a MC.

Embedding an emitter in a MC can give rise to three effects:

- When the emitter photoluminescence is spectrally broader than the PBG, photons normally emitted at its frequencies are funneled within the cavity mode, accordingly to the PDOS, resulting in an emission intensity enhancement at λ_c and in an intensity suppression at the PBG. Outside the PBG, no major effects are observed.[6, 8-9, 51-52]
- In the second case, the emitter spectrum is spectrally sharper than the PBG but larger than $\Delta\lambda_c$. In this case a sharpening of the emission and a strong increase of intensity occurs.
- Eventually, when the free-space emission spectrum is sharper than both $\Delta\lambda_c$ and the PBG, only an intensity variation occurs joined to a modification of the radiative rate.[4, 38, 40-41, 53-55] So far, this effect has not been reported for polymer MCs.

Moreover, as mentioned above, the spectral redistribution of the fluorescence oscillator strength varies strongly also with the collection angle. Indeed, the dot product of the dipole moment vector and the electric field of the cavity standing wave provides an angular dependence, in agreement with the photonic band structure dispersion (see Appendix A).[4, 54]

7.1.2 Lasing

Microcavities become particularly attractive when the fluorophore shows amplified spontaneous emission (ASE). ASE occurs when the material undergoes population inversion by effect of an external optical pump. When the gain associated to the population inversion exceeds losses due to the microcavity imperfections and material absorption, the lasing action starts. The thresholds (P_{th}) of the process is given by:[4, 56-57]

$$P_{th} = \frac{\hbar\omega_c^2}{2Q\beta} = \frac{\pi h}{Q\beta}\nu_c^2 \tag{7.8}$$

Where β is the spontaneous emission coupling factor, which provides the fraction of the total spontaneous emission rate emitted into the laser mode (above 10% for inorganic MCs).[4] Equation 7.8 also highlights the importance to increase the Q-factor to lower the lasing threshold. In solution processed MCs, the Q-factor is strictly connected to the material processability and to the dielectric contrast.

Since the first demonstration of ASE in conjugated polymers, both in solution and polymer blends,[58-59] optically pumped solid state organic laser gained a widespread interest and are still in the spotlight for their potential use in several fields.[60-61] Lasing action in MCs based on a conjugated polymer was first reported in 1996[62] for a feedback structure consisting in a metal mirror and an inorganic DBR. Following this result, two inorganic DBRs have been employed as feedback structure to gather lasing by conjugated copolymers.[63] The first flexible laser was demonstrated for distributed feedback cavities where a diffraction grating acting as Bragg reflector was implemented into a planar waveguide. In this case, vertical emission on the second order diffraction occurs (Figure 7.3 a and b).[64] This structures can be easily produced by soft lithography. Sophisticated structures can be even adapted to biochips as membrane lasers (Figure 7.3 f ang g).[60-61, 65-71] After these milestones, lasing action was achieved with several structures including microdisks (Figure 7.3 c),[72] and whispering gallery fibers (Figure 7.3 d).[73] Infiltrated opaline structures are instead efficiently used to achieve distributed feedback (DFB) and random lasing.[74-75]

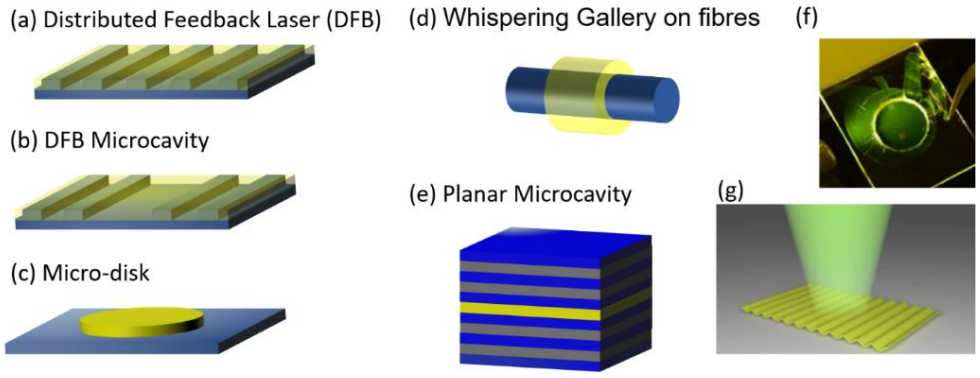

Figure 7.3: (a-g) Different lasing cavity structures achieved both with organic and inorganic systems.[68] (f) Example of membrane DBR laser adaptet to a biochip.[61]

7.2 Polymer Planar Microcavities for Emission Enhancement

This Paragraph shortly summarize part the result achieved on emission intensity enhancement. Obtained embedding hybrid perovskites, J-aggregates and inorganic nanocrystals in polymeric MCs. For brevity, only the spectral effects will be discussed while effect on emission rate and outcoupling will be only summarized.

7.2.1 Hybrid Perovskite Emitters

Thanks to high photoluminescence efficiencies, large charge carrier diffusion, and easy solution processing, hybrid organic-inorganic perovskites have been largely investigated for a variety of flexible optoelectronic devices.[76-80] However, their deposition often requires solvents able to dissolve most of commercial polymers, limiting the possibility to couple this active media with flexible polymer devices. For instance, white emitting bidimensional perovskites are very interesting for lightening applications.[19, 81-88] Indeed, coupling this emitters with all polymer structures processed from solution and able of single color emission enhancement or suppression would lead to reduction of fabrication cost and simplification of fabrication processes in lightening devices. On the other hand, the necessity to process the perovskite from broad-spectrum solvents such as dimethyl formamide (DMF) or dimethyl sulfoxide (DMSO), which would dissolve many polymers, makes perovskite incompatible with polymer processing. During this Thesis project, different strategies and architectures were employed to fabricate polymer MCs embedding perovskite emitters. This Paragraph shortly summarizes the results achieved employing a white emitting perovskite 2,2'-(ethylenedioxy)bis(ethylammonium) lead chloride ((EDBE) $PbCl_4$) and methylammonium lead iodide (MA PbI_3) perovskites provided by the group of Prof. Cesare Soci from the Nanyang Technological University of Singapore.

The top panels (a, b, and c) of Figure 7.4 show the schematics of the three architectures used to couple the hybrid perovskite thin films with planar polymer photonic structures. The first one is the simplest (Figure 7.4 a). In this case an (EDBE) $PbCl_4$ film is casted on substrates of fused silica or thick polyethylene terephthalate. A DBR made of PS and CA is successively spun-cast on top of this perovskite film.[19] The spectra of the sample surface Figure 7.4 a' are nicely superimposable indicating the homogeneity of the sample. All the spectra show a maximum in the reflectance intensity at 510 nm, assigned to the PBG, and an interference pattern which assesses the good optical quality of the sample. For what concern the effect of the photonic structure on the broad perovskite emitter, this kind of structure does not allow the formation of a cavity mode. On the other hand, in Figure 7.4 a" where the emission spectrum of the bare perovskite thin film (black line) is compared with the one of the photonic structures (red line), it is possible to see that the bare (EDBE) $PbCl_4$ emission appears quite broad ranging from 400 nm to more than 600 nm and is peaked in the green region of the spectrum. When the

emitter is coupled to the polymer DBR, the emission spectrum is strongly modified. Indeed, its intensity is enhanced in the entire range due to better light extraction (see also Figure 7.4 a'''), moreover the emission spectrum result modulated by both the PBG and the interference patter. A Peak of intensity enhancement is detected slightly below 500 nm, Such effect was assigned to a weak coupling regime favoured by the low reflectivity of the substrate.[19]

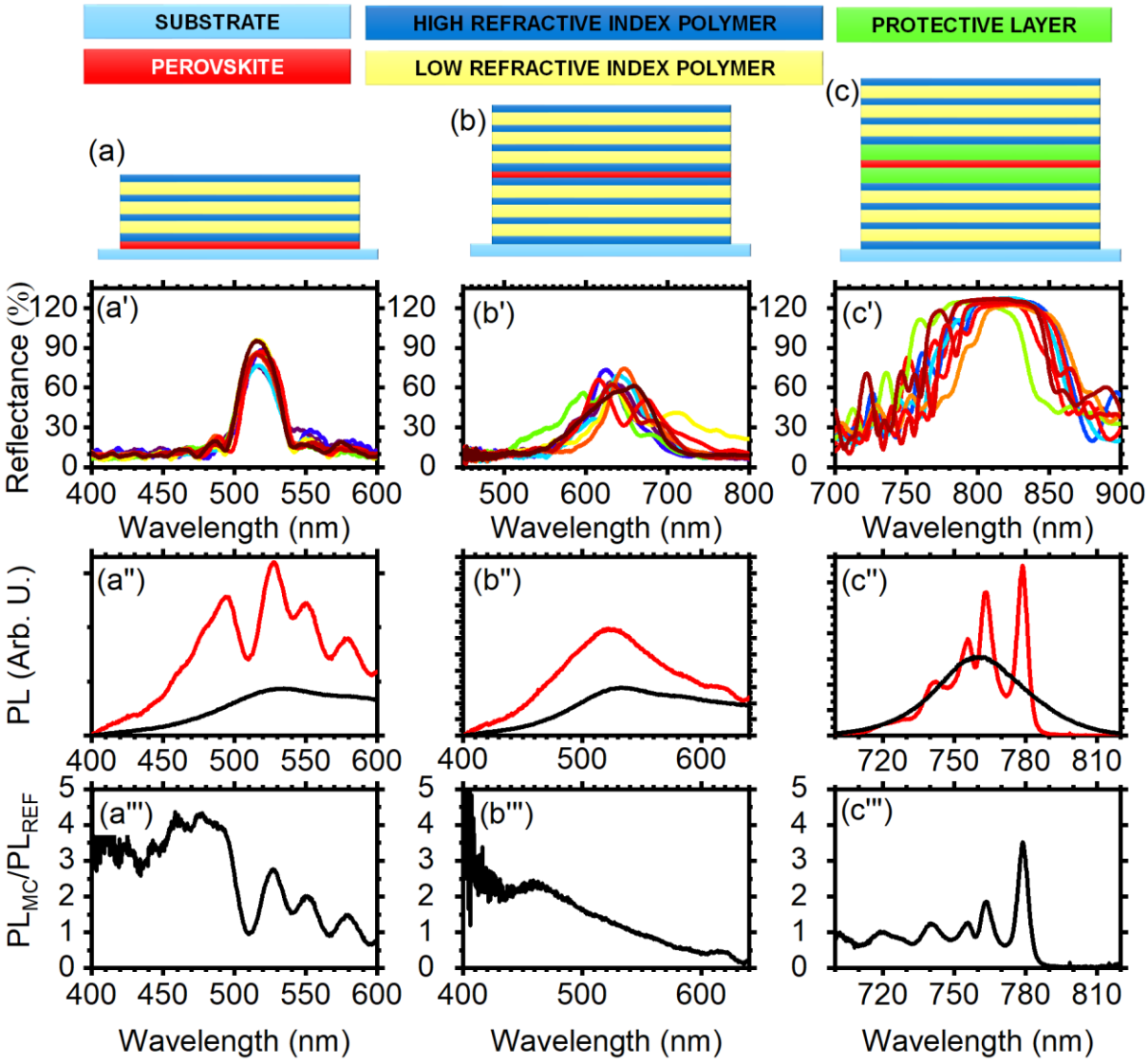

Figure 7.4:. Schematic (a, b, c) reflectance spectra (a', b', c') PL spectra of the photonic structure (red line) and of the reference film (black line) (a'', b'', c''), and ratio spectra calculated normalizing the photonic structure emission by the reference emission (a''', b''', c''') for the three architectures: (EDBE) $PbCl_4$ coupled with a DBR[19] (panels a) and with a full microcavity (panels b) and MA PbI_3 embedded in a microcavity employing a protective layer.[89]

When the same materials are employed to fabricate a microcavity where the perovskite constitute the defect layer (Figure 7.4 b), the deposition of the perovskite thin film from DMSO solution on the first half microcavity favour the polymer dissolution. Such phenomenon introduces defects, roughness and inhomogeneities within the structure. The reflectance spectra of Figure 7.4 b' show indeed lack of homogeneity, and low optical quality, as the interference pattern is barely visible. The PBG, positioned at about 640 nm is characterized by low reflectance intensity and appears broadened. Moreover, very broad cavity modes are detectable within this signal ($Q \approx 20$).[90] The large disorder induced by the deposition of the perovskite layer implies that the MC has only small effects on the perovskite emission. Comparing the emission spectra of Figure 7.4 b'', one notices that the emission intensity of the microcavity (red line) results larger with respect to the reference sample (black line) owing again to better light extraction, but emission reshaping induced is barely detectable. Indeed, only a broad relative maximum is visible at about 640 nm. As mentioned previously, polymer MCs with structure similar to the one just reported show quality factor up to 250.[3] The low quality of this systems can then be attributed to the incompatibility of the polymer thin films with DMSO-perovskite deposition.

Employing a protective perfluorinated polymer layer for the DBR during the perovskite deposition allows more homogeneous samples and larger finesse (See schematic in Figure 7.4 c). In this case high surface tension perfluorinated polymers with low wettability protects the commercial polymers and avoid their dissolution.[89] On the other hand, such low wettability implies a surface activation process to deposit the perovskite thin film on the protective layer, complicating the fabrication process.[89] The spectra of Figure 7.4 c' show the reflectance spectra collected on different part of the sample surface for a MC made of CA and PVK where the cavity layer is made of $MAPbI_3$ casted from DMSO solution over a protecting layer. The sample is very homogenous and present better optical quality with respect to the microcavity fabricated without protective layer. All the spectra show a relatively broad PBG peaked at about 810 nm. The intensity of the reflected light in this case is larger than 100% due to larger reflectivity than the reference aluminium mirror. The peak shows a cavity mode positioned on its short wavelength side, that induces major variations in the perovskite emission. The MA PbI_3 luminescence ranges from 710 nm and 820 nm and is peaked at 760 nm (Figure 7.4c'''). When coupled with the microcavity it results strongly modulated and a cavity mode is detected

at 780 nm (Figure 7.4 c"'). Such feature is sharp and corresponds to a finesse of 105, which is the best reported for polymer microcavities containing perovskites thin films.[89]

These data show that the DMSO is an issue for the implementation of perovskites in polymer structure, this solvent can indeed dissolve polymers with both polar and non-polar characters, affecting the homogeneity and in turn the performances of the photonic structure. On the other hand, the possibility to fabricate device for single color enhancement or suppression and for lasing by a start-to-end solution processing is highly interesting for the simplification of fabrication processes and for cost reduction. The data reported in this work, demonstrates that employing specialty polymers as protective coating it is possible to obtain photonic structure able to modify the emission successfully. On the other hand, these materials require processes of surface activation that make the growth of the structure more complex.

7.2.2 Molecular Emitters: J-aggregates

Since the discovery of J-aggregates in the '30s,[91-92] several synthetic and natural dye aggregates have been researched.[93-99] Thanks to outstanding photoemitting properties,[100] that include superradiance,[101] high absorbance, and sharp emission.[102-103] J-aggregates entered in the spotlight for applications in antifraud systems,[104] and biological imaging[105-106] and for optoelectronic devices such as light emitting diodes,[33, 107] lasers,[108-109] optical switches,[108-109] colorimetric sensors,[110-111] and for the achievement of strong-coupling effects.[112-115] Among these dyes, perylene bisimides (PBIs, in red in Figure 7.5) display exceptional photo-chemical stability against photo-oxidation,[102-103, 116-118] high absorption coefficients, inefficient triplet formation and photoluminescence quantum yields (*QY*s) close to unity in molecular solutions,[119-120] Thanks to the unique aggregate robustness, these new PBIs attracted interest for the integration into polymer matrices. Inducing J-aggregation into polymer solutions aiming at processable materials promises indeed the integration of solid-state active media into plastic photonic devices such as in lasing microcavity. On the other hand, PBI J-aggregates were never implemented into polymer matrices and structures,[121-123] while only few bare PBI J-aggregate solid state films have been reported so far.[119, 124-126] Polymeric MCs represent then viable media to achieve plastic devices based on PBI J-aggregates. For this study, a new PBI bearing 2-ethylhexyl-substituted gallic acid residues at para-positions of the phenoxy-functionalized PBI (named PEH-PBI, Figure 7.5) has been developed by the research Group of Prof. Würthner, of the University of . Wurzburg. PEH-PBI J-aggregates only form in low-polarity

environments, where hydrogen bonds are sufficiently strong. Then, to embed these J-aggregate fibers into a polymer matrix, the monomeric PEH-PBI was dispersed into a solution of amorphous polypropylene (aPP) and *n*-hexane. The aPP matrix prevented the washout of the dye during the deposition of the subsequent microcavity layers, and allows smooth surfaces typical of spun-cast polymers and nanocomposite films.[127-128]

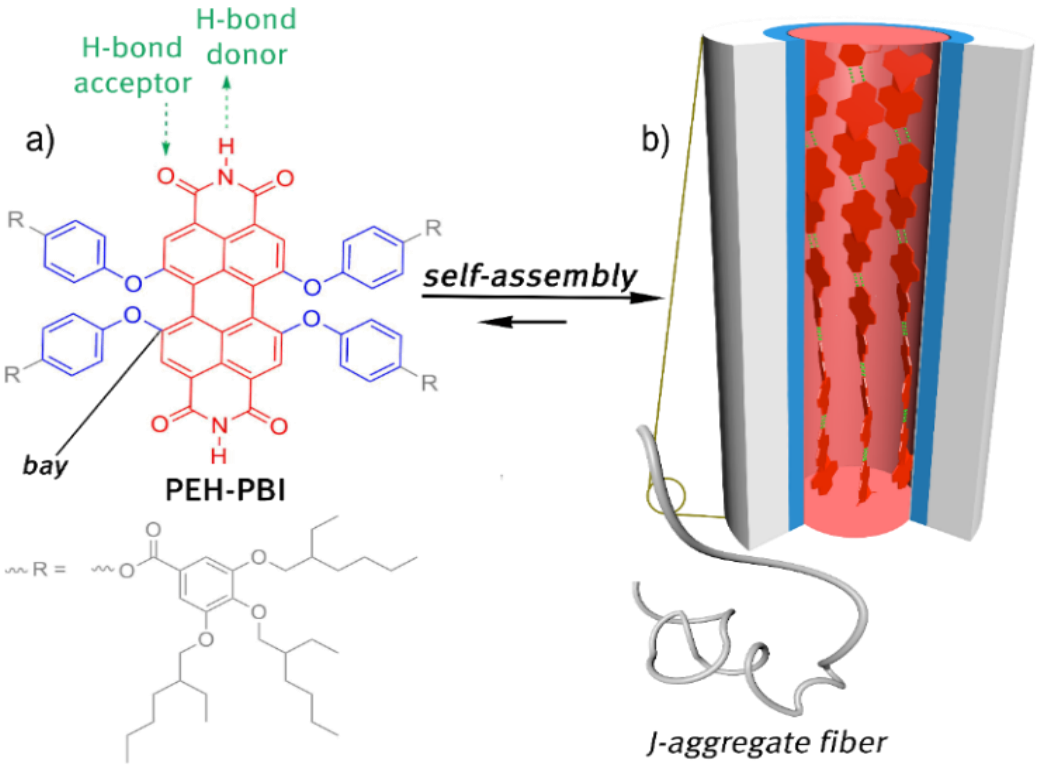

Figure 7.5: a) Chemical structure of PEH-PBI monomer and b) the hydrogen bond directed J-type aggregate Hydrogen bonds, displayed in green, direct the formation of the triple-stranded J-aggregate.

Figure 7.6 a and b compare the transmittance and fluorescence spectra of the obtained microcavity where the PEH PBI:aPP blend was inserted between two DBRs made of polyacrylic acid (PAA) and PVK. The cavity observed at ~725 nm strongly affects the PEH-PBI fluorescence. The PL spectrum of the bare blend ranges from ~ 625 to 800 nm with maximum intensity at 659 nm. In the MCs, its intensity is suppressed at the PBG wavelengths (Figure 7.6 a and b), while it is strongly enhanced at the cavity mode wavelength. The interference pattern weakly modulates the emission. Because of the angular dispersion of the

PBG and of the cavity mode (See Appendix A.2), the enhanced peak shifts toward smaller wavelength increasing the collection angle (Figure 7.6 c), demonstrating that the variations in the J-aggregate emission profile are correlated to the photonic structure. The microcavity Q-factor approaches 110.[129]

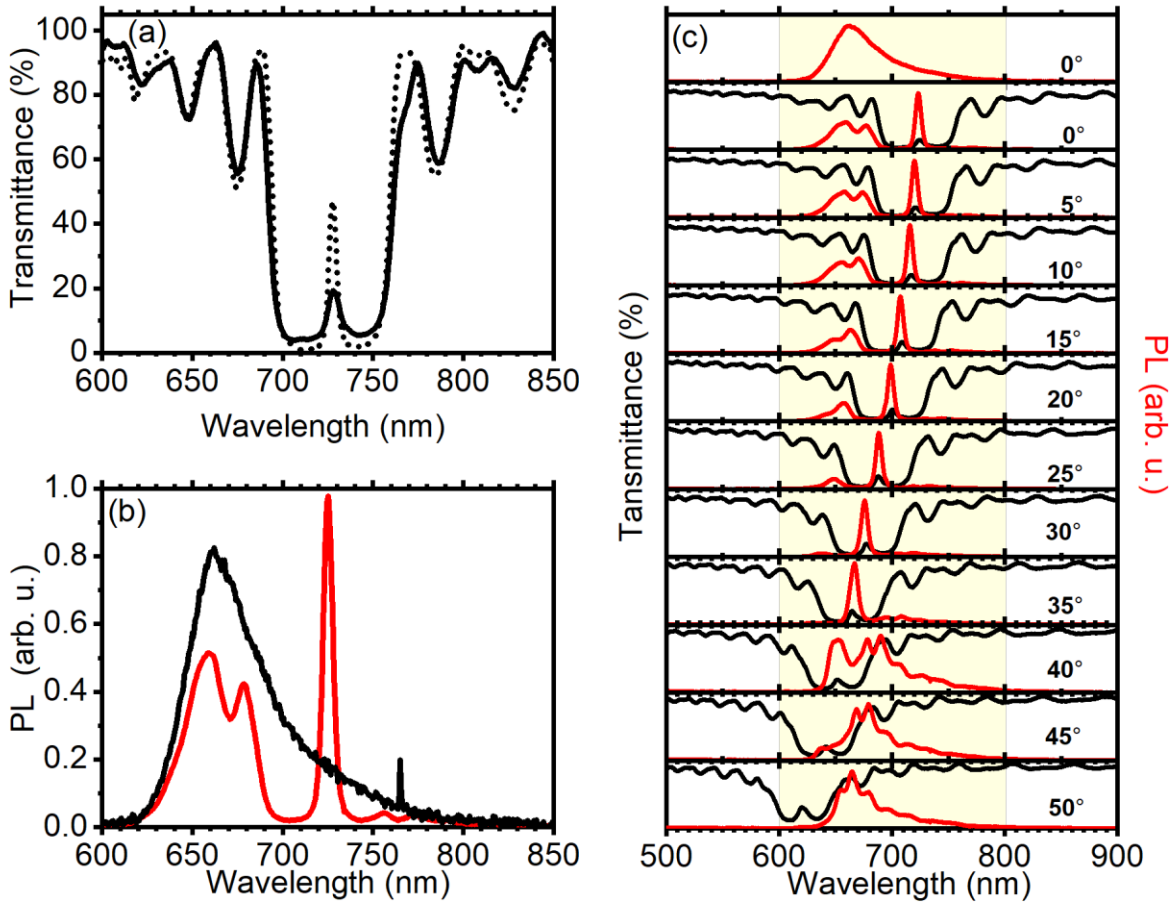

Figure 7.6: a) Calculated (dashed lines) and experimental (continuous lines) transmittance spectra of PEH-PBI MC. b) *PL* spectra of reference (black line) and microcavity (red line). c) Angular dispersion of the microcavity transmittance and fluorescence spectra.

Summarizing, PEH-PBI J-aggregates can be efficiently transferred from solutions to amorphous polypropylene matrix and used as photoactive material in all-polymer microcavities. The cavity provides a strong and directional spectral redistribution of PEH-PBI J-aggregate fluorescence due to the modified density of photonic states. Analyses of the enhancement factors, the photoluminescence decay and the quantum yields (Data not shown here, see Ref. [8]) show that the microcavity growth process does not introduce non-radiative *PL* de-excitation pathway, being the measured *QY* limited by light extraction issues, only. In order

to achieve a full radiative rate enhancement, higher *PL QY* materials and higher dielectric contrast processable polymers must be developed.

7.2.3 Inorganic Emitters: Core-Shell CdS-CdSe Dot in Rods Nanocrystals

Colloidal nanocrystals attracted considerable attention in the field of light emitting devices thanks to their high fluorescence QY and spectral tunability via electronic structure engineering, and surface functionalization. Indeed, their composition and shape can be adjusted to obtain materials with tailored and stable electronic properties.[130] Nanocrystals of different shapes such as CdSe nanoplatelets[131] and core-shell architectures as CdSe/CdS dot-in-rods[132] or giant-shells[133-134] have been used in several light-emitting applications,[135-139] including lasers.[140-146] Surface functionalization improves passivation and reduces PL quenching defects, [147-151] while allowing *solubility* in many organic and polar solvents including water,[152-156] and promoting self-organization and preparation of nanocomposites for solid state photonic devices.[157-165] In this part of the project, high quality, polymer planar MCs embedding CdSe/CdS dot-in-rods (DiRs) in the cavity layer were fabricated and investigated, (Figure 7.7 a and b). The DiRs were provided by Dr Francesco di Stasio from the Italian Institute of Technology of Genova. To embed DiRs in high optical quality all-polymer MCs, the DiRs were dispersed into a polystyrene matrix (DiRs:PS). The composite was then embedded into a PVK:CA MC.

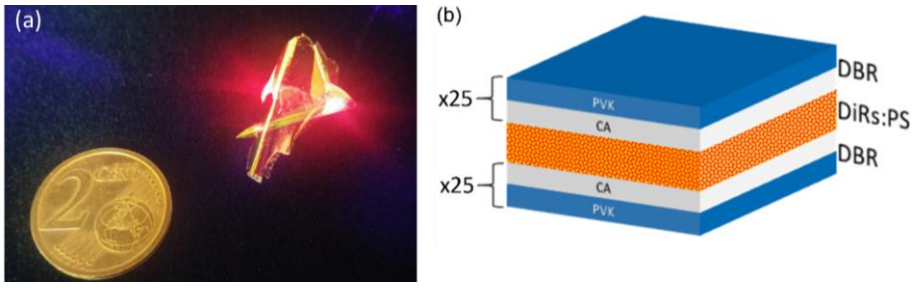

Figure 7.7: (a) Freestanding rolled-up microcavity under violet laser excitation where the bright DiRs red fluorescence is observed. (b) Scheme of the planar microcavity.

Figure 7.8 shows the transmittance spectrum of the MCs having an intense and broad peak between 580 and 646 nm assigned to the photonic band gap. Within the PBG, a sharp minimum at 613 nm is assigned to the cavity mode. Figure 7.8 b highlights the spectral re-shaping

induced by the microcavity on the PL of DiRs:PS nanocomposite with respect to the reference film recorded under the very same experimental conditions. The MCs induces a 10 folds sharpening of the PL spectrum, whose FWHM changes from 24 nm for the reference to 2.4 nm. In addition, for the microcavity, PL peak intensity is ~5 times larger than for the reference. The microcavity quality factor approaches 255, that is the largest so far reported for planar all-polymer microcavities.[157, 166-170] Figure 7.8 c shows the PL spectra of the microcavity collected at angles between 0 and 32°. The cavity emission shifts towards higher energy increasing the detection angle, according to the PBG dispersion (Appendix A).

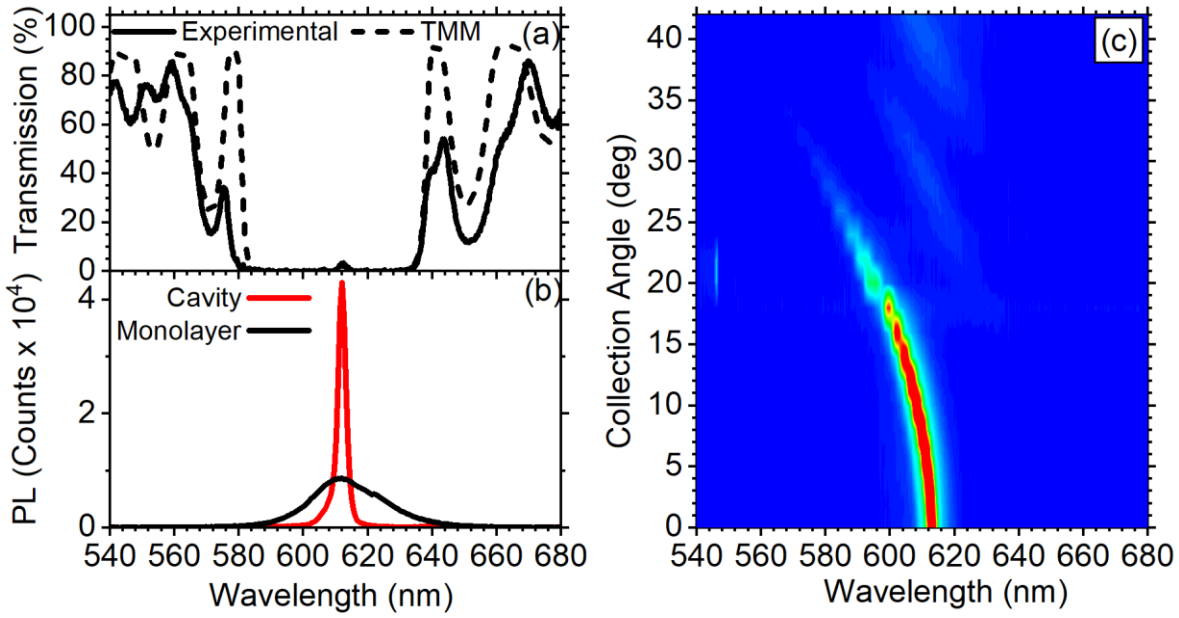

Figure 7.8 (a) Experimental (continuous line) and calculated (dashed line) microcavity transmission spectra. (b) PL spectra for a microcavity (in red) and for a reference sample (in black) recorded in the very same conditions. (c) Contour plot of the microcavity fluorescence spectra as a function of the collection angle.

This work demonstrates solution-based bottom-up fabrication of all-polymer planar microcavities embedding CdSe/CdS DiRs nanocrystals as fluorescent medium. DiRs are dispersed in a polystyrene matrix to obtain a highly process able nanocomposite. Optical investigation of the microcavity shows a 10-fold sharpening and a 5-time increase of the emission at the cavity mode wavelength, while the overall number of emitted photons is reduced.

7.3 Polymer Planar Microcavities For Lasing

The wide use of integrated lasers in electronic devices pushes the development of simple and cost-effective fabrication for low power sources.[171-173] Vertical cavity surface emitting lasers (VCSEL)[174] are ideal candidates for this purpose.[175] VCSELs are a planar MCs formed by two dielectric mirrors embedding a gain medium opportunely structured to provide lateral confinement.[176] Due to its conceptual simplicity, this kind of structure is easy to fabricate and applies to many technological fields, including fiber communication systems, optical disk reading, laser printers, and sensing.[177-181] The main drawback of these systems is the need for expensive and time consuming epitaxial growth to obtain high quality VCSELs based on crystalline emitters.[174, 182-183] However, pursuing simplicity and cost reduction, solution processing is arising increasing interest.[184] The previous Paragraph, reported on the fabrication of hybrid microcavities made of polymers doped with CdSe/CdS dot-in-rods (DiRs).[9] Employing a similar structure, but increasing the NCs density it is possible to achieve a low lasing threshold. In detail, a dense solution of DiRs was drop-cast on a polymer DBR to realize a several microns thick and compact nanocrystal film. The second DBR was fabricated separately and then pressed it on top of the first one to obtain the resonator (Figure 7.9 a).

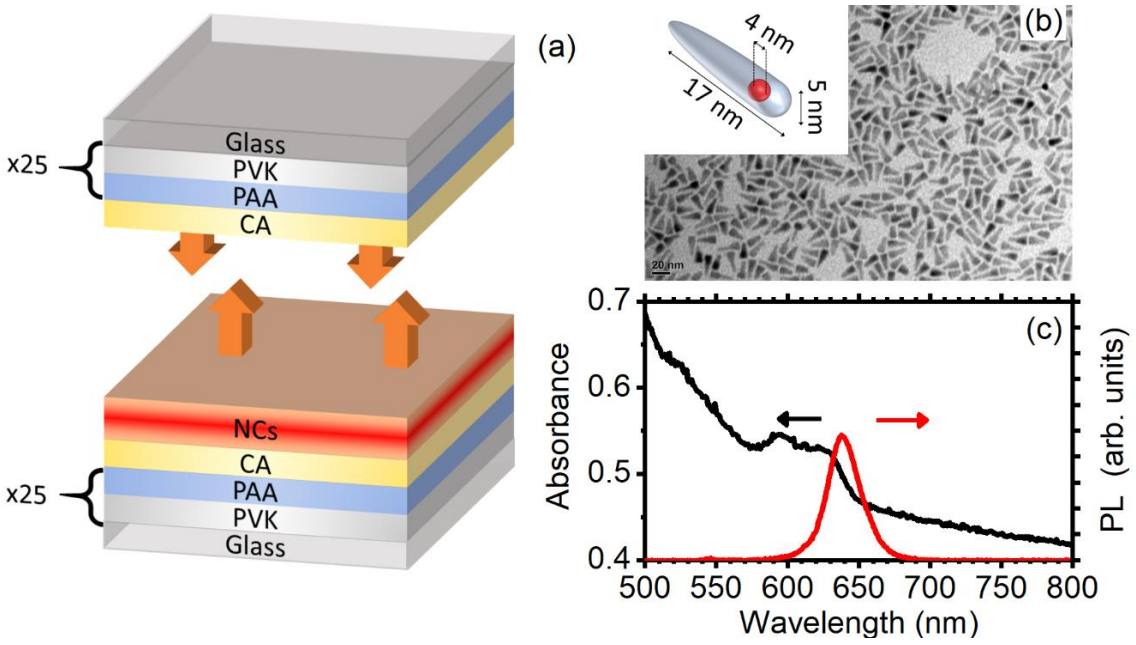

Figure 7.9: (a) Schematic of the MC structure; (b) TEM image of CdSe/Cds DiRs; in the inset, sketch of the DiR core-shell structure; (c) Absorbance (black) and CW PL (red) of the DiR film.

Figure 7.9 b shows a transmission electron microscopy (TEM) image of the DiRs used in this work. The DiRs have a tapered shape with average length of 17 ± 3 nm, and a mean base diameter of 5 ± 1 nm. Figure 7.9 c reports the absorbance (black) and continues wave (CW) PL (red) spectra of a drop-cast DiRs film. The background of the absorbance spectrum is characterized by light scattering induced by the rough film surface. In spite of that, the spectrum clearly shows two peaks at about 625 and 595 nm, which are assigned to transitions related to the CdSe cores.[132] The shoulder at ~520 nm originates instead from the CdS shell. The CW PL spectrum of the DiRs film displays a sharp peak[9] with FWHM of 27 nm centered at 639 nm.

The investigation of the fluorescence properties under fs-excitation for different pumping fluences clearly shows lasing action. Figure 7.10 a reports the bare spectra in light colors filled to the base. These spectra show a complex structure consisting in a broad component, similar to the one observed under CW pumping, and some sharper peaks between 630 nm and 645 nm. To appreciate these features, we deconvoluted all the spectra into two components. A first *broad* corresponding to the sample PL and a second *structured* component consists of the ASE band detected in the spectra of the reference sample (Data not shown here, see Ref. [24]). For low pumping fluences (<55 μJ/cm^2), a broad signal consisting of many peaks is observed. At a fluence of 55 μJ/cm^2 three very sharp peaks arise at 635 nm, 637 nm, and 640 nm. Upon further increasing of the pumping fluence to 110 μJ/cm^2, the intensity of the peak at 640 nm grows and dominates the spectrum. The FWHM of this peak is ~1 nm (resolution limited), which is 6-fold sharper than the ASE signal and 24-times sharper than the CW PL (Figure 7.9). In the spectra in Figure 7.10 a we also notice a clear variation of the line-shape of this sharp peak with increasing pumping fluence. Such behavior cannot be explained by the spectral redistribution induced by cavity modes, which, as well-known, preserves the line-shape.[9, 167, 185-187] Therefore, we conclude that the sharp peaks in the spectra originate from lasing.

To provide further evidence of lasing action, Figure 7.10 b shows the emission of the microcavity collected at normal incidence and slightly off-axis (angle < 10°) measured at a pumping fluence of 110 μJ/cm^2 together with the ASE spectrum of the reference sample recorded at a pumping fluence of 460 μJ/cm^2. The sharp peak at 640 nm is visible for collection under normal incidence (red line in Figure 7.10 b) and falls well inside the ASE emission band (green line in Figure 7.10 b). However, it is not detectable off-axis. This strong angular dependence is in excellent agreement with lasing from a DBR microcavity, while from spectral redistribution only a slight shift of the peak within such angles would be expected.[9, 167] Last,

Figure 7.10 c displays the intensity collected at 640 nm, assigned to the lasing mode, and at 660 nm, assigned to the PL, for increasing pumping fluence. As expected for lasing modes, the intensity of the sharp peak rises faster than the signal assigned to the PL.

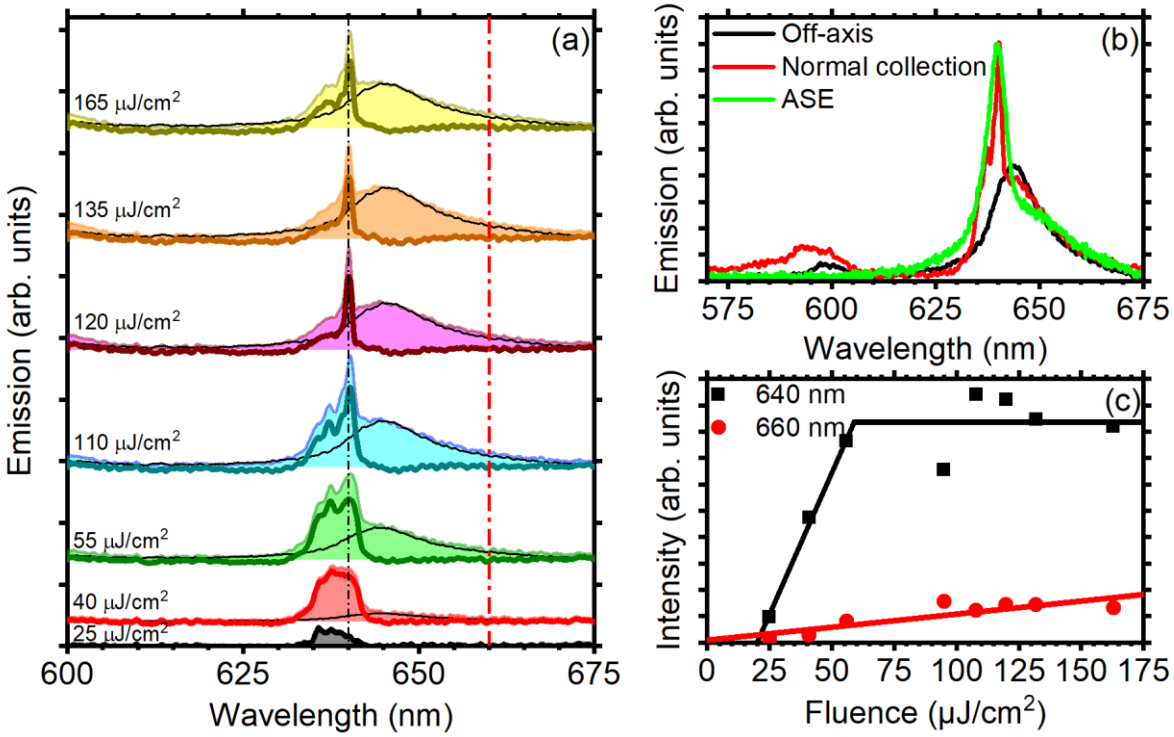

Figure 7.10 (a) Stacked fs emission spectra of the MC collected at normal incidence for different pumping fluences. The original emission spectra are shown in filled light colors; the deconvoluted PL component as a black line; and the deconvoluted component with the lasing peaks as dark thick line. (b) Microcavity emission spectra under fs pumping at 110 μJ/cm^2 collected at normal angle from the sample (red) and off-axis (black). Reference sample emission spectra showing ASE (in green) (c) Emission intensity at 640 nm (black squares) and 660 nm (red circles) against the pump fluence.

To summarize, the small linewidth, the intensity versus pumping fluence, the spectral position, and the strong angular dependence of the sharp peaks in the microcavity spectra allows us to assign them to lasing.

7.4 Outcomes

This part of the work aimed to demonstrates the feasibility of polymer microcavities embedding different emitters. It demonstrates that trough proper processing polymer microcavities can

embed a very large variety of materials including molecules, inorganic nanocrystals and even perovskites. For all the systems investigated we recorded emission intensity enhancement, spectral redistribution and angular dependence. On the other hand, investigations of emission rate enhancement (data not shown here) demonstrates that strong effects are still unreliable with polymer microcavities due to the low dielectric contrast between their building blocks. Nevertheless, this work demonstrates that it is possible to achieve emission reshaping and lasing action also from not-polymeric emitters. These results, considering the advantages related to polymer that have been mentioned many times in this manuscript, are promising for the development of polymer all-solution processable lightening devices with controllable emission and lasing.

References

(1) Malvezzi, A. M.; Cattaneo, F.; Vecchi, G.; Falasconi, M.; Guizzetti, G.; Andreani, L. C.; Romanato, F.; Businaro, L.; Fabrizio, E. D.; Passaseo, A.; Vittorio, M. D., *J. Opt. Soc. Am. B*, **2002**, 19, 2122.

(2) MacDougal, M. H.; Dapkus, P. D.; Pudikov, V.; Hanmin, Z.; Gye Mo, Y., *IEEE Photonics Technol. Lett.*, **1995**, 7, 229-231.

(3) Lova, P.; Manfredi, G.; Comoretto, D., *Adv. Opt. Mater.*, **2018**, 6, 1800730-26.

(4) Laussy, F. P., *Microcavities*. Oxford University Press: New York, 2017.

(5) Joannopoulos, J. D.; Johnson, S. G.; Winn, J. N.; Meade, R. D., *Photonic crystals: molding the flow of light*. Princeton university press: Woodstock, 2011.

(6) Frezza, L.; Patrini, M.; Liscidini, M.; Comoretto, D., *J. Phys. Chem. C*, **2011**, 115, 19939 - 19946.

(7) Gazzo, S.; Manfredi, G.; Pötzsch, R.; Wei, Q.; Alloisio, M.; Voit, B.; Comoretto, D., *J. Polym. Sci., Part B: Polym. Phys.*, **2016**, 54, 73-80.

(8) Lova, P.; Grande, V.; Manfredi, G.; Patrin, M.; Herbst, S.; Würthner, F.; Comoretto, D., *Adv. Opt. Mater.*, **2017**, 5, 1700523.

(9) Manfredi, G.; Lova, P.; Di Stasio, F.; Krahne, R.; Comoretto, D., *ACS Photonics*, **2017**, 4, 1761–1769.

(10) Canazza, G.; Scotognella, F.; Lanzani, G.; De Silvestri, S.; Zavelani-Rossi, M.; Comoretto, D., *Laser Phys. Lett.*, **2014**, 11, 035804

(11) Chen, S.; Zhang, C.; Lee, J.; Han, J.; Nurmikko, A., *Adv. Mater.*, **2017**, 29, 1604781.

(12) Christmann, G.; Simeonov, D.; Butté, R.; Feltin, E.; Carlin, J.-F.; Grandjean, N., *Appl. Phys. Lett.*, **2006**, 89, 261101.

(13) Mizuno, H.; Tanijiri, N.; Kawanishi, Y.; Ishizumi, A.; Yanagi, H.; Hiromitsu, I., *Mater. Lett.*, **2016**, 168, 210-213.

(14) Hobson, P. A.; Barnes, W. L.; Lidzey, D. G.; Gehring, G. A.; Whittaker, D. M.; Skolnick, M. S.; Walker, S., *Appl. Phys. Lett.*, **2002**, 81, 3519-3521.

(15) Scotognella, F.; Monguzzi, A.; Cucini, M.; Meinardi, F.; Comoretto, D.; Tubino, R., *Int. J. Photoenergy*, **2008**, 2008, 1-4.

(16) Knarr III, R. J.; Manfredi, G.; Martinelli, E.; Pannocchia, M.; Repetto, D.; Mennucci, C.; Solano, I.; Canepa, M.; Buatier de Mongeot, F.; Galli, G.; Comoretto, D., *Polymer*, **2016**, 84, 383-390.

(17) Fornasari, L.; Floris, F.; Patrini, M.; Comoretto, D.; Marabelli, F., *Phys. Chem. Chem. Phys.*, **2016**, 18, 14086-14093.

(18) Manfredi, G.; Mayrhofer, C.; Kothleitner, G.; Schennach, R.; Comoretto, D., *Cellulose*, **2016**, 23, 2853-2862.

(19) Lova, P.; Cortecchia, D.; S. Krishnamoorthy, H. N.; Giusto, P.; Bastianini, C.; Bruno, A.; Comoretto, D.; Soci, C., *ACS Photonics*, **2018**, 5, 867-874.

(20) Vijisha, M. V.; Sini, V. V.; Siji Narendran, N. K.; Chandrasekharan, K., *Phys. Chem. Chem. Phys.*, **2017**, 19, 29641-29646.

(21) Katouf, R.; Komikado, T.; Itoh, M.; Yatagai, T.; Umegaki, S., *Photonics Nanostructures: Fundam. Appl.*, **2005**, 3, 116-119.

(22) Russo, M.; Campoy-Quiles, M.; Lacharmoise, P.; Ferenczi, T. A. M.; Garriga, M.; Caseri, W. R.; Stingelin, N., *J. Polym. Sci., Part B: Polym. Phys.* , **2012**, 50, 65-74.

(23) Yagi, R.; Katae, H.; Kuwahara, Y.; Kim, S.-N.; Ogata, T.; Kurihara, S., *Polymer*, **2014**, 55, 1120-1127.

(24) Manfredi, G.; Lova, P.; Di Stasio, F.; Rastogi, P.; Krahne, R.; Comoretto, D., *RSC Advances*, **2018**, 8, 13026-13033.

(25) Toccafondi, C.; Occhi, L.; Cavalleri, O.; Penco, A.; Castagna, R.; Bianco, A.; Bertarelli, C.; Comoretto, D.; Canepa, M., *J. Mater. Chem. C*, **2014**, 2, 4692-4698.

(26) Valappil, N. V.; Luberto, M.; Menon, V. M.; Zeylikovich, I.; Gayen, T. K.; Franco, J.; Das, B. B.; Alfano, R. R., *Photonics Nanostructures: Fundam. Appl.*, **2007**, 5, 184-188.

(27) Menon, V. M.; Luberto, M.; Valappil, N. V.; Chatterjee, S., *Opt. Express*, **2008**, 16,

19535-19540**.**

(28) Goldenberg, L. M.; Lisinetskii, V.; Schrader, S., *Laser Phys. Lett.***, 2013**, 10, 055808**.**

(29) Goldenberg, L. M.; Lisinetskii, V.; Schrader, S., *Appl. Phys. B***, 2015**, 120, 271-277**.**

(30) Bellingeri, M.; Chiasera, A.; Kriegel, I.; Scotognella, F., *Opt. Mater.***, 2017**, 72, 403-421**.**

(31) Skorobogatiy, M.; Yang, J., *Fundamentals of photonic crystal guiding*. Cambridge University Press: Cambridge, 2009.

(32) Savona, V.; Andreani, L. C.; Schwendimann, P.; Quattropani, A., *Solid State Commun.***, 1995**, 93, 733-739**.**

(33) Tischler, J. R.; Bradley, M. S.; Bulovic, V.; Song, J. H.; Nurmikko, A., *Phys. Rev. Lett.***, 2005**, 95, 036401**.**

(34) Sumioka, K.; Nagahama, H.; Tsutsui, T., *Appl. Phys. Lett.***, 2001**, 78, 3**.**

(35) Schouwinka, P.; Berlepschb, H. v.; Dahnec, L.; Mahrt, R. F., *Chem. Phys.***, 2002**, 285, 113**.**

(36) Liscidini, M.; Andreani, L. C., Photonic crystals: An introductory survey. In *Organic and hybrid photonic crystals*, Comoretto, D., Ed. Springer International Publishing: Cham, 2015; pp 3-29.

(37) Bajoni, D. Optical spectroscopy of photonic crystals and microcavities. PhD thesis, Università di Pavia, 2003.

(38) Skolnick, M. S.; Fisher, T. A.; Whittaker, D. M., *Semicond. Sci. Technol.***, 1998**, 13, 645**.**

(39) Oulton, R. F.; Takada, N.; Koe, J.; Stavrinou, P. N.; Bradley, D. D. C., *Semicond. Sci. Technol.***, 2003**, 18, S419**.**

(40) Kimble, H. J., *Nature***, 2008**, 453, 1023**.**

(41) Novotny, L., *Am. J. Phys.***, 2010**, 78, 1199-1202**.**

(42) Björk, G., *IEEE J. Quant. Electron.***, 1994**, 30, 2314-2318**.**

(43) Schubert, E. F.; Hunt, N. E. J.; Micovic, M.; Malik, R. J.; Sivco, D. L.; Cho, A. Y.; Zydzik, G. J., *Science***, 1994**, 265, 943-945**.**

(44) Björk, G.; Machida, S.; Yamamoto, Y.; Igeta, K., *Phys. Rev. A***, 1991**, 44, 669-681**.**

(45) Barth, M.; Gruber, A.; Cichos, F., *Phys. Rev. B***, 2005**, 72**.**

(46) Berti, L.; Cucini, M.; Di Stasio, F.; Comoretto, D.; Galli, M.; Marabelli, F.; Manfredi, N.; Marinzi, C.; Abbotto, A., *J. Phys. Chem. C***, 2010**, 114, 2403-2413**.**

(47) Lidzey, D. G.; Coles, D. M., Strong coupling in organic and hybrid-semiconductor microcavity structures. In *Organic and hybrid photonic crystals*, Comoretto, D., Ed.

Springer: Cham, 2015; pp 243-273.

(48) Hu, Y.; Lin, J.; Song, L.; Lu, Q.; Zhu, W.; Liu, X., *Sci. Rep.*, **2016**, 6, 23210.

(49) Di Stasio, F.; Berti, L.; McDonnell, S. O.; Robbiano, V.; Anderson, H. L.; Comoretto, D.; Cacialli, F., *APL Mater.*, **2013**, 1, -.

(50) Vos, W. L.; Sprik, R.; Lagendijk, A.; Wegdam, G. H.; Blaaderen, A. v.; Imhof, A., *Photonic band gap materials*. Kluwer Academic Publishers Dordrecht Netherlands: Dordrecht, 1996.

(51) Virgili, T.; Lidzey, D. G.; Grell, M.; Walker, S.; Asimakis, A.; Bradley, D. D. C., *Chem. Phys. Lett.*, **2001**, 341, 219-224.

(52) Hopmeier, M.; Guss, W.; Deussen, M.; Göbel, E. O.; Mahrt, R. F., *Phys. Rev. Lett.*, **1999**, 82, 4118-4121.

(53) Gerard, J. M.; Gayral, B., *J. Lightwave Technol.*, **1999**, 17, 2089-2095.

(54) Yokoyama, H.; Nishi, K.; Anan, T.; Nambu, Y.; Brorson, S.; Ippen, E.; Suzuki, M., *Opt. Quantum Electron.*, **1992**, 24, S245-S272.

(55) McKenzie, J.; Zoorob, T. L. Inverted-pyramidal photonic crystal light emitting device. Filing Date 28 November 2006.

(56) Svelto, O., *Principles of lasers*. 4th Edition ed.; Springer Science + Business Media, Inc.: New York, 1998.

(57) Dowling, J. P.; Scalora, M.; Bloemer, M. J.; Bowden, C. M., *J. Appl. Phys.*, **1994**, 75, 1896-1899.

(58) Moses, D., *Appl. Phys. Lett.*, **1992**, 60, 3215-3216.

(59) Hide, F.; Díaz-García, M. A.; Schwartz, B. J.; Andersson, M. R.; Pei, Q.; Heeger, A. J., *Science*, **1996**, 273, 1833-1836.

(60) Samuel, I. D. W.; Namdas, E. B.; Turnbull, G. A., *Nat. Photon.*, **2009**, 3, 546-549.

(61) Karl, M.; Glackin, J. M. E.; Schubert, M.; Kronenberg, N. M.; Turnbull, G. A.; Samuel, I. D. W.; Gather, M. C., *Nat. Comm.*, **2018**, 9, 1525.

(62) Tessler, N.; Denton, G. J.; Friend, R. H., *Nature*, **1996**, 382, 695-697.

(63) Persano, L.; Carro, P. D.; Mele, E.; Cingolani, R.; Pisignano, D.; Zavelani-Rossi, M.; Longhi, S.; Lanzani, G., *Appl. Phys. Lett.*, **2006**, 88, 121110.

(64) Christian, K.; Martin, H.; Andreas, H.; Martin, P.; Wolfgang, S.; Uli, L.; Jochen, F.; Ullrich, S.; Klaus, M.; Andreas, G.; Volker, W., *Adv. Mater.*, **1998**, 10, 920-923.

(65) Gaal, M.; Gadermaier, C.; Plank, H.; Moderegger, E.; Pogantsch, A.; Leising, G.; List,

E. J. W., *Adv. Mater.*, **2003**, 15, 1165-1167.

(66) Lova, P.; Soci, C., Nanoimprint Lithography: Toward Polymer Photonic Crystals. In *Organic and Hybrid Photonic Crystals*, 1st ed.; Comoretto, D., Ed. Springer: Cham, 2015; Vol. 1, p 493.

(67) Clark, J.; Lanzani, G., *Nat. Photon.*, **2010**, 4, 438-446.

(68) Sébastien, C.; Sébastien, F., *Polym. Int.*, **2012**, 61, 390-406.

(69) Samuel, I. D. W.; Turnbull, G. A., *Chem. Rev.*, **2007**, 107, 1272-1295.

(70) Grivas, C.; Pollnau, M., *Laser Photonic Rev.*, **2012**, 6, 419-462.

(71) Johannes, H.; Yue, W.; D., M. J. J.; Zheng, G.; David, M.; Benoit, G.; Georgios, T.; A., T. G.; W., S. I. D.; Nicolas, L.; Erdan, G.; D., D. M., *Laser Photonic Rev.*, **2013**, 7, 1065-1078.

(72) Polson, R. C.; Vardeny, Z. V.; Chinn, D. A., *Appl. Phys. Lett.*, **2002**, 81, 1561-1563.

(73) Vardeny, Z. V., *Nature*, **2002**, 416, 489.

(74) Polson, R.; Chipouline, A.; Vardeny, Z., *Adv. Mater.*, **2001**, 13, 760-764.

(75) Shkunov, M. N.; Vardeny, Z. V.; DeLong, M. C.; Polson, R. C.; Zakhidov, A. A.; Baughman, R. H., *Adv. Func. Mater.*, **2002**, 12, 21.

(76) Deschler, F.; Price, M.; Pathak, S.; Klintberg, L. E.; Jarausch, D.-D.; Higler, R.; Hüttner, S.; Leijtens, T.; Stranks, S. D.; Snaith, H. J.; Atatüre, M.; Phillips, R. T.; Friend, R. H., *J. Phys. Chem. Lett.*, **2014**, 5, 1421-1426.

(77) Cho, H.; Jeong, S.-H.; Park, M.-H.; Kim, Y.-H.; Wolf, C.; Lee, C.-L.; Heo, J. H.; Sadhanala, A.; Myoung, N.; Yoo, S.; Im, S. H.; Friend, R. H.; Lee, T.-W., *Science*, **2015**, 350, 1222-1225.

(78) Cortecchia, D.; Mróz, W.; Neutzner, S.; Borzda, T.; Folpini, G.; Brescia, R.; Petrozza, A., *Chem.*, **2019**, 5, 2146-2158.

(79) Saliba, M.; Correa-Baena, J.-P.; Grätzel, M.; Hagfeldt, A.; Abate, A., *Angew. Chem. Int. Ed.*, **2018**, 57, 2554-2569.

(80) Cortecchia, D.; Neutzner, S.; Yin, J.; Salim, T.; Srimath Kandada, A. R.; Bruno, A.; Lam, Y. M.; Martí-Rujas, J.; Petrozza, A.; Soci, C., *APL Materials*, **2018**, 6, 114207.

(81) Park, H. J.; Xu, T.; Lee, J. Y.; Ledbetter, A.; Guo, L. J., *ACS Nano*, **2011**, 5, 7055-7060.

(82) Cortecchia, D.; Yin, J.; Bruno, A.; Lo, S.-Z. A.; Gurzadyan, G. G.; Mhaisalkar, S.; Bredas, J.-L.; Soci, C., *J. Mater. Chem. C*, **2017**, 5, 2771-2780.

(83) Dohner, E. R.; Jaffe, A.; Bradshaw, L. R.; Karunadasa, H. I., *J. Am. Chem. Soc.*, **2014**,

136, 13154-13157**.**

(84) Dou, L.; Wong, A. B.; Yu, Y.; Lai, M.; Kornienko, N.; Eaton, S. W.; Fu, A.; Bischak, C. G.; Ma, J.; Ding, T.; Ginsberg, N. S.; Wang, L.-W.; Alivisatos, A. P.; Yang, P., *Science***,** **2015**, 349, 1518-1521**.**

(85) Yin, J.; Li, H.; Cortecchia, D.; Soci, C.; Brédas, J.-L., *ACS Energy Lett.***,** **2017**, 2, 417-423**.**

(86) Cortecchia, D.; Neutzner, S.; Srimath Kandada, A. R.; Mosconi, E.; Meggiolaro, D.; De Angelis, F.; Soci, C.; Petrozza, A., *J. Am. Chem. Soc.***,** **2017**, 139, 39-42**.**

(87) Cortecchia, D.; Yin, J.; Petrozza, A.; Soci, C., *J. Mater. Chem. C***,** **2019**, 7, 4956-4969**.**

(88) Cortecchia, D.; Lew, K. C.; So, J.-K.; Bruno, A.; Soci, C., *Chem. Mater.***,** **2017**, 29, 10088-10094**.**

(89) Lova, P.; Giusto, P.; Di Stasio, F.; Manfredi, G.; Paternò, G. M.; Cortecchia, D.; Soci, C.; Comoretto, D., *Nanoscale***,** **2019**, 11, 8978-8983**.**

(90) Lova, P.; Cortecchia, D.; Soci, C.; Comoretto, D., *Appl. Sci.***,** **2019**, 9**.**

(91) Scheibe, G.; Kandler, L.; Ecker, H., *Naturwissenschafte***,** **1937**, 25-75**.**

(92) Jelley, E. E., *Nature***,** **1936**, 138, 1009-1010**.**

(93) Würthner, F.; Kaiser, T. E.; Saha-Möller, C. R., *Angew. Chem. Int. Ed.***,** **2011**, 50, 3376 – 3410**.**

(94) Moll, J.; Daehne, S., *J. Chem. Phys.***,** **1995**, 102, 6362-6370**.**

(95) Tani, T.; Saeki, M.; Yamaguchi, Y.; Hayashi, T.; Oda, M., *J. Lumin.***,** **2004**, 107, 339-346**.**

(96) Avdeeva, V. I.; Shapiro, B. I., *Chem. Mater.***,** **2003**, 389, 77**.**

(97) Berlepsch, H. V.; Bottcher, C.; Ouart, A.; Burger, C.; Dahne, S.; Kirstein, S., *J. Phys. Chem. B***,** **2000**, 104, 5255**.**

(98) George, J.; Wang, S.; Chervy, T.; Canaguier-Durand, A.; Schaeffer, G.; Lehn, J.-M.; Hutchison, J. A.; Genet, C.; Ebbesen, T. W., *Faraday Discuss.***,** **2015**, 178, 281-294**.**

(99) Collini, E.; Ferrante, C.; Bozio, R., *J. Phys. Chem. B***,** **2005**, 109, 2-5**.**

(100) Semion, S. K.; Eisfeld, A.; Valleau, S.; Aspuru-Guzik, A., *Nanophotonics***,** **2013**, 2, 21-38**.**

(101) Spano, F. C.; Mukamel, S., *J. Chem. Phys.***,** **1989**, 91, 683-700**.**

(102) Kobayashi, T., *J-aggregates*. World Scientific Publishing Co Pte Ltd: Singapore, 2012; Vol. 2.

(103) Kobayashi, T., *J-Aggregates*. World Scientific Publishing Co Pte Ltd: Singapore, 1996.

(104) Xue, C.; Xue, Y.; Dai, L.; Urbas, A.; Li, Q., *Adv. Opt. Mater.*, **2013**, 1, 581-587.

(105) Xue, C.; Birel, O.; Xue, Y.; Dai, L.; Urbas, A.; Li, Q., *J. Phys. Chem. C*, **2013**, 117, 6752-6758.

(106) Xue, C.; Birel, O.; Gao, M.; Zhang, S.; Dai, L.; Urbas, A.; Li, Q., *J. Phys. Chem. C*, **2012**, 116, 10396-10404.

(107) Stender, B.; Völker, S. F.; Lambert, C.; Pflaum, J., *Adv. Mater.*, **2013**, 25, 2943-2947.

(108) Özçelik, S.; Akins, D. L., *Appl. Phys. Lett.*, **1997**, 71, 3057-3059.

(109) Özçelik, S.; Özçelik, I.; Akins, D. L., *Appl. Phys. Lett.*, **1998**, 73, 1949-1951.

(110) Chen, C.; Wang, R.; Guo, L.; Fu, N.; Dong, H.; Yuan, Y., *Org. Lett.*, **2011**, 13, 1162-1165.

(111) Sloniec-Myszk, J.; Resch-Genger, U.; Hennig, A., *J. Phys. Chem. B*, **2016**, 120, 877-885.

(112) Eradat, N.; Sivachenko, A. Y.; Raikh, M. E.; Vardeny, Z. V.; Zakhidov, A. A.; Baughman, R. H., *Appl. Phys. Lett.*, **2002**, 80, 3491.

(113) Agranovich, V. M.; Litinskaia, M.; Lidzey, D. G., *Phys. Rev. B*, **2003**, 67, 085311.

(114) Fletcher, R. B.; Lidzey, D. G.; Bradley, D. D. C.; Bernius, M.; Walker, S., *Appl. Phys. Lett.*, **2000**, 77, 1262-1264.

(115) Pirotta, S.; Patrini, M.; Liscidini, M.; Galli, M.; Dacarro, G.; Canazza, G.; Guizzetti, G.; Comoretto, D.; Bajoni, D., *Appl. Phys. Lett.*, **2014**, 104, 4051111.

(116) Marabelli, F.; Comoretto, D.; Bajoni, D.; Galli, M.; Fornasari, L., *Mat. Res. Soc. Symp. Proc.*, **2005**, 846, DD12.11.1-DD12.11.6.

(117) Huang, C.; Barlow, S.; Marder, S. R., *J. Org. Chem.*, **2011**, 76, 2386-2407.

(118) Zhan, X.; Facchetti, A.; Barlow, S.; Marks, T. J.; Ratner, M. A.; Wasielewski, M. R.; Marder, S. R., *Adv. Mater.*, **2011**, 23, 268-284.

(119) Würthner, F.; Saha-Möller, C. R.; Fimmel, B.; Ogi, S.; Leowanawat, P.; Schmidt, D., *Chem. Rev.*, **2016**, 116, 962-1052.

(120) Langhals, H.; Karolin, J.; B-A. Johansson, L., *J. Chem. Soc., Faraday Trans.*, **1998**, 94, 2919-2922.

(121) Ramírez, M. G.; Morales-Vidal, M.; Navarro-Fuster, V.; Boj, P. G.; Quintana, J. a.; Villalvilla, J. M.; Retolaza, A.; Merino, S.; Díaz-García, M. A., *J. Mater. Chem. C*, **2013**, 1, 1182-1182.

(122) Calzado, E. M.; Villalvilla, J. M.; Boj, P. G.; Quintana, J. A.; Gómez, R.; Segura, J. L.;

Díaz-García, M. A., *J. Phys. Chem. C*, **2007**, 111, 13595-13605.

(123) Calzado, E. M.; Villalvilla, J. M.; Boj, P. G.; Quintana, J. A.; Gómez, R.; Segura, J. L.; Díaz García, M. A., *Appl. Opt.*, **2007**, 46, 3836-3842.

(124) Herbst, S.; Soberats, B.; Leowanawat, P.; Lehmann, M.; Würthner, F., *Angew. Chem. Int. Ed.*, **2017**, 56, 2162-2165.

(125) Yu, Z.; Wu, Y.; Liao, Q.; Zhang, H.; Bai, S.; Li, H.; Xu, Z.; Sun, C.; Wang, X.; Yao, J.; Fu, H., *J. Am. Chem. Soc.*, **2015**, 137, 15105-15111.

(126) Tropf, L.; Dietrich, C. P.; Herbst, S.; Kanibolotsky, A. L.; Skabara, P. J.; Würthner, F.; Samuel, I. D. W.; Gather, M. C.; Höfling, S., *Appl. Phys. Lett.*, **2017**, 110, 153302.

(127) Unger, K.; Resel, R.; Czibula, C.; C. Ganser; Teichert, C.; Jakopic, G.; Canazza, G.; S. Gazzo; Comoretto, D. In *Distributed Bragg reflectors: Morphology of cellulose acetate and polystyrene multila*, 6th International Conference on Transparent Optical Networks (ICTON 2014), Graz, Austria, Graz, Austria, 2014; pp 1-4.

(128) Lova, P.; Manfredi, G.; Boarino, L.; Comite, A.; Laus, M.; Patrini, M.; Marabelli, F.; Soci, C.; Comoretto, D., *ACS Photonics*, **2015**, 2, 537-543.

(129) Burns, S. E.; Denton, G.; Tessler, N.; Stevens, M. A.; Cacialli, F.; Friend, R. H., *Opt. Mater.*, **1998**, 9, 18-24.

(130) Angeloni, I.; Raja, W.; Brescia, R.; Polovitsyn, A.; De Donato, F.; Canepa, M.; Bertoni, G.; Proietti Zaccaria, R.; Moreels, I., *ACS Photonics*, **2016**, 3, 58-67.

(131) Nasilowski, M.; Mahler, B.; Lhuillier, E.; Ithurria, S.; Dubertret, B., *Chemical Reviews*, **2016**, 116, 10934-10982.

(132) Carbone, L.; Nobile, C.; De Giorgi, M.; Sala, F. D.; Morello, G.; Pompa, P.; Hytch, M.; Snoeck, E.; Fiore, A.; Franchini, I. R.; Nadasan, M.; Silvestre, A. F.; Chiodo, L.; Kudera, S.; Cingolani, R.; Krahne, R.; Manna, L., *Nano Lett.*, **2007**, 7, 2942-2950.

(133) Chen, Y.; Vela, J.; Htoon, H.; Casson, J. L.; Werder, D. J.; Bussian, D. A.; Klimov, V. I.; Hollingsworth, J. A., *J. Am. Chem. Soc.*, **2008**, 130, 5026-5027.

(134) Christodoulou, S.; Vaccaro, G.; Pinchetti, V.; De Donato, F.; Grim, J. Q.; Casu, A.; Genovese, A.; Vicidomini, G.; Diaspro, A.; Brovelli, S.; Manna, L.; Moreels, I., *J. Mater. Chem. C*, **2014**, 2, 3439-3447.

(135) Dai, X.; Zhang, Z.; Jin, Y.; Niu, Y.; Cao, H.; Liang, X.; Chen, L.; Wang, J.; Peng, X., *Nature*, **2014**, 515, 96-99.

(136) Nam, S.; Oh, N.; Zhai, Y.; Shim, M., *ACS Nano*, **2015**, 9, 878-885.

(137) Yang, Y.; Zheng, Y.; Cao, W.; Titov, A.; Hyvonen, J.; Manders, J. R.; Xue, J.; Holloway, P. H.; Qian, L., *Nat Photon*, **2015**, 9, 259-266.

(138) Lin, C. H.; Lafalce, E.; Jung, J.; Smith, M. J.; Malak, S. T.; Aryal, S.; Yoon, Y. J.; Zhai, Y.; Lin, Z.; Vardeny, Z. V.; Tsukruk, V. V., *ACS Photonics*, **2016**, 3, 647-658.

(139) Jiang, Y.; Oh, N.; Shim, M., *ACS Photonics*, **2016**, 3, 1862-1868.

(140) Grim, J. Q.; Christodoulou, S.; Di Stasio, F.; Krahne, R.; Cingolani, R.; Manna, L.; Moreels, I., *Nature Nanotech.*, **2014**, 9, 891-895.

(141) Min, B.; Kima, S.; Okamoto, K.; Yang, L.; Scherer, A.; Atwater, H.; Vahalab, K., *Appl. Phys. Lett.*, **2006**, 89, 191124.

(142) Dang, C.; Lee, J.; Breen, C.; Steckel, J. S.; Coe-Sullivan, S.; Nurmikko, A., *Nat. Nanotechnol.*, **2012**, 335-339.

(143) Schaefer, J.; Mondia, J. P.; Sharma, R.; Lu, Z. H.; Susha, A. S.; Rogach, A. L.; Wang, L. J., *Nano Lett.*, **2012**, 8, 1709-1712.

(144) Kelestemur, Y.; Cihan, A. F.; Guzelturk, B.; Demir, H. V., *Nanoscale*, **2014**, 6, 8509-8514.

(145) Gollner, C.; Ziegler, J.; Protesescu, L.; Dirin, D. N.; Lechner, R. T.; Fritz-Popovski, G.; Sytnyk, M.; Yakunin, S.; Rotter, S.; Yousefi Amin, A. A.; Vidal, C.; Hrelescu, C.; Klar, T. A.; Kovalenko, M. V.; Heiss, W., *ACS Nano*, **2015**, 9, 9792-9801.

(146) Di Stasio, F.; Polovitsyn, A.; Angeloni, I.; Moreels, I.; Krahne, R., *ACS Photonics*, **2016**, 3, 2083-2088.

(147) Pu, C.; Peng, X., *J. Am. Chem. Soc.*, **2016**, 138, 8134-8142.

(148) Jones, M.; Lo, S. S.; Scholes, G. D., *Proceedings of the National Academy of Sciences*, **2009**, 106, 3011-3016.

(149) Jones, M.; Kumar, S.; Lo, S. S.; Scholes, G. D., *J. Phys. Chem. C*, **2008**, 112, 5423-5431.

(150) Lin, W.; Niu, Y.; Meng, R.; Huang, L.; Cao, H.; Zhang, Z.; Qin, H.; Peng, X., *Nano Research*, **2016**, 9, 260-271.

(151) Zhou, R.; Stalder, R.; Xie, D.; Cao, W.; Zheng, Y.; Yang, Y.; Plaisant, M.; Holloway, P. H.; Schanze, K. S.; Reynolds, J. R.; Xue, J., *ACS Nano*, **2013**, 7, 4846-4854.

(152) Zavelani-Rossi, M.; Krahne, R.; Della Valle, G.; Longhi, S.; Franchini, I. R.; Girardo, S.; Scotognella, F.; Pisignano, D.; Manna, L.; Lanzani, G.; Tassone, F., *Laser & Photonics Reviews*, **2012**, 6, 678-683.

(153) Zavelani-Rossi, M.; Lupo, M. G.; Krahne, R.; Manna, L.; Lanzani, G., *Nanoscale*, **2010**,

2, 931-935**.**

(154) Moreels, I.; Rainò, G.; Gomes, R.; Hens, Z.; Stöferle, T.; Mahrt, R. F., *Adv. Mater*.**, 2012**, 24, OP231–OP235**.**

(155) Fischer, A.; Rollny, L.; Pan, J.; Carey, G. H.; Thon, S. M.; Hoogland, S.; Voznyy, O.; Zhitomirsky, D.; Kim, J. Y.; Bakr, O. M.; Sargent, E. H., *Adv. Mater*.**, 2013**, 25, 5742-5749**.**

(156) Di Stasio, F.; Grim, J. Q.; Lesnyak, V.; Rastogi, P.; Manna, L.; Moreels, I.; Krahne, R., *Small***, 2015**, 11, 1328-1334**.**

(157) Canazza, G.; Scotognella, F.; Lanzani, G.; De Silvestri, S.; Zavelani-Rossi, M.; Comoretto, D., *Laser Phys. Lett*.**, 2014**, 11, 035804**.**

(158) Goldenberg, L. M.; Lisinetskii, V.; Schrader, S., *Appl. Phys. B***, 2015**, 120, 271-277**.**

(159) Comoretto, D., *Organic and Hybrid Photonic Crystals*. 1 ed.; Springer International Publishing: Switzerland, 2015; p 497.

(160) Fogg, D. E.; Radzilowski, L. H.; Dabbousi, B. O.; Schrock, R. R.; Thomas, E. L.; Bawendi, M. G., *Macromolecules***, 1997**, 30, 8433-8439**.**

(161) Zanella, M.; Gomes, R.; Povia, M.; Giannini, C.; Zhang, Y.; Riskin, A.; Bael, M. V.; Hens, Z.; Manna, L., *Adv. Mater*.**, 2011**, 23, 2205–2209**.**

(162) Arciniegas, M. P.; Stasio, F. D.; Li, H.; Altamura, D.; De Trizio, L.; Prato, M.; Scarpellini, A.; Moreels, I.; Krahne, R.; Manna, L., *Adv. Funct. Mater*.**, 2016**, 26, 4535-4542**.**

(163) Li, G.; Tan, Z.-K.; Di, D.; Lai, M. L.; Jiang, L.; Lim, J. H.-W.; Friend, R. H.; Greenham, N. C., *Nano Lett*.**, 2015**, 15, 2640-2644**.**

(164) Rippa, M.; Capasso, R.; Mormile, P.; De Nicola, S.; Zanella, M.; Manna, L.; Nenna, G.; Petti, L., *Nanoscale***, 2013**, 5, 331-336**.**

(165) Peng, S.; Zhang, R.; Chen, V. H.; Khabiboulline, E. T.; Braun, P.; Atwater, H. A., *ACS Photonics***, 2016**, 3, 1131-1137**.**

(166) Gazzo, S.; Manfredi, G.; Poetzsch, R.; Wei, Q.; Alloisio, M.; Voit, B.; Comoretto, D., *J. Polym. Sci. B: Polym. Phys*.**, 2016**, 54, 73-80**.**

(167) Frezza, L.; Patrini, M.; Liscidini, M.; Comoretto, D., *J. Phys. Chem. C***, 2011**, 115, 19939-19946**.**

(168) Menon, V. M.; Luberto, M.; Valappil, N. V.; Chatterjee, S., *Opt. Express***, 2008**, 16, 19535-19540**.**

(169) Hou, L.; Hou, Q.; Mo, Y.; Peng, J.; Cao, Y., *Appl. Phys. Lett.*, **2005**, 87, 243504.

(170) Valappil, N. V.; Luberto, M.; Menon, V. M.; Zeylikovich, I.; Gayen, T. K.; Franco, J.; Das, B. B.; Alfano, R. R., *Photonic Nanostruct.*, **2007**, 5, 184-188.

(171) Tan, Z.; Yang, C.; Zhu, Y.; Xu, Z.; Zou, K.; Zhang, F.; Wang, Z., *IEEE Photon. Technol. Lett.*, **2017**, 29, 751-754.

(172) Sheffi, N.; Sadot, D., *J. Lightwave Technol.*, **2017**, 35, 2098-2108.

(173) Pavan, S. K.; Lavrencik, J.; Ralph, S. E., *J. Lightwave Technol.*, **2017**, 35, 1614-1623.

(174) Haruhisa, S.; Ken-ichi, I.; Chiyuki, K.; Yasuharu, S., *Jpn. J. Appl. Phys.*, **1979**, 18, 2329.

(175) Koyama, F., *J. Lightwave Technol.*, **2006**, 24, 4502-4513.

(176) Scofield, A. C.; Kim, S.-H.; Shapiro, J. N.; Lin, A.; Liang, B.; Scherer, A.; Huffaker, D. L., *Nano Lett.*, **2011**, 11, 5387-5390.

(177) Hu, B.; Jin, G.; Liu, T.; Wang, J., *Photonic Sensors*, **2016**, 6, 351-358.

(178) Chang-Hasnain, C. J., *IEEE J. Sel. Topics Quantum Electron.*, **2000**, 6, 978-987.

(179) Vahala, K. J., *Nature*, **2003**, 424, 839-846.

(180) Mizunami, T.; Yamada, T.; Tsuchiya, S., *Opt. Rev.*, **2016**, 23, 703-707.

(181) Iga, K., *IEEE J. Sel. Topics Quantum Electron.*, **2000**, 6, 1201-1215.

(182) Jatta, S.; Zogal, K.; Kögel, B.; Haberle, K.; Sydlo, C.; Meissner, P., *Frequenz*, **2008**, 62, 96-99.

(183) Breiland, W. G.; Allerman, A. A.; Klem, J. F.; Waldrip, K. E., *MRS Bull.*, **2011**, 27, 520-524.

(184) Andrews, J. H.; Crescimanno, M.; Dawson, N. J.; Mao, G.; Petrus, J. B.; Singer, K. D.; Baer, E.; Song, H., *Opt. Express*, **2012**, 20, 15580-15588.

(185) Lova, P.; Grande, V.; Manfredi, G.; Patrini, M.; Herbst, S.; Würthner, F.; Comoretto, D., *Adv. Opt. Mater.*, 5, 1700523.

(186) Gazzo, S.; Manfredi, G.; Pötzsch, R.; Wei, Q.; Alloisio, M.; Voit, B.; Comoretto, D., *J. Polym. Sci., Part B: Polym. Phys.*, **2016**, 54, 73-80.

(187) Knarr III, R. J.; Manfredi, G.; Martinelli, E.; Pannocchia, M.; Repetto, D.; Mennucci, C.; Solano, I.; Canepa, M.; Buatier de Mongeot, F.; Galli, G.; Comoretto, D., *Polymer*, **2016**, 84, 383-390

Appendix A: Theoretical Background

This section reports the basic optics of polymer DBRs, the properties of the photonic band gap and its high order replica. It also discusses the role of the dielectric contrast among the DBR components and reports the basic concept of Transfer Matrix Method modelling.

This section is substantially published at:

Lova, P. et al., Advances in Functional Solution Processed Planar One-Dimensional Photonic Crystals, *Adv. Opt. Mater*.**, 2018**, 6, 1800730-26**.**

A.1 Basic Optics of DBRs

This Paragraph introduces some basic concepts useful to understand the optical response of DBR structures.

As mentioned in Chapter 1, DBRs are lattices of thin films made of media with different refractive index and are considered the simplest PhC structure. As depicted in Figure A.1 a, for a DBR made of alternated layers of two transparent media with thicknesses d_H and d_L and real refractive indexes n_H and n_L ($n_H > n_L$), light is partially refracted, reflected and transmitted at each interface. The lattice spacing, and the layer refractive indexes define whether the interference among reflected (transmitted) beams is constructive (disruptive) at a specific wavelength and in turn, this defines the spectral region of the PBG. When non-absorbing media are used as building blocks, the sum of reflectance and transmittance intensities, neglecting scattering phenomena, is unitary (energy conservation). Then, the photonic structure of a DBR can be easily characterized by mean of simple optical transmittance or reflectance measurements. Figure A.1 b shows a typical reflectance spectrum of a DBR, where the PBG is detected as a pronounced peak, while the background is dominated by a Fabry-Pérot interference pattern arising from the interference of beams reflected at the external DBR interfaces, i.e. by the overall thickness of the DBR, which can be considered as an effective medium.[1]

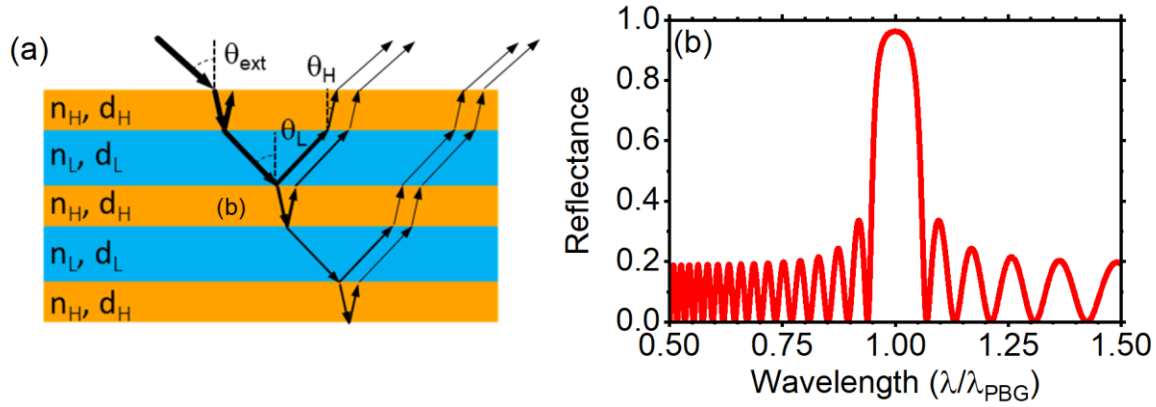

Figure A.1: (a) Reflection, refraction, and transmission in a DBR with $n_H > n_L$. (b) Reflectance spectrum of a polymer DBR made of 15 periods of transparent layers having $n_H = 1.69$ and $n_L = 1.46$.

A.2 Photonic Band Gap Properties in DBRs

Intuitively, the spectral position (λ_{PBG}) and intensity of the reflectance peak assigned to the PBG depend on the thickness of the DBR layers, on their refractive index and on the internal angles of incidence of light (θ_H, θ_L), which are connected to the external incidence angle (θ_{ext}) by the Snell's law ($n_{ext}\, sin\, \theta_{ext} = n_H\, sin\, \theta_H = n_L\, sin\, \theta_L$). Given the planarity of DBRs, it is easy to model their optical response and extract some simple analytical relations, which correlates the PBG position to the structural parameters and to the incidence angle:[2]

S-polarization $$\lambda_{PBG} = 4(d_H+d_L)\frac{n_H n_L \cos\theta_H \cos\theta_L}{n_H \cos\theta_H + n_L \cos\theta_L} \qquad (A.1)$$

P-polarization $$\lambda_{PBG} = 4\frac{n_H n_L (d_H \cos^2\theta_H + d_L \cos^2\theta_L)}{n_H \cos\theta_L + n_L \cos\theta_H} \qquad (A.2)$$

When θ_{ext} increases, the difference between the optical paths of photons reflected at any interface decreases, and the PBG shifts toward short wavelengths. This effect is depicted in Figure A.2 a. The Figure shows the reflectance of a polymer DBR as a function of θ_{ext} calculated by transfer matrix method formalism (see Paragraph A.5) and plotted as a contour plot.[3] In the plot, the horizontal axis reports the wavelength scale, while the vertical one displays θ_{ext}. The color scale indicates the reflectance intensity. The top panel of the Figure displays the data for S-polarized light, while the bottom one shows those for P-polarized light. As expected, for both polarizations, the PBG shifts toward the short wavelengths increasing θ_{ext}. Moreover, for S-polarization the intensity and the width of the PBG optical signature remain almost unchanged, while for P-polarization, both the PBG reflectance intensity and its spectral width decrease as θ_{ext} approaches the Brewster-angle (θ_B) of the structure.[4] The dispersion of the PBG is described in details by the photonic band structure of the DBR, as reported in Figure A.2 b.[4]

Figure A.2 displays that light propagation is never completely inhibited for all directions and for all polarizations. In this case the PBG is said to be incomplete,[5] and sometime it is called stop-band. The incomplete PBG affects light confinement effects, especially for the photoluminescence from emitters embedded in the structure.[6] Indeed, photons propagation

through leaky modes reduces confinement volume, which is crucial to achieve radiative rate enhancement and Purcell effect.[7-9] For this reason, new strategies to achieve omnidirectional PBGs including control of the dielectric contrast, development of ternary structures and structures with graded and anisotropic refractive index, are currently highly investigated.[10-13]

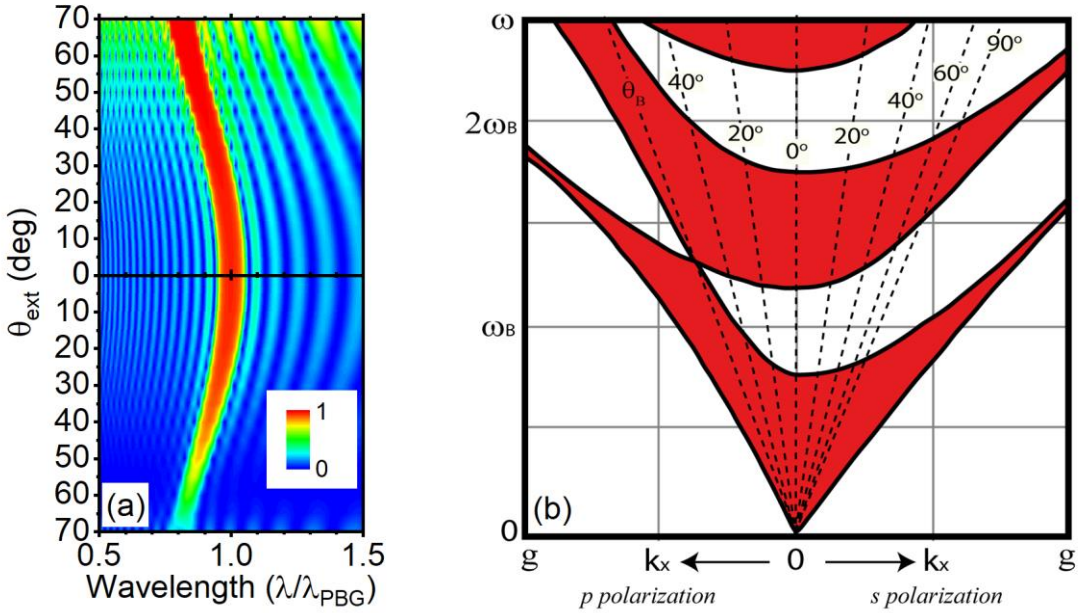

Figure A.2: (a) Calculated angular dispersion reflectance spectra contour plot for a 15-period CA:PVK DBR for S-polarized (top panel) and P-polarized (bottom panel) light; (b) PBG dispersion of a DBR for S- and P-polarizations; (Photonic bands are shaded in red) for n_L=1.5, n_H=3.5, d_L=d_H. The dashed lines corresponds to different values of θ_{ext}; the Brewster' angle is also reported.[14]

When the high and the low refractive index media allows the same optical path ($n_L d_L = n_L d_H$), the lattice is said to fulfil the $\lambda/4$ condition and the DBR can also be called a quarter-wave stack.[5] This condition maximizes the reflectance in correspondence of the first order PBG (see Paragraph A.4) and can be treated analytically.[4-5, 15] The peak reflectivity then follows:

$$R_{PBG} = 1 - 4\left(\frac{n_L}{n_H}\right)^N = 1 - 4\left(1 - \frac{\Delta n}{n_H}\right)^N \qquad (A.3)$$

where N is the number of periods composing the DBR and $\Delta n = n_H - n_L$ is the dielectric contrast among the two dielectric materials. Δn also defines the spectral width of the PBG in $\lambda/4$ condition:[5]

$$\Delta E_{PBG} = \frac{4E_{PBG}}{\pi}\frac{n_H - n_L}{n_H + n_L} = \frac{4E_{PBG}}{\pi}\frac{\Delta n}{2n_L + \Delta n} \qquad (A.4)$$

where, E_{PBG} is the energy of the PBG peak. Then, reflectivity quickly increases as the number of periods increases. Similarly, large dielectric contrast allows large PBG spectral widths and strong reflectivity.

A.3 The Role of the Dielectric Contrast

Aware of the relations between the PBG properties and the dielectric contrast for quarter wave stacks, it is interesting to compare the response of DBRs made by commodity solution processable polymers with those of standard bulky inorganic DBRs available on the market. Figure A.3 a shows the calculated transmittance spectra for a series of DBRs made of 10 periods in $\lambda/4$ condition with PBG centered at 2 eV (~620 nm). The black dotted spectrum represents a bulky DBR made of TiO_2 and SiO_2 (n_h=2.6; n_l=1.46 at 620 nm, respectively). Such oxides are commercially used for reflectors and optical filters and represent the reference benchmark.[16] For the comparison, we considered a series of polymer DBRs, where the low refractive index material is a fluorinated polymer (n_L~1.3),[17] which is one of the lowest indexes available on the market.[17-19] The high index media are instead cellulose acetate (CA, n~1.46),[20] poly(methyl methacrylate) (PMMA, n~1.50),[21] polyacrylic acid (PAA, n~1.51),[22] polyvinyl alcohol (PVA, n~1.52),[22] polystyrene (PS, n~1.58),[20] and poly(N-vinylcarbazole) (PVK, n ~1.68).[23] Currently, PVK provides one of the highest refractive index available among commercial polymers thanks to the pre-resonant enhancement from the carbazole group absorption at about 350 nm.[24-25] We also calculated the spectra for media with larger indexes (1.8, 1.9, and 2) to consider new polymer-inorganic nanocomposites, hyper-branched polysulphides and inverse vulcanized systems, which are promising to increase dielectric contrast in polymer DBRs.[26-33] In Figure A.3 a, each spectrum shows the typical low transmittance band assigned to the PBG, which becomes deeper and wider upon the increase

of the dielectric contrast. The intensity of the interference fringes also increases with this parameter. Figure A.3 b highlights the relation between the minimum of transmittance intensity and the number of periods for the different Δn. As expected from Equation A.3 and Figure A.3 a, the relation among the number of periods and the minimum of transmittance is linear on semi-logarithmic scale. Indeed, the material pair that shows the deeper PBG (higher reflectance) is SiO_2:TiO_2 (black squares), confirming the efficacy of inorganic dielectrics for filter coatings. However, novel high index polymers with comparable number of layers provide similar PBG transmittance values.

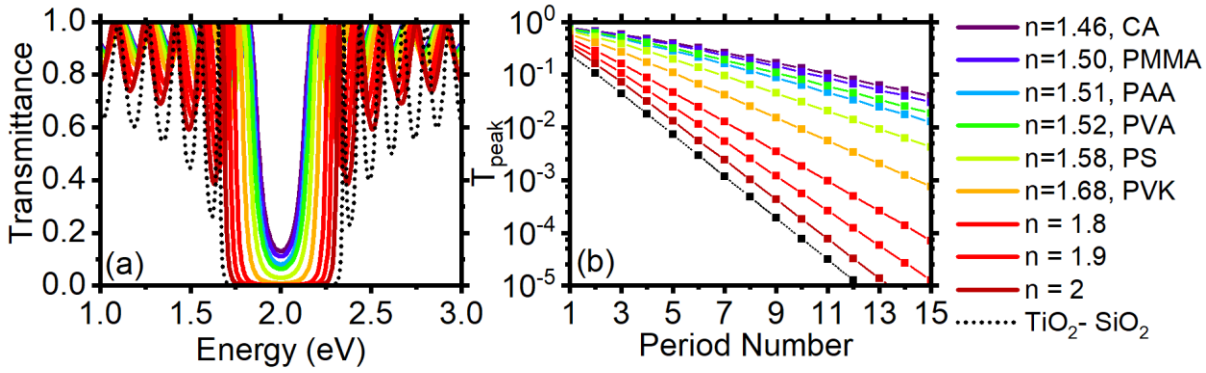

Figure A.3: (a) Calculated transmittance spectra of DBRs made of 10 periods with varying n_H and set n_L=1.3. The high refractive index increases through the values of commonly used polymers (CA, PMMA, PVA, PAA, PS, PVK, and 1.8, 1.9, and 2). The black dotted spectrum is the transmittance for a TiO_2:SiO_2 DBR. (b) Minimum transmittance intensity for the same materials calculated as a function of the number of periods at the PBG peak position (2 eV).

A.4 High Diffraction Orders

The photonic band structure of Figure A.2 b shows that the DBR lattice generates several PBGs. Such stop-bands remind the higher diffraction order structures (m) predicted by the Bragg's law for crystals, which has been proposed to roughly describe the dispersion for 3D opal PhCs,[34] and roughly adapted to the case of DBRs:

$$m\lambda_{PBG} = 2D\sqrt{n_{eff}^2 - sin^2(\theta_{ext})} \qquad (A.5)$$

Where $D = d_H + d_L$, and n_{eff} is the effective refractive index of the DBR. When considering broad spectral ranges, we need to consider the refractive index dispersion to properly describe high diffraction orders. The effect of the dispersion is shown in Figure A.4 a for a DBR made of CA and PVK (black line) and for the same media neglecting the spectral dependence of n (red line). For non-dispersive dielectrics, the higher order PBGs are found exactly at $2E_{PBG}$, $3E_{PBG}$, $4E_{PBG}$ and so on. On the other hand, according to Sellmeir dispersion,[35] the refractive index increases at larger energies shifting the higher order PBGs to higher values (Figure A.4 a, black line). Even though CA and PVK are not highly dispersive, especially if compared with inorganic semiconductors and oxides, the effect of the refractive index dispersion must be considered in the structure design, especially when large spectral ranges are investigated.

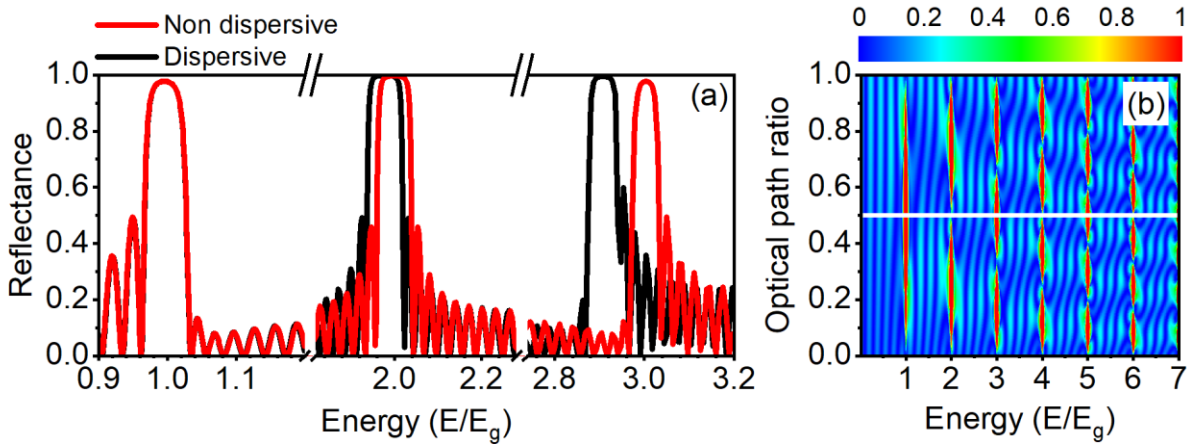

Figure A.4: (a) Reflectance spectra for a 30 periods PVK:CA DBR with dispersive (black) and for the same non-dispersive (red) dielectric functions. (b) Contour plot of calculated DBR reflectance spectra as a function of optical thickness ratio between the DBR components.

Another characteristic of the higher order PBGs is their relative intensity, which is strongly affected by the optical thickness of the dielectrics. Figure A.4 b reports as contour plot the calculated reflectance spectra of DBRs having the same total optical path, but layers with different optical thicknesses ratio. The *x*-axis reports the energy normalized to the first order PBG (E_G). The *y*-axis instead reports the ratio between the optical thickness of the high index layer ($n_H\, d_H$) and the DBR period ($n_H\, d_H + n_L\, d_L$). This scale goes from 0 (low index medium only) to 1 (high index medium only). The λ/4 condition is set at y=0.5 and is highlighted with a white line. In this case, the odd orders have maximum intensity (full constructive interference

among diffracted beams), while for even orders full destructive interference occurs making their intensity negligible. The λ/4 condition is exploited to achieve strong light confinement for lasing and strong-coupling applications.[1, 14] Conditions far from the quarter wave stack, which generate both odd and even diffraction orders are instead interesting to improve sensitivity and lower detection limit in DBR sensors.[36]

A.5 Modelling the Optical Response of the DBR structure

Transfer matrix method (TMM) is largely employed to calculate the propagation of photons, or even electrons,[37] and is the most common approach to simulate the optical response of multilayered structures.[35, 38-46] This method can also be used to calculate energy dispersion relations.[15] In the model, a DBR is considered as a series of layers separated by plane and parallel interfaces, while the electric field of the incident radiation is decomposed in a series of waves propagating from one layer to the other through the interfaces, as shown in Figure A.5 a. There, the z-axis represents the normal incidence direction to the interfaces separating two adjacent layers, while n_m and d_m are the refractive index and thickness of the m-th layer.

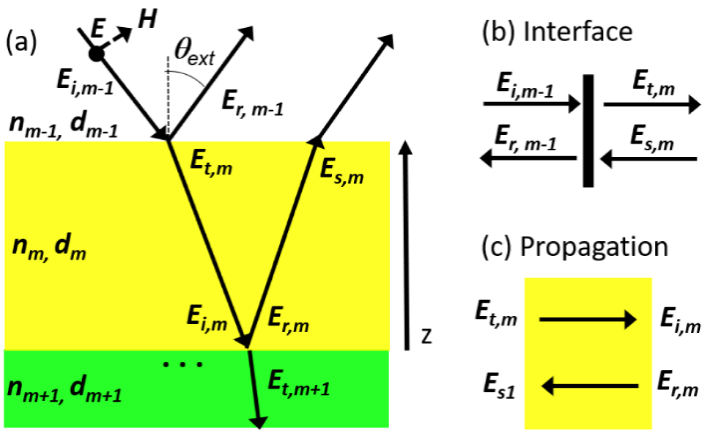

Figure A.5: (a) Schematic of a wave propagating in a DBR period along the z direction with angle of incidence θ_{ext}; (b) Electric field components at an interface and (c) within a dielectric layer.

Within the m-th subunit, we can focus on two blocks. The first block consists in the interface between the (m-1)-th layer and the m-th layer (Figure A.5 b). There, we identify four phasors that indicate the components of the electric field: $E_{i,m-1}$ corresponding to the wave that

propagates in negative z-direction and hits the interface from the (m-1)-th layer side; $E_{r,m-1}$ propagates in positive z-direction and is transmitted at the interface; $E_{t,m}$ propagates in negative z-direction and is transmitted at the interface; $E_{s,m}$ propagates in positive z-direction and hits the interface for the m-th layer side. The second block instead describes wave propagation in the m-th dielectric layer alone (Figure A.5 c), where $E_{t,m}$ propagates until the next interface between the m-th and (m+1)-th layer is reached. At this second interface, we can identify $E_{i,m}$ and $E_{r,m}$, which have the same role of $E_{i,m-1}$ and $E_{r,m-1}$. All the above electric field components are related by simple matrix equations:[47]

$$\begin{pmatrix} E_{t,m} \\ E_{s,m} \end{pmatrix} = D \begin{pmatrix} E_{i,m-1} \\ E_{r,m-1} \end{pmatrix}, \qquad \begin{pmatrix} E_{i,m} \\ E_{r,m} \end{pmatrix} = P \begin{pmatrix} E_{t,m} \\ E_{s,m} \end{pmatrix} \tag{A.6}$$

where D and P are respectively the interface and the propagation matrices, which consider the Fresnel reflection (r) and transmission (t) coefficients at the interface between layers $m-1$ and m.

$$D_{m-1,m} = \frac{1}{t_{m-1,m}} \begin{bmatrix} 1 & r_{m-1,m} \\ r_{m-1,m} & 1 \end{bmatrix} \tag{A.7}$$

and

$$P_m = \begin{bmatrix} e^{-i2\pi\sigma\tilde{n}_m d_m \cos\theta_m} & 0 \\ 0 & e^{i2\pi\sigma\tilde{n}_m d_m \cos\theta_m} \end{bmatrix} \tag{A.8}$$

We can now retrieve the reflectance and the transmittance of a DBR placed in air as:

$$R = \left|\frac{M_{21}}{M_{11}}\right|^2, T = \left|\frac{1}{M_{11}}\right|^2 \tag{A.9}$$

where M_{11} and M_{21} are the (1,1) and (2,1) elements of the matrices P or D, depending on the block under consideration, $\sigma = c/\lambda$ are the wavenumbers, $\tilde{n}_m = n_m + ik_m$ is the complex refractive index of the m-th layer, and θ_m the incidence angle at the m, m+1 interface.

TMM allows to easily calculate reflectance or transmittance spectra in both coherent or incoherent systems.[48-49] Indeed, with respect to the simple and basic formalism here recalled, starting from the late '90s TMM has been improved to better model real structures and extended to investigate more complex effects than the simple optical response of a DBR. For instance, one of the key issues related to TMM modelling of real systems dwells on coherent light propagation, which usually generates a very dense and intense interference pattern in the simulated spectra. Such pattern owes to the partial reflectance within the thick substrate (e.g. 1 mm thick glass slide or fused silica) and can even hide the optical features related to the DBR. Common approaches to overcome this issue consider light incoherence in real systems, modelling the substrate as an infinitely thick medium, or conversely, assuming it as a nanometric layer to account for the interface with the DBR only. More rigorous methods introduce phase shifts in the refracted beams, scattering layers, or incoherent propagation media to achieve both incoherent[47, 50] and partially coherent[47, 51] interference.[47-49, 51] Another variant of TMM uses the E and H fields as components of the vector being multiplied.[15, 38, 52] Moreover, 4-dimensional vectors can be used to account for in-plane anisotropies or incoherence of the light traveling through the structure.[53-54] The flexibility of the TMM makes it interesting also for the modelling of more complex light-matter interaction effects. For instance, the effect of the modified PDOS on the oscillator strength of emitters embedded into microcavities and distributed feedback structures can be studied including internal sources of spontaneous emission and modelling both photoluminescence[55-56] and amplified spontaneous emission.[57] It has also been shown that TMM can be used to simulate second harmonic generation from multilayered structures[58] and the optical response of switches[39] and sensors.[59] Investigation of phonon propagation in the multilayers even allows to determine thermal conductivity in multilayered structures.[60]

References

(1) Comoretto, D., *Organic and Hybrid Photonic Crystals*. Springer: Cham, 2015.

(2) Laussy, F. P., *Microcavities*. Oxford University Press: New York, 2017.

(3) Makino, T., *Prog. Electromagn. Res.*, **1995**, 10, 271-319.

(4) Liscidini, M.; Andreani, L. C., Photonic crystals: An introductory survey. In *Organic and hybrid photonic crystals*, Comoretto, D., Ed. Springer International Publishing: Cham, 2015; pp 3-29.

(5) Joannopoulos, J. D.; Johnson, S. G.; Winn, J. N.; Meade, R. D., *Photonic crystals: molding the flow of light*. Princeton university press: Woodstock, 2011.

(6) Björk, G.; Machida, S.; Yamamoto, Y.; Igeta, K., *Phys. Rev. A*, **1991**, 44, 669-681.

(7) Noda, S.; Fujita, M.; Asano, T., *Nat. Photon.*, **2007**, 1, 449.

(8) Baba, T.; Sano, D., *IEEE J. Sel. Top. Quantum Electron.*, **2003**, 9, 1340-1346.

(9) Oulton, R. F.; Takada, N.; Koe, J.; Stavrinou, P. N.; Bradley, D. D. C., *Semicond. Sci. Technol.*, **2003**, 18, S419.

(10) Fink, Y.; Winn, J. N.; Fan, S.; Chen, C.; Michel, J.; Joannopoulos, J. D.; Thomas, E. L., *Science*, **1998**, 282, 1679-1682.

(11) Winn, J. N.; Fink, Y.; Fan, S.; Joannopoulos, J. D., *Opt. Lett.*, **1998**, 23, 1573-1575.

(12) Shiveshwari, L., *Optik*, **2013**, 124, 5646-5648.

(13) Sharma, S.; Kumar, R.; Singh, K. S.; Kumar, A.; Kumar, V., *Optik*, **2015**, 126, 1146-1149.

(14) Saleh, B. E. A.; Teich, M. C., *Fundamentals of photonics*. John Wiley & Sons Inc: : Hoboken, 2007.

(15) Skorobogatiy, M.; Yang, J., *Fundamentals of photonic crystal guiding*. Cambridge University Press: Cambridge, 2009.

(16) THORLABS, https://www.thorlabs.com/navigation.cfm?guide_id=2210. (accessed 11/12/2019).

(17) Radice, S. V.; Srinivasan, P.; Comoretto, D.; Gazzo, S. One-dimensional planar photonic crystals including fluoropolymer compositions and corresponding fabrication methods. WO 2016/087439 A1, Filing date 9 June 2016, 2016.

(18) Liu, C.-C.; Li, J.-G.; Kuo, S.-W., *RSC Advances*, **2014.**

(19) Giusto, P.; Lova, P.; Manfredi, G.; Gazzo, S.; Srinivasan, B.; Radice, S. V.; Comoretto, D., *ACS Omega*, **2018**, 3, 7517-7522.

(20) Frezza, L.; Patrini, M.; Liscidini, M.; Comoretto, D., *J. Phys. Chem. C*, **2011**, 115, 19939 - 19946.

(21) Beadie, G.; Brindza, M.; Flynn, R. A.; Rosenberg, A.; Shirk, J. S., *Appl. Opt.*, **2015**, 54, F139-F143.

(22) Manfredi, G.; Mayrhofer, C.; Kothleitner, G.; Schennach, R.; Comoretto, D., *Cellulose*, **2016**, 23, 2853-2862.

(23) Canazza, G.; Scotognella, F.; Lanzani, G.; De Silvestri, S.; Zavelani-Rossi, M.; Comoretto, D., *Laser Phys. Lett.*, **2014**, 11, 035804

(24) Comoretto, D.; Moggio, I.; Cuniberti, C.; Dellepiane, G.; Giardini, M. E.; Borghesi, A., *Phys. Rev. B*, **1997**, 56, 10264-10270.

(25) Comoretto, D.; Cuniberti, C.; Musso, G. F.; Dellepiane, G.; Speroni, F.; Botta, C.; Luzzati, S., *Phys. Rev. B*, **1994**, 49, 8059-8066.

(26) Anderson, L. E.; Kleine, T. S.; Zhang, Y.; Phan, D. D.; Namnabat, S.; LaVilla, E. A.; Konopka, K. M.; Ruiz Diaz, L.; Manchester, M. S.; Schwiegerling, J.; Glass, R. S.; Mackay, M. E.; Char, K.; Norwood, R. A.; Pyun, J., *ACS Macro Lett.*, **2017**, 6, 500-504.

(27) Qiang, W.; Xingjie, Z.; Xianping, Q.; Gözde, Ö.; Karin, S.; Anton, K.; Brigitte, V., *Macromol. Chem. Phys.*, **2016**, 217, 1977-1984.

(28) Griebel, J. J.; Namnabat, S.; Kim, E. T.; Himmelhube, R.; Moronta, D. H.; Chung, W. J.; Simmonds Adam, G.; Kim Kyung, J.; van der Laan, J.; Nguyen Ngoc, A.; Dereniak Eustace, L.; Mackay Michael, E.; Kookheon, C.; Glass, R. S.; Norwood, R. A.; Pyun, J., *Adv. Mater.*, **2014**, 26, 3014-3018.

(29) Zhang, Q.; Goh, E. S. M.; Beuerman, R.; Judeh, Z.; Chan-Park, M. B.; Chen, T.; Xu, R., *J. Appl. Polym. Sci.*, **2013**, 129, 1793-1798.

(30) Russo, M.; Campoy-Quiles, M.; Lacharmoise, P.; Ferenczi, T. A. M.; Garriga, M.; Caseri, W. R.; Stingelin, N., *J. Polym. Sci., Part B: Polym. Phys.* , **2012**, 50, 65-74.

(31) Mahendia, S.; Tomar, A. K.; Goyal, P. K.; Kumar, S., *J. Appl. Phys.*, **2013**, 113, 073103.

(32) Liu, J.-g.; Nakamura, Y.; Shibasaki, Y.; Ando, S.; Ueda, M., *Macromolecules*, **2007**, 40, 4614-4620.

(33) You, N.-H.; Suzuki, Y.; Yorifuji, D.; Ando, S.; Ueda, M., *Macromolecules*, **2008**, 41, 6361-6366.

(34) Berti, L.; Cucini, M.; Di Stasio, F.; Comoretto, D.; Galli, M.; Marabelli, F.; Manfredi, N.; Marinzi, C.; Abbotto, A., *J. Phys. Chem. C*, **2010**, 114, 2403-2413.

(35) Bellingeri, M.; Chiasera, A.; Kriegel, I.; Scotognella, F., *Opt. Mater.*, **2017**, 72, 403-421.

(36) Lova, P.; Bastianini, C.; Giusto, P.; Patrini, M.; Rizzo, P.; Guerra, G.; Iodice, M.; Soci, C.; Comoretto, D., *ACS Appl. Mater. Interfaces*, **2016**, 8, 31941–31950.

(37) Markoš, P.; Soukoulis, C. M., *Wave propagation: from electrons to photonic crystals and*

left-handed materials. Princeton University Press: Princeton, 2008; p 352.

(38) Born, M.; Wolf, E.; Bhatia, A. B.; Clemmow, P. C.; Gabor, D.; Stokes, A. R.; Taylor, A. M.; Wayman, P. A.; Wilcock, W. L., *Principles of optics: Electromagnetic theory of propagation, interference and diffraction of light*. Cambridge University Press: Oxford, 1999.

(39) Ahmed, A. M.; Shaban, M.; Aly, A. H., *Optik***, 2017**, 145, 121-129**.**

(40) Sahu, S.; Singh, G. In *Modelling of phase shift Bragg grating biosensor for non invasive detection of blood components*, 2016 International Conference on Recent Advances and Innovations in Engineering (ICRAIE), 23-25 Dec. 2016; 2016; pp 1-3.

(41) Stelitano, S.; Savasta, S.; Patané, S., *Thin Solid Films***, 2014**, 564, 401-405**.**

(42) Bailey, J.; Sharp, J. S., *Eur. Phys. J. E***, 2010**, 33, 41-49**.**

(43) Lova, P.; Cortecchia, D.; S. Krishnamoorthy, H. N.; Giusto, P.; Bastianini, C.; Bruno, A.; Comoretto, D.; Soci, C., *ACS Photonics***, 2018**, 5, 867-874**.**

(44) Manfredi, G.; Lova, P.; Di Stasio, F.; Krahne, R.; Comoretto, D., *ACS Photonics***, 2017**, 4, 1761–1769**.**

(45) Lova, P.; Grande, V.; Manfredi, G.; Patrin, M.; Herbst, S.; Würthner, F.; Comoretto, D., *Adv. Opt. Mater.***, 2017**, 5, 1700523**.**

(46) Scotognella, F.; Varo, S.; Criante, L.; Gazzo, S.; Manfredi, G.; Knarr III, R. J.; Comoretto, D., Spin-Coated Polymer and Hybrid Multilayers and Microcavities. In *Organic and Hybrid Photonic Crystals*, 1st ed.; Comoretto, D., Ed. Springer: Cham, 2015; Vol. 1, p 493.

(47) Troparevsky, M. C.; Sabau, A. S.; Lupini, A. R.; Zhang, Z., *Opt. Express***, 2010**, 18, 24715-24721**.**

(48) Katsidis, C. C.; Siapkas, D. I., *Appl. Opt.***, 2002**, 41, 3978-3987**.**

(49) Prentice, J. S. C., *J. Phys. D***, 2000**, 33, 3139**.**

(50) Ohta, K.; Ishida, H., *Appl. Opt.***, 1990**, 29, 1952-1959**.**

(51) Mitsas, C. L.; Siapkas, D. I., *Appl. Opt.***, 1995**, 34, 1678-1683**.**

(52) Khalil, A. I.; Steer, M. B., *IEEE Trans. Microwave Theory Tech.***, 1999**, 47, 2151-2157**.**

(53) Yeh, P., *Surf. Sci.***, 1980**, 96, 41-53**.**

(54) Wang, L.; Rokhlin, S. I., *Ultrasonics***, 2001**, 39, 413-424**.**

(55) Boucher, Y. G.; Chiasera, A.; Ferrari, M.; Righini, G. C., *Opt. Mater.***, 2009**, 31, 1306-1309**.**

(56) Neyts, K. A., *J. Opt. Soc. Am. A*, **1998**, 15, 962-971.

(57) Boucher, Y. G., *J. Eur. Opt. Soc. Rapid. Publ.* , **2006**, 1.

(58) Li, H.; Haus, J. W.; Banerjee, P. P., *J. Opt. Soc. Am. B*, **2015**, 32, 1456-1462.

(59) Lova, P.; Manfredi, G.; Boarino, L.; Comite, A.; Laus, M.; Patrini, M.; Marabelli, F.; Soci, C.; Comoretto, D., *ACS Photonics*, **2015**, 2, 537-543.

(60) Basu, D.; Blöchl, P. E., *Phys. Status Solidi A*, **2016**, 213, 635-648.

Appendix B: List of Publications

The work summarized in this Thesis have been reported in several publication on indexed international journals:

Sensing

(1) Lova, P.; Megahd, H.; Comoretto, D. Thin Polymer Films: Simple Optical Determination of Molecular Diffusion Coefficients. ACS Applied Polymer Materials 2020, 2, 563-568

(2) Lova, P.; Manfredi, G.; Bastianini, C.; Mennucci, C.; Buatier de Mongeot, F.; Servida, A.; Comoretto, D., Flory-Huggins Photonic Sensors for the Optical Assessment of Molecular Diffusion Coefficients in Polymers, ACS Appl. Mater. Interfaces, 2019, 11, 16872-16880.

(3) Giusto, P.; Lova, P.; Manfredi, G.; Gazzo, S.; Srinivasan, B.; Radice, S. V.; Comoretto, D., Colorimetric Detection of Perfluorinated Compounds by All-Polymer Photonic Transducers ACS Omega, 2018, 3, 7517-7522.

(4) Lova, P., Selective Polymer Distributed Bragg Reflector Vapor Sensors, Polymers, 2018, 10, 1161.

(5) Lova, P.; Comoretto, D., Label-free Vapor Selectivity by Polymer-Inorganic Composite Photonic Crystals Sensors, AIP Conf. Proc., 2018, 1981, 020097.

Emission Control and Lasing

(6) Lova, P.; Giusto, P.; Stasio, F. D.; Manfredi, G.; Paternò, G. M.; Cortecchia, D.; Soci, C.; Comoretto, D., All-Polymer Methylammonium Lead Iodide Perovskite Microcavity, Nanoscale, 2019, 11, 8978-8983

(7) Lova, P.; Cortecchia, D.; Soci, C.; Comoretto, D., Solution Processed Polymer-ABX_4 Perovskite-Like Microcavities, Appl. Sci., 2019, 9.

(8) Lova, P.; Cortecchia, D.; S. Krishnamoorthy, H. N.; Giusto, P.; Bastianini, C.; Bruno, A.; Comoretto, D.; Soci, C., Engineering the Emission of Broadband 2D Perovskites by Polymer Distributed Bragg Reflectors, ACS Photonics, 2018, 5, 867-874.

(9) Manfredi, G.; Lova, P.; Di Stasio, F.; Rastogi, P.; Krahne, R.; Comoretto, D., Lasing From Dot-In-Rod Nanocrystals in Planar Polymer Microcavities, RSC Advances, 2018, 8, 13026-13033.

(10) Manfredi, G.; Lova, P.; Di Stasio, F.; Krahne, R.; Comoretto, D., Directional Fluorescence Spectral Narrowing in All-Polymer Microcavities Doped with CdSe/CdS Dot-in-rod Nanocrystals, ACS Photonics, 2017, 4, 1761–1769.

(11) Lova, P.; Grande, V.; Manfredi, G.; Patrin, M.; Herbst, S.; Würthner, F.; Comoretto, D., All-Polymer Photonic Microcavities Doped with Perylene Bisimide J-Aggregates, Adv. Opt. Mater., 2017, 5, 1700523.

(12) Manfredi, G.; Lova, P.; Di Stasio, F.; Krahne, R.; Comoretto, D. In Directional Fluorescence Shaping and Lasing in All-Polymer Microcavities Doped with CdSe/CdS Dot-in-Rod nanocrystals, 2017 European Conference on Lasers and Electro-Optics and European Quantum Electronics Conference, Munich, 2017/06/25; Optical Society of America: Munich, 2017; p CK_10_2.

Reviews

(13) Lova, P.; Manfredi, G.; Comoretto, D., Advances in Functional Solution Processed Planar One-Dimensional Photonic Crystals, Adv. Opt. Mater., 2018, 6, 1800730-26.

Other Projects

(14) Giusto, P.; Cruz, D.; Heil, T.; Arazoe, H.; Lova, P.; Aida, T.; Comoretto, D.; Patrini, M.; Antonietti, M. Shine Bright Like a Diamond: New Light on an Old Polymeric Semiconductor. *Adv. Mater. https://doi.org/10.1002/adma.201908140*.

(15) Iasilli, G.; Francischello, R.; Lova, P.; Silvano, S.; Surace, A.; Pesce, G.; Alloisio, M.; Patrini, M.; Shimizu, M.; Comoretto, D.; Pucci, A., Luminescent Solar Concentrators: Boosted Optical Efficiency by Polymer Dielectric Mirrors, Mater. Chem. Front., 2019, 3, 429-436.

(16) Lova, P.; Robbiano, V.; Cacialli, F.; Comoretto, D.; Soci, C., Black GaAs by Metal-Assisted Chemical Etching, ACS Appl Mater Interfaces, 2018, 10, 33434-33440.

(17) Martinelli, A.; Alberti, S.; Caratto, V.; Lova, P.; Locardi, F.; Pampararo, G.; Villa, S.; Ferretti, M., Zeitschrift für Kristallographie - Crystalline Materials, 2018, 233, 867

Appendix C: Conference Contributions

The results reported in this Thesis were presented in 23 national and international conference contributions including 21 oral communications and 2 posters.

FisMat 2019, Italian National Conference on the Physics of Matter 2019, 30 September - 4 October 2019, Catania, Italy

1. P. Lova, P. Giusto, F. Di Stasio, G. Manfredi, G. M. Paternò, D. Cortecchia, C. Soci, D. Comoretto. Reshaping Hybrid Perovskites Emission with Flexible Polymer Microcavities (**Oral**)
2. P. Lova, H. Megahd, D. Comoretto. All-polymer Planar Photonic Crystals as an Innovative Tool for the Analysis of Air (**Oral**)

ICSAAM 2019, The 9th International Conference on Structural Analysis of Advanced Materials, 12-15 September 2019

3. P. Lova, H. Meghad, D. Comoretto. A New Method for the Determination of Molecular Diffusion Coefficient in Polymer Films by Simple UV-Vis Spectroscopy (**Oral**)
4. P. Lova, D. Comoretto. Tailoring Optical and Mechanical Properties of Polymers for Photonic applications with Optical Nanocomposites (**Oral**)

Nordic Italian Polymer Future 2019, 3-4 September 2019, Copenhagen, Denmark.

5. P. Lova, D. Comoretto. A Simple Optical Method for the Assessment of Molecular Diffusion Coefficients and Sensing Using Polymer Thin Films (**Oral**)

EPF 2019, European Polymer Federation Congress 2019, 9-14 June, Crete, Greece

6. P. Lova, A. Servida, D. Comoretto. Determination of Diffusion Coefficients and Sensing in Polymer Films by UV-Vis Spectroscopy (**Oral**)

EOSAM 2018, European Optical Society Annual Meeting 2018, 8-12 October 2018, Delft, Netherland

7. P. Lova, D. Cortecchia, H. N. S. Krishnamoorthy, P. Giusto, C. Bastianini, A. Bruno, D. Comoretto, C. Soci. Reshaping White Light Emission from 2D Perovskites with Flexible Photonic Crystals (**Oral**)

8. P. Lova, D. Comoretto. All-polymer Distributed Bragg Reflectors as Innovative and Powerful Chromatic Sensors (**Oral**)

NANOPHOTONICS 2018, 1.3 October 2018, Rome, Italy

9. P. Lova, A. Servida, D. Comoretto. Polymer Distributed Bragg Reflectors: an Old Structure with Unexpected Sensing Capabilities (**Oral**)

Polymer Crystallization Workshop, 1-3 September 2018, Genova, Italy

10. P. Lova, A. Servida, D. Cavallo, G. Portale, D. Comoretto. Polymer Photonic Crystal Sensors (**Oral**)

TOP 2018 - Times of Polymers (TOP) & Composites 2018, 17-21 June 2018, Ischia, Italy

11. P. Lova, D. Comoretto. Label-Free Vapor Selectivity by Polymer-Inorganic Composite Photonic Crystals Sensors **(Oral)**

XXIII CONVEGNO NAZIONALE AIM, 9-12 September 2018, Catania, Italy

12. P. Lova, D. Comoretto, Polymer Photonic Crystals Sensors (**Oral**)
13. P. Lova, G. Pesce, M. Olivieri, M. Alloisio, and D. Comoretto. Polymers for Photonics (**Poster**)

EUPOC 2018, European Polymer Conference 2018, 20-24 May 2018, Como, Italy

14. P. Lova, M. Olivieri, D. Cavallo, M. Viviani, G. Portale, A. Servida, D. Comoretto. Simple UV-VIS Study of Polymer-Molecule Supramolecular Interactions: Assessment of Diffusion Coefficients and Crystallinity in Polymer Films (**Oral**)

MACROGIOVANI 2017, 22-23 June 2017, Trento, Italy

15. P. Lova. Polymer Photonic Crystals Sensors (**Oral and Poster**)
16. G.Manfredi, P.Lova, P. Perkhun, A. Surace, D. Comoretto. Polymer and Hybrid Materials for Photonic Crystals (**Oral and Poster**)

WORKSHOP on Italian-Nordic Polymer Future, 14–15 September 2017, Pisa, Italy

17. P. Lova, G. Manfredi, A. Servida, D. Comoretto. Polymer Multilayered Photonic Crystals Vapor Sensors (**Poster**)
18. G. Manfredi, A. Surace, S. Silvano, P. Lova, D. Comoretto. Polymer and Hybrid Photonic Crystal Structures (**Poster**)

EMRS FALL 2017 - Fall Meeting- European Material Research Society Fall Meeting, 18-21 September 2017, Warsaw, Poland

19. P. Lova, V. Grande, G. Manfredi, M. Patrini, S. Herbst, F. Würthner, D. Comoretto. All-Polymer Microcavities Doped with Perylene Bisimide J-Aggregates (**Oral**)
20. P. Lova, G. Manfredi, A. Servida, D. Comoretto. Sensing and Assessment of Molecular Diffusion Parameters by Polymer Photonic Crystals. (**Oral)**

EPF 2017 - European Polymer Federation Congress 2017, 2-7 July 2017, Lyon, France

21. P.Lova, G. Manfredi, S. Silvano, P. Giusto, D. Comoretto. Polymers for Photonic Devices (**Oral**)

Fotonica 2017 – 19º Convegno Italiano delle Tecnologie Fotoniche 3-5 May 2017, Padova, Italy

22. P. Lova, G. Manfredi, S. Silvano, P. Giusto, D. Comoretto. All-polymer Photonic Crystal Sensors (**Oral**)

MATERIALS 2016 – 12-16 December 2016, Catania, Italy

23. P. Lova, P. Giusto, C. Bastianini, G. Manfredi, D. Comoretto. Polymer Bricks for Photonic Devices (**Oral**)